2

AD-A229 892

Defense Nuclear Agency
Alexandria, VA 22310-3398

DNA-TR-87-171-V6

Effects for ICBM Basing
Volume VI—Numerical Simulation and Evaluation of Non-Ideal Airblast

G. T. Phillips, et al.
Science Applications International Corporation
10260 Campus Point Drive
San Diego, CA 92121

DTIC
S ELECTE D
DEC 0 4 1990
B

December 1990

Technical Report

CONTRACT No. DNA 001-85-C-0090

Approved for public release;
distribution is unlimited.

DISTRIBUTION LIST UPDATE

This mailer is provided to enable DNA to maintain current distribution lists for reports. We would appreciate your providing the requested information.

NOTE:
Please return the mailing label from the document so that any additions, changes, corrections or deletions can be made more easily.

☐ Add the individual listed to your distribution list.

☐ Delete the cited organization/individual.

☐ Change of address.

NAME: ______________________________

ORGANIZATION: ______________________________

OLD ADDRESS	**CURRENT ADDRESS**

TELEPHONE NUMBER: (   ) ______________________________

SUBJECT AREA(s) OF INTEREST:

____

DNA OR OTHER GOVERNMENT CONTRACT NUMBER: ______________________________

CERTIFICATION OF NEED-TO-KNOW BY GOVERNMENT SPONSOR (if other than DNA):

SPONSORING ORGANIZATION: ______________________________

CONTRACTING OFFICER OR REPRESENTATIVE: ______________________________

SIGNATURE: ______________________________

CUT HERE AND RETURN

Director
Defense Nuclear Agency
ATTN: TITL
Washington, DC 20305-1000

Director
Defense Nuclear Agency
ATTN: TITL
Washington, DC 20305-1000

REPORT DOCUMENTATION PAGE

Form Approved
OMB No. 0704-0188

1. AGENCY USE ONLY *(Leave blank)*

2. REPORT DATE
901201

3. REPORT TYPE AND DATES COVERED
Technical 860401 - 870731

4. TITLE AND SUBTITLE
Effects for ICBM Basing
Volume VI—Numerical Simulation and Evaluation
of Non-Ideal Airblast

5. FUNDING NUMBERS
C - DNA 001-85-C-0090
PE - 62715H
PR - RA
TA - RG
WU - DH008826

6. AUTHOR(S)
G. T. Phillips, R. M. Harris, F. Y. Su, C. C. Hsiao,
and R. M. Traci

7. PERFORMING ORGANIZATION NAME(S) AND ADDRESS(ES)
Science Applications International Corporation
10260 Campus Point Drive
San Diego, CA 92121

8. PERFORMING ORGANIZATION REPORT NUMBER
SAIC-87-6550

9. SPONSORING/MONITORING AGENCY NAME(S) AND ADDRESS(ES)
Defense Nuclear Agency
6801 Telegraph Road
Alexandria, VA 22310-3398

SPWE/Rohr

10. SPONSORING/MONITORING AGENCY REPORT NUMBER
DNA-TR-87-171-V6

11. SUPPLEMENTARY NOTES
This work was sponsored by the Defense Nuclear Agency under RDT&E RMC Codes B4662D RA RG 00054 SPAS 3420A 25904D and B4693C RA RG 00010 SPAS 3410A 25904D.

12a. DISTRIBUTION/AVAILABILITY STATEMENT

Approved for public release; distribution is unlimited.

12b. DISTRIBUTION CODE

13. ABSTRACT *(Maximum 200 words)*

The objective of this study was to assess and demonstrate the SAIC "multi-grid methodology" employing the MAGIC model for the study of non-ideal, dusty airblast loads analysis. Two areas of interest to the airblast effects problem were addressed, namely the non-ideal dusty environment flow resulting from both non-precursed and precursed shockwaves, as well as the flow field about generic hard mobile launcher (HML) configurations and resulting loads in that environment.

This study utilized the MAGIC turbulent two-phase flow numerical model to evaluate both the physical processes and numerical effects on the non-ideal dusty walljet development and the associated loads on two dimensional generic HML shapes. The principal features in the development and application of MAGIC to the present problem include a stochastic particle model to treat soil particles in air, an advanced two equation dynamic turbulence model, a high order accurate Flux Corrected Transport (FCT) numerical scheme, and a surface aligned conformal grid network.

14. SUBJECT TERMS

Airblast	Loads
Precursing	Thermal Layer

15. NUMBER OF PAGES
128

16. PRICE CODE

17. SECURITY CLASSIFICATION OF REPORT	18. SECURITY CLASSIFICATION OF THIS PAGE	19. SECURITY CLASSIFICATION OF ABSTRACT	20. LIMITATION OF ABSTRACT
UNCLASSIFIED	UNCLASSIFIED	UNCLASSIFIED	SAR

CLASSIFIED BY

N/A since Unclassified

DECLASSIFY ON
N/A since Unclassified

13. ABSTRACT (Continued)

The study demonstrated the viability of a sequential multi-grid methodology in which separate solution domains are defined for the environment and vehicle flow field computations where data from the environment simulation is used to drive the vehicle calculation. This sequential multi-grid approach, along with the use of the surface conformal orthogonal grid system, attempts to reconcile the different resolution needs of the non-ideal dusty walljet flow with the more refined resolution needs of the flow about the HML shape. The resolution needs are dictated by the desire to resolve the turbulent two-phase physics, which dominate the flow in each respective region and which are included in the MAGIC model.

SUMMARY

The objective of the current program was the continued refinement and validation of a multi-phase viscous airblast flow methodology appropriate to the prediction of near surface airblast environments and loads for both ideal and non-ideal precursed or non-precursed waveforms. Specifically, the current program had as its intent the study of the role of dust in the evolution of precursed or non-precursed non-ideal blast waveforms and the further refinement of the sequential multi-grid methodology.

In general, the methodology has as its basis the concept that airblast effects can be predicted through the use of a sequential multi-grid approach employing a compressible, multi-phase, viscous or inviscid numerical fluids model. That is, the methodology seeks to calculate multi-phase, compressible, viscous or inviscid flow on successively smaller and more highly refined domains ultimately to arrive at the detailed flow structure about a vehicle. Each simulation may be performed with either of two SAIC developed models: MAGIC or BISON. The MAGIC model is a multi-phase viscous model applicable to solutions on an arbitrary mesh. The BISON model is a multi-phase inviscid model restricted to Cartesian geometry. The calculations summarized in this report were generated using the MAGIC model. Previous studies have utilized both models for the prediction of airblast environments.

At full scale, the sequential multi-grid methodology would employ both the BISON and MAGIC simulation capabilities to determine the airblast environments and loads. The inviscid model, BISON, would be employed to generate the earlier time prediction on a coarse grid appropriate to the full domain solution. The MAGIC model would then apply these results to develop a more highly resolved near surface environment domain which would include viscous effects. Finally, MAGIC would be employed again to develop the predicted loads on a vehicle using a body-fitted grid system for highly resolved calculations in the vehicle domain.

The simulations reviewed in this report did not consider full scale predictions; thus the first step in the sequential multi-grid process, the use

of BISON to obtain a full domain simulation was, not required. Emphasis here was on the engineering scale where detailed experimental data were available for model validation. For these applications, MAGIC was applied to obtain an environments simulation on the scale of the shocktube used in the experimental program. The data generated from this "large" scale prediction was then used to drive the smaller vehicle domain high resolution calculation.

For the data reported here, the engineering test scale refers to the CERF HST6 environment scaled at ~ 1/100 and the model loads tests scaled at ~ 1/15 relative to the megaton criterion environment for the HML vehicle. Further, scaling of dust size was not considered. Although the scaling was inconsistent and not entirely suitable to the task of determining accurate design requirements, it was sufficient for computational model validation. Justification of this belief is that if the model is capable of accurate predictions at scales approximately correct, it should be sufficiently self consistent to give accurate answers at full scale. In fact, with respect to dust, model predictions should be more accurate, since dust particle equilibrium with the gas phase is much more likely at full scale.

Previous studies performed by SAIC as part of the DNA blastwave effects technology program have demonstrated the importance of the following: turbulence in the development of the non-ideal blastwave profile, high order accurate numerics, surface conformal, orthogonal grid systems and the sequential multi-grid approach. These properties were previously made an integral part of the SAIC blastwave methodology. The engineering scale dusty flow simulations studies described in this report further demonstrate the role of dust in the development of the non-ideal blastwave profile for both precursed and non-precursed waveforms. The results of this current investigation have led to some definite conclusions relative to dusty blastwave boundary layer modeling mechanisms and have provided for the continued refinement of the multi-phase aspects of the current blastwave simulation models.

The qualitatively and quantitatively good agreement between the simulations results and experimental data for both the environment and loads continues to substantiate the "mixing controlled" dust entrainment (scouring) hypothesis proposed by SAIC. By "mixing controlled" it is meant that the effective particle entrainment rate and injection velocity both scale according to the level of turbulent fluctuations in the wall layer. That is, they are proportional to the mixing or shear velocity. The particles are thus entrained by the same mechanism that distributes them throughout the boundary layer. Further, these particles do not play a passive role. The simulations show that the particles have a moderate effect on the mean velocity profile, surface shear and boundary layer thickness and most likely a secondary effect on the gas turbulence properties. For the environments this means a reduced gas momentum flux within the boundary layer. This in turn affects the predicted loads because, among other factors, the modified approach flow alters the size and duration of the upstream flow separation region ahead of the vehicle.

The current methodology appears to be sufficient to capture the trends and in many cases the magnitude of the effect of dust on the characteristics of the blastwave flow for both precursed and non-precursed non-ideal flows. There are, of course, issues which have not been addressed and which may be important to the ultimate prediction of environments and loads in a dusty environment. The current multi-phase approach assumes that dust densities remain sufficiently low so that particle-particle interactions may be neglected. This assumption is probably valid in most of the flow domain. However this assumption is not likely to be true, very near the surface. Dust densities in this region have been shown to be sufficiently high to warrant the need to consider particle wake and collision processes. SAIC is currently considering modifications to its discrete dust particle approach to include these effects; however, none of the results described in this paper consider such interactions. A second area of possible importance is the nature of particle rebound off loading surfaces. The discrete particle nature of the current multi-phase modeling approach, unlike continuum approaches in common use, is capable of treating crossing particle trajectories. This freedom allows the study of particle rebound at solid boundaries (current continuum approaches must assume particle stick). The degree of particle rebound from a fixed surface obviously affects the momentum imparted to the surface and hence the resulting loads experienced by the surface. This area of study has not been sufficiently pursued and remains an active topic of research.

With the exceptions noted above, the methodology presented in this report is felt to be applicable and, in fact, preferable for the study of full scale dusty airblast flows. The capability presents a state-of-the-art multi-phase viscous or inviscid modeling approach for accurately describing the loads experienced on an arbitrarily shaped surface structure. The methodology contains provisions for predicting the complete blastwave history from the burst point to ground ranges of interest through the use of a sequential multi-grid approach which may incorporate both inviscid and viscous numerical models.

PREFACE

This report was prepared by the Theoretical Physics Division and the Fluid and Material Sciences Operation of Science Applications International Corporation (SAIC), La Jolla, California for the U.S. Defense Nuclear Agency (DNA). The research described in the report was conducted under DNA Contract No. DNA-001-85-C-0090. Dr. Paul R. Rohr of DNA SPAS provided technical guidance for the project.

The program represented a cooperative effort between SAIC's Theoretical Physics Division in La Jolla, California and the Fluid and Material Sciences Operation in Valley Forge, Pennsylvania with Gary T. Phillips of the Theoretical Physics Division serving as the Principal Investigator for the research. Dr. Thomas B. Harris of the Fluid and Material Sciences Operation was Task Manager for the HML Dusty Loads analysis task. Additional support was provided by Richard M. Traci of Fluid Physics International. Staff scientists F.Y. Su and C.C. Hsiao were principal technical contributors in all areas of Magic model refinement, testing and application to both the environment and loads analysis aspects of the program. Finally, D. C. Moore and C. M. Dougherty provided programming and graphics support.

CONVERSION TABLE

Conversion factors for U.S. Customary to metric (SI) units of measurement.

MULTIPLY → BY → TO GET
TO GET ← BY ← DIVIDE

angstrom	1.000 000 X 10^{-10}	meters (m)
atmosphere (normal)	1.013 25 X 10^{+2}	kilo pascal (kPa)
bar	1.000 000 X 10^{+2}	kilo pascal (kPa)
barn	1.000 000 X 10^{-28}	meter^2 (m^2)
British thermal unit (thermochemical)	1.054 350 X 10^{+3}	joule (J)
calorie (thermochemical)	4.184 000	joule (J)
cal (thermochemical)/cm^2	4.184 000 X 10^{-2}	mega joule/m^2 (MJ/m^2)
curie	3.700 000 X 10^{+1}	*giga becquerel (GBq)
degree (angle)	1.745 329 X 10^{-2}	radian (rad)
degree Fahrenheit	$t_K = (t^{\circ}f + 459.67)/1.8$	degree kelvin (K)
electron volt	11605.4	degree kelvin (K)
erg	1.000 000 X 10^{-7}	joule (J)
erg/second	1.000 000 X 10^{-7}	watt (W)
foot	3.048 000 X 10^{-1}	meter (m)
foot-pound-force	1.355 818	joule (J)
gallon (U.S. liquid)	3.785 412 X 10^{-3}	meter^3 (m^3)
inch	2.540 000 X 10^{-2}	meter (m)
jerk	1.000 000 X 10^{+9}	joule (J)
joule/kilogram (J/kg) (radiation dose absorbed)	1.000 000	Gray (Gy)
kilotons	4.183	terajoules (TJ)
kip (1000 lbf)	4.448 222 X 10^{+3}	newton (N)
kip/inch^2 (ksi)	6.894 757 X 10^{+3}	kilo pascal (kPa)
ktap	1.000 000 X 10^{+2}	newton-second/m^2 (N-s/m^2)
micron	1.000 000 X 10^{-6}	meter (m)
mil	2.540 000 X 10^{-5}	meter (m)
mile (international)	1.609 344 X 10^{+3}	meter (m)
ounce	2.834 952 X 10^{-2}	kilogram (kg)
pound-force (lbs avoirdupois)	4.448 222	newton (N)
pound-force inch	1.129 848 X 10^{-1}	newton-meter (N-m)
pound-force/inch	1.751 268 X 10^{+2}	newton/meter (N/m)
pound-force/foot^2	4.788 026 X 10^{-2}	kilo pascal (kPa)
pound-force/inch^2 (psi)	6.894 757	kilo pascal (kPa)
pound-mass (lbm avoirdupois)	4.535 924 X 10^{-1}	kilogram (kg)
pound-mass-foot^2 (moment of inertia)	4.214 011 X 10^{-2}	kilogram-meter^2 (kg m^2)
pound-mass/foot^3	1.601 846 X 10^{+1}	kilogram/meter^3 (kg/m^3)
rad (radiation dose absorbed)	1.000 000 X 10^{-2}	**Gray (Gy)
roentgen	2.579 760 X 10^{-4}	coulomb/kilogram (C/kg)
shake	1.000 000 X 10^{-8}	second (s)
slug	1.459 390 X 10^{+1}	kilogram (kg)
torr (mm Hg, 0° C)	1.333 22 X 10^{-1}	kilo pascal (kPa)

*The becquerel (Bq) is the SI unit of radioactivity; 1 Bq = 1 event/s.
**The Gray (Gy) is the SI unit of absorbed radiation.

TABLE OF CONTENTS

LIST OF ILLUSTRATIONS

LIST OF ILLUSTRATIONS (continued)

LIST OF ILLUSTRATIONS (continued)

LIST OF ILLUSTRATIONS (concluded)

SECTION 1
INTRODUCTION

Nuclear blastwave vulnerability of surface targets is made uncertain due to our lack of a quantitative understanding of non-ideal effects. Those non-ideal effects which are believed to be of critical importance to surface structure vulnerability are associated with dusty, precursed, and turbulent blastwaves. Their relation to the observed loads on a surface vehicle are the subject of this study. The research described here contributes to the ongoing US Defense Nuclear Agency (DNA) blastwave effects technology program by utilizing the **MAGIC** turbulent, two-phase flow, numerical model to evaluate the loads, under non-ideal conditions, on two-dimensional Hardened Mobile Launcher (HML) shapes.

Non-ideal airblast effects associated with precursed airblast environments arise due to the heating of the ground surface by the nuclear fireball radiation. The hot ground surface heats the surface air layer through conduction, convection and reradiation. Radiative heating can also directly deposit energy into the lofted absorbing soil particles. Additional air heating occurs from the heat exchange between lofted hot soil particles and the air. The resulting hot, dusty air layer displays a higher sound speed than the overlaying air, allowing the airblast front within this near surface air layer to move ahead of the main shock wave. The resulting refracted shock wave connecting the precursed shock with the main shock, along with the entrained thermal layer, produces a highly vortical region of the flow. This vortical region bounded below by the ground surface produces an intense wall jet which may enhance the vulnerability of near surface structures.

The numerical prediction of non-ideal airblast is one of considerable complexity both in the accurate description of the physics of the flows and in the accurate numerical representation of the multi-scales associated with the flow. The physical complexities include the unsteady, compressible, turbulent and multi-phase nature of the airblast near surface environment as well as the complex geometries, thin surface boundary layers and separation regions associated with the vehicle domain. The accurate description of the multi-scale flow regimes places an extreme burden on the numerics, and the numerical solution technique must be capable of yielding numerical non-diffusive predictions at all scales of interest. To accomplish this task, the scheme must be of high order, but without numerical oscillations, and it must be able to accurately resolve all scales of interest from the entire blastwave domain down to the thin shear layers along the vehicle boundary.

The **MAGIC** numerical program (Traci, et. al., 1981), developed at SAIC, embodies the principal physical and numerical features required to obtain an accurate description of the non-ideal airblast environment and vehicle loads. These principal features include:

- an advanced two-equation dynamic turbulence model
- a stochastic discrete particle two-phase flow model
- a Flux Corrected Transport (FCT) high order advection scheme
- a surface conformal orthogonal grid system

The methodology for developing accurate airblast environments and loads predictions makes use of the **MAGIC** program with the attributes above along with a "sequential multi-grid" simulation technique. This methodology is illustrated schematically in Figure 1. The top figure displays the non-ideal airblast environment with an indication of the appropriate scales pertinent to HML vulnerability. The critical spatial scales are noted to range from ones of meters for the vehicle flow domain to tens of meters appropriate to the non-ideal airblast features to finally hundreds of meters for the global blast wave flow. This figure suggests the use of a global blastwave solution to "drive" the near surface flow domain and the use of that solution to, in turn, drive the vehicle flow domain. Hence, the need for a sequential multi-grid methodology. To further reconcile the need for varying degrees of spatial resolution, the most finely resolved vehicle flow domain also employs a surface conformal orthogonal grid system to assure accuracy within the region of the vehicle. Two examples of mesh gridding within this region are indicated at the bottom of Figure 1.

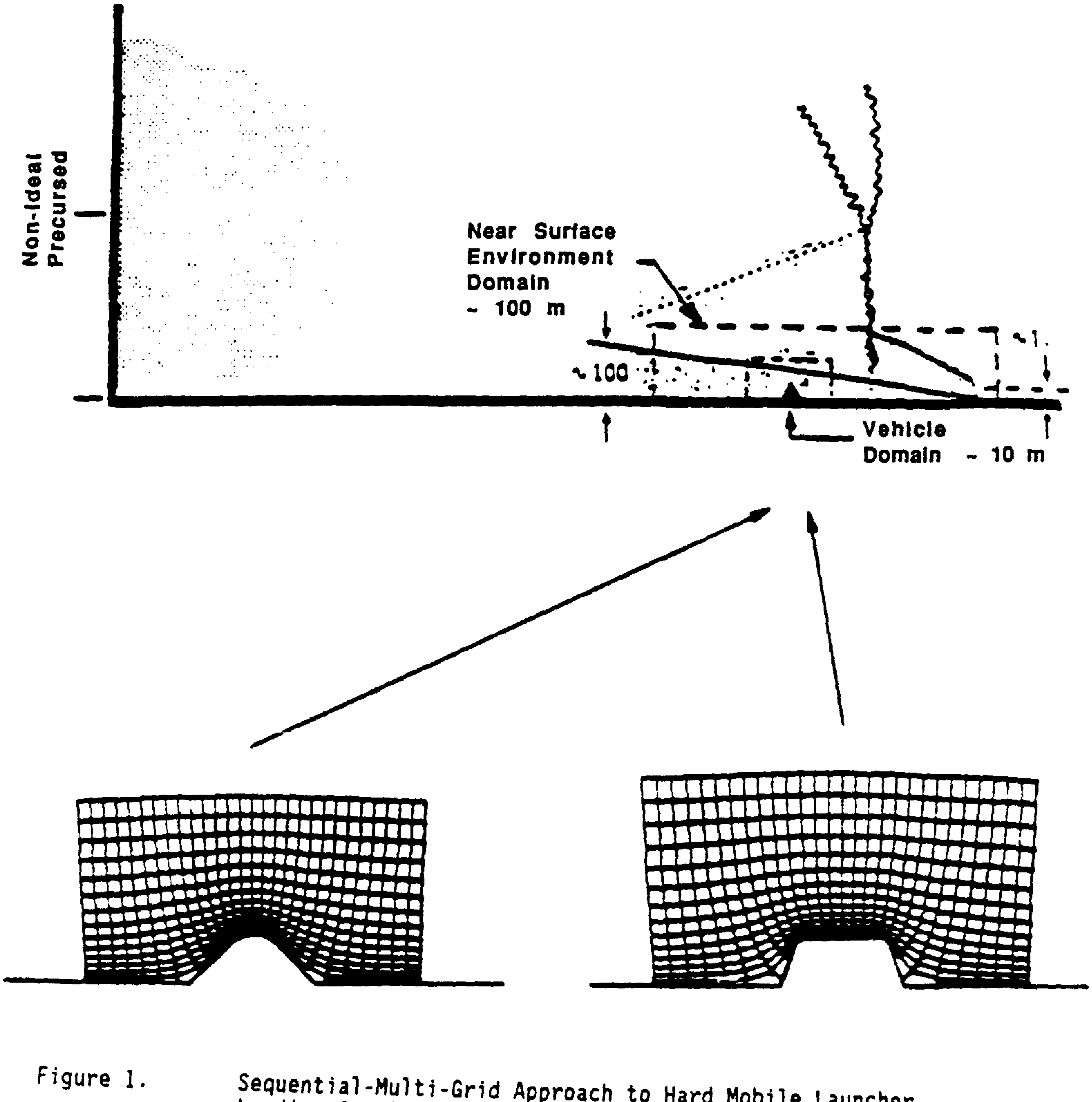

Figure 1. Sequential-Multi-Grid Approach to Hard Mobile Launcher Loading Simulations.

This methodology was demonstrated in a previous SAIC study for DNA relevant to loads on HML vehicles (Traci, et. al., 1987). The cases considered there were for primarily clean flows (no dust). That study addressed both areas of interest to the airblast effects problem; namely, the non-ideal environment flow as well as the vehicle flowfield and loads associated with that environment. The methodology was employed primarily to the study of engineering scale tests as represented by shocktube simulations performed in the New Mexico Engineering Research Institute's (NMERI) six-foot horizontal shocktube at the Civil Engineering Research Facility (CERF) located in Albuquerque, New Mexico. This data provided the opportunity to validate both the non-ideal environment and the vehicle loads in conjunction with a thorough evaluation of numerical and physical effects embodied in the **MAGIC** program. The main conclusion reached in that study was that the SAIC methodology incorporating the **MAGIC** program is a viable approach to the accurate simulation of the non-ideal airblast environment and semi-bluff body loads at the engineering test scale.

The present program builds upon this earlier work by incorporating dust phenomenology into the prediction of non-ideal airblast environments and loads and by considering further refinements to the numerics employed in the **MAGIC** program. The approach is identical to that taken in the previous study, namely, that the sequential multi-grid methodology is employed first to determine the dusty non-ideal airblast environment which then is used to drive the loads domain solution. The model predictions selected are based on the availability of corroborative experimental data since, because of the complexity of the flow, experimental data provides the only reliable test of the model's predictive capabilities.

Further model refinements include the generalization of the FCT technique employed in **MAGIC** to allow non-rectangular zoning and the provision for the communication of dust densities and distribution between the environment and loads domains. Although the previous study proved the utility of the SAIC methodology for predicting accurate vehicle loads, continued model refinements are essential to provide ever increasing accuracy in model predictions.

In its original form, the FCT algorithm, was appropriate to Cartesian gridding only. The need to employ conformal gridding for accuracy in the vehicle domain dictated that this original algorithm be modified to yield a technique appropriate to general four-sided polygons. The adaption of FCT to the conformal domain accomplished under the current study provides for an additional refinement to the solution to achieve optimum accuracy of the loads predictions within the context of an FCT monotonicity preserving scheme. A discussion of the current algorithm along with validation simulations is provided in Section 3.

Dusty flow airblast simulations within the context of a sequential multi-grid methodology required the implementation of a communications algorithm for dust properties between the environments domain and the vehicle domain and this had not yet been accomplished in the previous study. The previous study had shown, however, that accurate predictions of dusty airblast flow for the environments domain was possible using the two-phase flow discrete particle approach. Thus, the groundwork had already been laid for producing complete loads simulation data with dust effects included and required only that the communication of dust properties between the two simulation domains be fully implemented. This task was completed as part of the current effort extending the multi-phase flow capabilities of the **MAGIC** model to include the multi-grid methodology. The implementation of this capability is discussed in Section 4.

The core task under the current program was the simulation of dusty environments and loads on an HML shape at the engineering scale. This task makes use of the numerical refinements discussed above and relied upon experimental data to provide the requiiired validation of the numerically refined **MAGIC** model. Experimental data was provided by NMERI CERF six-foot shocktube data base. These data were used both to initialize the environments domain and to provide a means to compare simulated results with real data. Environments simulations were performed for both dusty non-precursed and precursed blast waves. Loads calculations were undertaken for precursed blastwaves only. Environments simulation results for both blastwave flows is presented in Section 2. The corresponding loads simulations for precursed blastwaves are given in Section 4. Finally, Section 4 contains a "Scaled-up" simulation (factor of 15 in space and time) of loads on an HML shape. This simulation provides a first look at the application of the sequential multi-grid methodology employing the **MAGIC** model to loads predictions at scales substantially larger than the engineering scale validation calculations.

The objectives of this study have been met in that they provide a tool for predicting non-ideal airblast loads including dust effects for two-dimensional semi-bluff bodies. The simulated results indicate that the SAIC methodology developed over a two-year period is capable of yielding both qualitative and quantitatively accurate loads data necessary for vulnerability assessment of above surface structures subject to non-ideal airblast flows at moderate overpressures. This conclusion is based upon detailed comparisons with engineering scale data for transient non-ideal blastwaves including dust. The application of this predictive methodology to full scale loads predictions is believed to be straightforward, and the validation studies undertaken to date should provide a high confidence level for the user. A summary of the complete multi-year program detailing the overall development and validation effort is given in Section 5.

SECTION 2
DUSTY FLOW ENVIRONMENTS

Uncertainties in nuclear blastwave effects in the low to moderate overpressure regime center largely on the precursed shock flow field. Of particular importance for precursed airblast and in general for all airblast environments are the complex fluid/surface interaction phenomena which may be referred to as the "dusty boundary layer" processes. Such processes are dominated by turbulent mixing effects and two-phase (soil particle/air) flow interactions.

The critical blastwave environment is illustrated in Figures 2a and 2b. The schematic suggests the scales of the relevant inviscid and turbulent viscous phenomena for an ideal surface Mach blast region and the non-ideal precursed blastwave, respectively. The scales shown are appropriate to the 30 psi overpressure range assuming a 1 MT yield at a height of burst of 2000 ft. The largely inviscid nature of the ideal blast case is quantitatively understood and well represented by current global blastwave computations as well as blastwave property curve fits. In both cases, turbulent viscous effects modify the flowfield outside the indicated shear layers only slightly. The shear layer of importance here is the surface boundary layer since surface structures may lie entirely within the boundary layer and since the boundary layer modifies the blastwave flow profile near the ground resulting in high levels of turbulence and dust entrainment.

The blastwave boundary layer has been studied for idealized smooth surfaces under the assumption of laminar flow (Mirels, 1956, 1958; Quan and Traci, 1971) and turbulent flow (Quan and Crawford, 1972; Mirels, 1984a and 1984b). The ideal surface assumption (perfectly smooth) applied in these studies, however, underestimates the boundary layer thickness (see Figure 3a). Figure 2a, displays an ideal Mach shock configuration showing the Mach triple point (TP), Mach stem (M), reflected shock (R), incident shock (I), and slip line (SL) along with the estimated boundary layer growth. The current estimate as shown in Figure 2a, is 25 m for more realistic surface roughness in the range

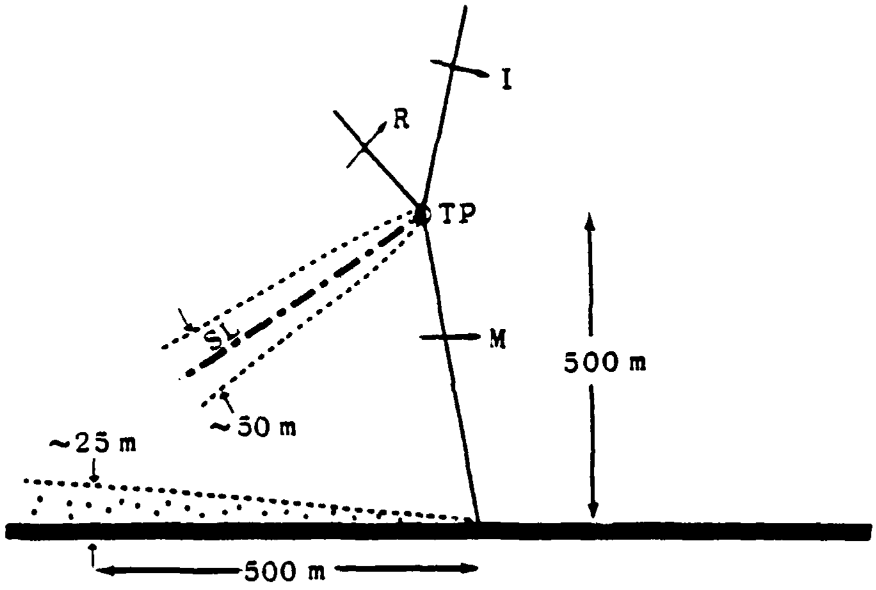

a. Ideal MACH Shock Schematic

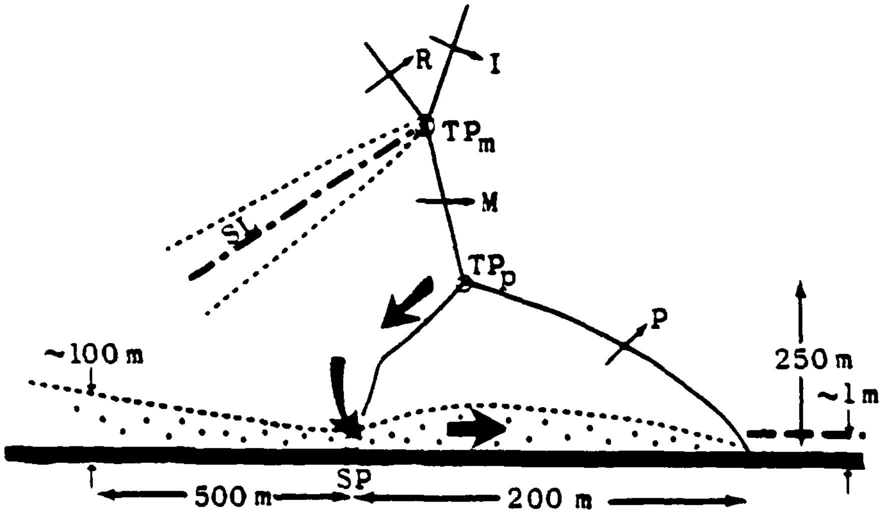

b. Non-Ideal Precursed Shock Schematic

Figure 2. Ideal and Non-Ideal Blastwave Schematic for the Complex MACH Regime - Scales Appropriate to a 30 psi Overpressure Assuming a 1 MT Burst at 610 m (2000 ft).

of 1 to 10 cm. This value is based on estimates made as part of the current study and is believed to represent more accurately the disturbed mean velocity profile, turbulence and dust particle environment. These are, of course, the main parameters which are of interest to surface structure vulnerability.

The blastwave boundary layer associated with a non-ideal precursed shock environment, shown in Figure 2b, is considerably more complicated in both its inviscid and turbulent viscous structure. In addition to the structure shown in Figure 2a, there is the additional structure associated with the precursor: precursor shock (P), precursor triple point (TP_p) and flow stagnation point (SP). The near surface environment is best characterized as a fully merged flow field in that the near surface vortical flow region is intimately coupled to the inviscid precursed shock above. Thus the usual boundary layer approximation applicable to the ideal blastwave solution, in which the boundary layer can be considered separately from and driven by the inviscid outer flow, is not appropriate.

The non-ideal precursed shock flow field is caused by the preshock surface heating resulting from the emitted fireball thermal radiation. The hot surface in turn heats the near surface air layer through a combination of lofted surface material, convection and radiation. This hot, dusty, high sound speed layer causes the shock wave near the ground to move ahead of the main shock wave. The refracted shock front and entrained thermal layer produce a vortical flow region near the ground which may be referred to as the "wall jet" flow structure. The thermal layer is seen to serve as a conduit for converting the post-shock flow reservoir into a high speed jet of air near the surface which can lead to augmented dust entrainment and enhanced loads.

Based on computational predictions of the non-ideal precursed airblast environments, it is found that the equilibrium thickness of the wall jet is roughly six to eight times the prescribed pre-shock thermal layer thickness. The equilibration of the jet thickness is a function of the duration or "run-up" length of the precursor and is important since it results in an expansion of the flow around the wedge-like nose of the precursor. The combination of incident shock strength and thermal layer temperature or sound speed control the jet intensity, as measured by the dynamic pressure. This enhanced dynamic pressure implies higher surface shear which in turn implies an increased rate of dust entrainment. This entrained dust will to a large degree follow the turbulent eddies eventually filling the wall jet region and resulting in a thicker dust cloud than expected for ideal surfaces.

The effect of the precursed non-ideal airblast environment on the near surface turbulent, dusty boundary layer is summarized in Figure 3. The curves in these figures compare the surface boundary layer growth for ideal smooth and rough surfaces and for the precursed non-ideal blastwave environment. Figure 3a, displays the estimated boundary layer growth assuming an ideal surface. Surface roughness effects as a function of the surface roughness parameter (k_s) are noted to be significant and can lead to as much as a ten-fold increase in boundary layer thickness when compared to a ideally smooth surface. Figure 3b, displays the boundary layer growth for the non-ideal case and shows that in addition to the surface boundary layer growing up from below, the mixing layer, which separates the processed pre-shock thermal layer from the ambient, grows down from above. Estimates of the growth of the relevant layers presented in this figure are based on the rough surface boundary layer estimates made as part of this study and the Brown and Roshko (1974, 1976) mixing layer data. Based on these estimates, the two layers are expected to merge approximately 200 m behind the front. This indicates that during the highest intensity of the wall jet flow, just before the Mach shock extension (moving stagnation point) arrives, the flow is likely to be fully turbulent. After this point, not shown in the figure, the moving stagnation point slows the flow and squeezes it to the surface, thus reducing the depth of the boundary layer. Past this point, the boundary layer will begin to grow again with a rate of growth similar to that found for the ideal case, see Figure 2b.

For both the ideal and non-ideal blastwave environments, the dust is entrained from the ground and diffuses away from the surface to fill the respective turbulent shear layers. From a modeling standpoint, the essential features of both environments are the turbulence (its generation, intensity,

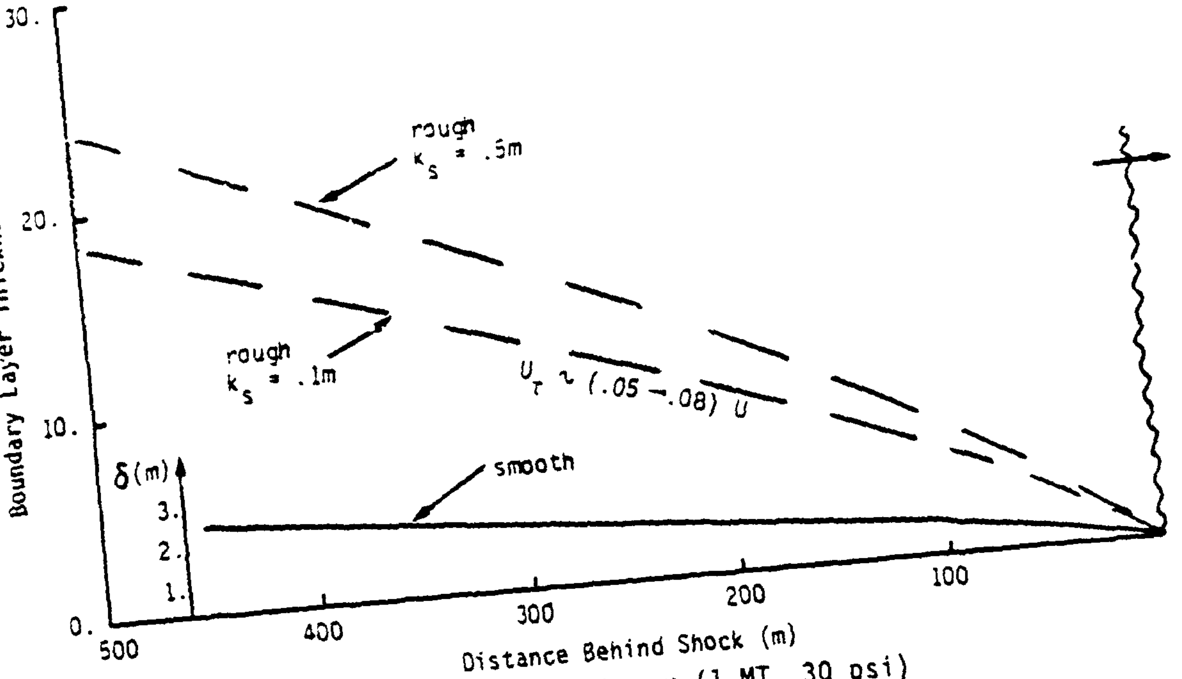

a. Ideal Airblast Boundary Layer (1 MT, 30 psi)

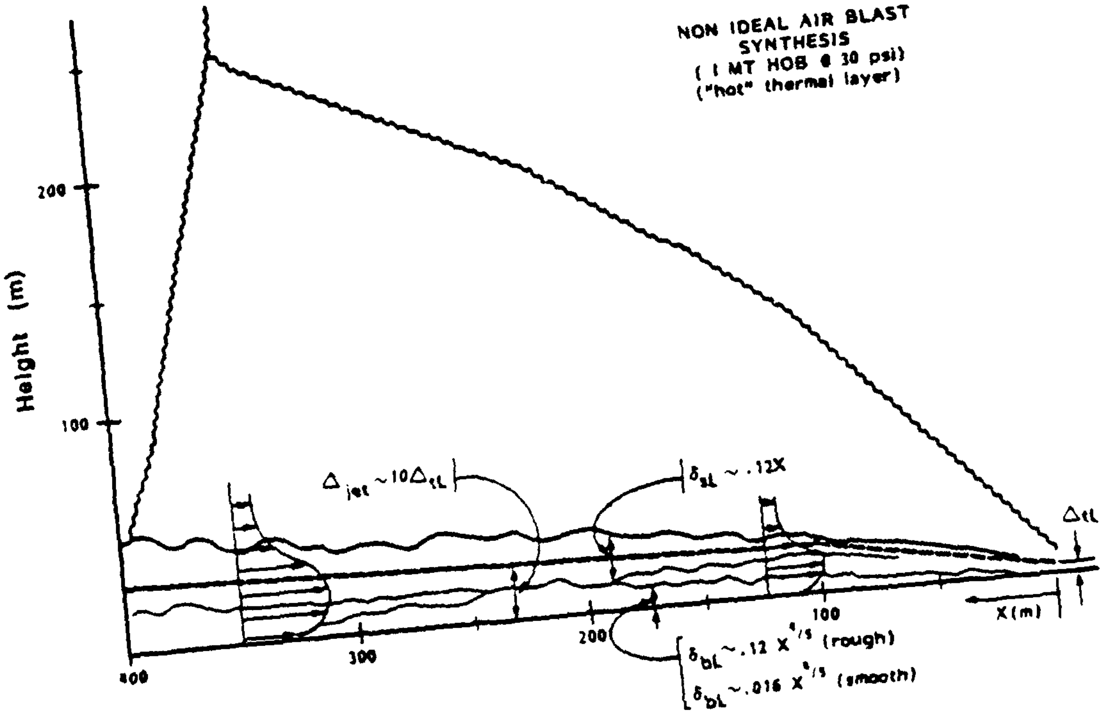

b. Non-Ideal Airblast "Wall Jet" Synthesis

Figure 3. Schematics of Near Surface Blast Wave Environment.

scale and influence on the mean flow) and the dust loading (particle entrainment and evolution in the turbulent flow). These effects, although confined principally to the shear layer regions, can be expected to have a moderating influence on the global, largely inviscid flow. That is, turbulent mixing will affect the growth and deceleration of the wall jet to a degree which may be sufficient to affect the precursor pressure distribution by retarding the expansion around the post-shock thermal layer. Similarly, the dust will have a retardation and growth effect due to its momentum exchange with the air and would be difficult to distinguish from the turbulent mixing effect.

2.1 DUSTY AIRBLAST BOUNDARY LAYER METHODOLOGY.

The study of dusty precursed non-ideal airblast flow via a predictive computational approach was accomplished through comparative simulations of experimental tests at the laboratory and engineering test scales. This procedure allowed for the validation of the approach, leading the way to a predictive capability at full scale. The numerical predictions of dusty flow blast boundary layers were accomplished through the application of the two-dimensional axisymmetric model, MAGIC. These predictions were then compared with experimental data sets from two shocktube experiments. The laboratory scale experimental data were taken from the TRW 4" shocktube and the engineering scale data were obtained from one of the dusty flow tests (HST6-89) carried out in the New Mexico Engineering Research Institute's (NMERI) six foot diameter horizontal shocktube located at the Civil Engineering Research Facility (CERF) in Albuquerque, New Mexico. The TRW simulations have been described in previous reports (Traci, et. al., 1987) and will not be considered here. The CERF tube simulations were completed during this contract period and are the major subject of this report.

The dusty airblast predictive methodology is based upon the MAGIC computational model. MAGIC is a finite difference numerical model for multicomponent reactive turbulent flows with general application to simulations of complex multi-species compressible flows. The model implements a relatively complete set of physical processes within the framework of a numerical simulation technique. These numerical and physical model approaches are described in detail by Traci and Su (1986).

The model effects a two-dimensional time dependent solution of the coupled fluid dynAmic/particulate/chemical system of Reynolds' averaged conservation equations (mass, momentum, species energy transport, turbulence equations and particle trajectories). Subsidiary equations for boundary conditions (inflow, outflow, particle injection, etc.) as well as real or ideal equations of state close the system of equations. The numerical solution technique is based on a "control volume" differencing scheme, after Hirt et al. (1974), with a generalized coordinate system to resolve irregular and moving boundaries and an acoustic implicitization technique to permit efficient calculations of low Mach number flows. The model provides for higher order accuracy through a Flux Corrected Transport (FCT) spatial differencing scheme based on Boris and Book (1971, 1974, 1976) with the flux limiter treatment of Zalesak (1979). Turbulent closure is effected using the two-equation dynamic turbulence transport model of Saffman-Wilcox-Traci (1976). Finally, two-phase flow effects are considered by including Lagrangian particle trajectories for an ensemble of representative particles which interact with and couple to the gas flow through momentum (drag), energy (heat transfer) and mass (vaporization) exchange.

The quantification and understanding of two-phase flow effects requires the capability to describe the entrainment, transport and evolution of particles or condensed phase droplets coupled to the vapor state flow. The capability implemented in MAGIC accounts for both the single particle trajectory and the multiple particle "cloud" nature of two phase flows. An accurate description of these general limiting cases must include the rate limiting exchange processes occurring between the particles and the gas phase flow as well as the evolution and mixing of vaporized particle material. The approach formulated here consists of a set of equations governing the dynamic and thermal evolution of an ensemble of representative single particles. Account is taken of the evolving particle mass, two components of momentum and energy, as well as the resulting interchange with the gas phase flow. The interchange is treated as effective source terms in the conservation equations for the vaporized particle species (if present), the gas phase momentum and the gas phase energy. These terms are evaluated and accumulated over all particles during the subcycle solution for the evolution of the individual particles. Integrated over time, the solution provides for the description of the fully coupled two-phase mixture.

This particle interaction approach allows for full non-equilibrium two-phase flow modeling. The key element of this approach is embodied in the particle trajectory analysis which implements the interphase transport mechanisms of mass, momentum and energy exchange. These effects can be modeled in various levels of detail, and the model implemented in MAGIC seeks to balance the detail of the approach with the goal of providing an engineering simulation model. The principal assumptions made to arrive at this goal are: particle shape is neglected (assumption of equivalent sphere), internal particle structure is neglected (particle characterized by a single temperature and composition), dilute two-phase flow is assumed (particle- particle interactions are ignored) and phase changes occur at the particle surface with instantaneous vapor state mixing.

In the present dusty boundary layer study, the main interest is in demonstrating and validating the approach. Thus, the main emphasis was placed on describing the dust cloud evolution for simple injection schemes, the most basic of which was the assumption of uniform particle size, vertical injection velocity and particle temperature behind the shock. More complex conditions, however, have been prescribed, including non-uniform particle injection based on local shear rates at the surface along with a given particle size distribution function. The latter is felt to be more representative of the expected positional dependence of soil flux in the non-ideal blastwave.

Confidence in the modeling approach has been gained through extensive validation simulations aimed at verifying the model's ability to treat the two major aspects of two-phase flows: coupled mean flow interactions and particle turbulent diffusion. The coupled flow aspects of the model have been verified against exact solutions for single particle trajectories and in an extensive study of fuel injection processes (Su et. al., 1983). These studies incorporated experimental results and provided excellent tests of model performance under conditions in which the flow was dominated by the interphase coupling process. For these tests the turbulence attendant to the injection flow (particle laden jet) served primarily to moderate the action of momentum exchange within the flow by controlling the induced entrainment of surrounding fluid into the jet. Direct turbulent effects on the particles were of secondary importance. For dusty shock boundary layers, turbulence effects on the dust particles is not secondary. Further, it is postulated that the turbulence field is the major contributor to the effective dust entrainment from the surface in addition to controlling the evolution of the particle cloud in the blastwave boundary layer. Thus, verifying that the model is capable of treating mean flow interactions accurately is a necessary, but not sufficient, test of the dusty flow methodology.

Verification of the particle diffusion aspects of the model is complicated by the fact that particles respond to changes in the gas flow conditions according to their rate dependent dynamics (ie., a turbulence Schmidt Number, $Sc_t < 1$). Thus they do not necessarily diffuse in the same manner as passive molecular species ($Sc_t = 1$). Consideration of such effects is on the forefront of two-phase flow technology, and the model implemented in MAGIC is an attempt to include a degree of generality within the context of an engineering model.

Although the model allows for a Schmidt number dependence, the current calculations assumed that $Sc_t = 1$. This becomes the principle limiting assumption in the model. The correctness of this assumption can be semi-quantitatively checked using a perturbation method as applied in other particulate turbulent diffusion studies (Traci, 1981). The method contained in this reference examines the time dependent response of a single component of a particle velocity. This analysis provides a measure of particle fluctuations in response to gas turbulence and, at least to first order, indicates the degree to which the particles follow the turbulent gas flow. Based on this analysis it can be shown that for ideal or non-ideal turbulent blastwave flow, the response time of typical particles having a mean diameter of 100μ is in the range $0.1 < \tau_d < 1$ msec. This particle time constant along with the turbulent time constant (estimated from the turbulent length scale and intensity in a turbulent boundary layer, $\tau_t \approx .05\,\delta/u_\tau$), allows one to estimate the error made in assuming $Sc_t = 1$. For a full scale boundary layer of from 1 to 10 meters a reasonable estimate of the turbulent time scale is on the order of 3 to 30 msec. Substituting these values into the equation for the particle fluctuating velocity found in Traci (1983), it can be shown that the particles would follow the energy containing eddies to within a few percent. This leads to the conclusion that the $Sc_t = 1$ assumption considered here is appropriate for the full scale blastwave boundary layer.

Unfortunately, this assumption becomes less correct as the flow is scaled down to the engineering or laboratory scale. For example and as noted above, a series of dusty flow experiments have been carried out in the TRW 4" shocktube (Ausherman, 1973) in which the blast boundary layer thickness was on the order of 2 cm with a turbulent time scale of 0.1 msec. Applying the same argument as above would indicate that $\langle u'^2_d \rangle^{1/2} \approx .03 \langle u'^2 \rangle^{1/2}$, where u'_d is the particle fluctuating velocity and u' is the gas fluctuating velocity. Thus the particle response time is so sluggish relative to the turbulent eddy time scale that it is unlikely that the particles would respond very energetically to the gas turbulence and hence would diffuse slowly within the boundary layer. In this extreme case the $Sc_t = 1$ assumption is not realistic. However this does not necessarily imply a limitation of the modeling methodology, since a predictive capability for the full scale event is what is required. It does, however, cast some doubt as to the appropriateness of performing experiments at such small scales with the intent of inferring interactions at larger scales.

To complete the dusty shock boundary layer methodology a dust entrainment model must be specified. The entrainment of soil into the blastwave boundary layer flow is recognized as an important but complicated phenomenon controlled by the interfacial forces exchanged between the air and ground. Unfortunately, the state-of-the-art of fluid-solid interaction analysis for a solid which is frangible at relatively low stress levels cannot, at present, treat the processes of air infiltration, breakup and particle entrainment from first principles arguments. Consequently, computational approaches and dust sweep-up assessment analyses require an entrainment model which provides a boundary condition for the more manageable but nonetheless difficult two-phase flow analysis of the blastwave flow. The entrainment process has been relatively well studied from this standpoint for geophysical (Bagnold, 1941; Chepil, 1945; Owen, 1964), downwash impingement (Vidal, 1962; Roberts, 1963), mine safety (Singer, et al., 1969, 1972, 1974, 1976; Dawes, 1852) and nuclear effects (Swatosh, 1970; Quan and Traci, 1970; Kirsch, 1977; Rosenblatt, 1984; Denison and Baum, 1984; Mirels, 1984) research areas. In addition, experiments with direct application to blastwave dust boundary layer environments have been performed (Aushermann, 1973; Hartenbaum, 1971; Kulkarny, et. al. 1985; Dudziak, 1985). Although this breadth of activity would seem to be sufficient to allow a good understanding of the entrainment process, no widely accepted dust entrainment model is currently available. The model presented here is one which seeks to incorporate sufficient physical mechanisms to allow general application within the context of an engineering approach to the entrainment problem.

A dust entrainment model must provide the effective mass flux (m_d) and either the injection velocity (v_d) or mass density (ρ_d) of particles at the effective interface between the soil and dust-air mixture. In addition, a representation of the particle size distribution is required to determine the evolution and coupling of the particles to the boundary layer flow. The three primary injection parameters can be related by the expression:

$$\dot{m}_d = \rho_d V_d \tag{1}$$

From the various references cited above, a number of models have been proposed which are either empirically based on experimental data or physically based on arguments for momentum exchange between the fluid and the soil. Known empirically based models are limited by the paucity of relevant data bases. Of the physically based models, most assume that the entrainment rate is governed by and proportional to the local aerodynamic shear at the soil interface.

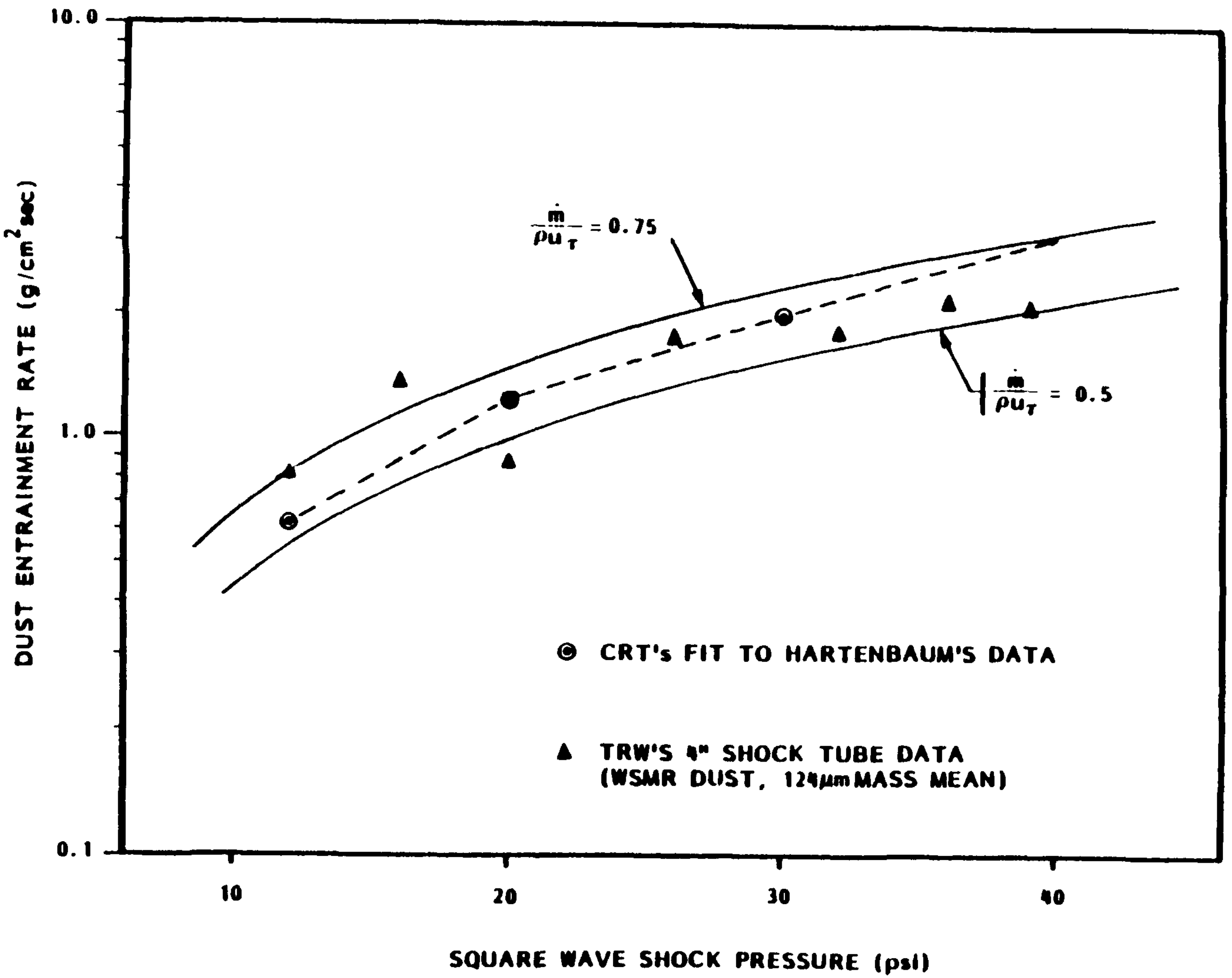

Figure 4. Dust Entrainment Rate for Relevant Shock Overpressures Range Data and Model Comparison.

Additionally, some of these models include a term to represent the cohesiveness of the soil. The entrainment approach employed in this study is similar to these physically based models (Kirsch, 1977; Roberts, 1963) with the exception that the friction velocity, rather than the shear stress, is explicitly used to define the local entrainment rate. This approach is based on the premise that entrainment is controlled by the turbulent mixing velocity or fluctuations, u', where near the surface $u' \approx u_T$, where u_T is the local shear stress. Based on this assumption and using the available dusty boundary layer data bases, it is possible to derive a correlation between the mass entrainment rate and the local friction velocity at the air-soil interface as shown in Figure 4. This figure displays data from two experimental data bases (Hartenbaum, 1971 and Ausherman, 1973) as well as two proposed fits to those data founded on a mixing controlled entrainment rate as a function of shock overpressure. The figure indicates that the trend with respect to overpressure or increased free stream velocity is captured by the concept of mixing controlled entrainment ($\dot{m}/\rho u_T$ curves). Further, this figure indicates that the data is bounded by correlation constants ranging between 0.5 and 0.75.

One additional parameter is required to close the dust entrainment model. Typically the one chosen is the injection velocity. Again a number of approaches could be considered to determine a realistic injection velocity. The current approach is to define the normalized, with respect to the speed of the free-stream, injection velocity via comparisons with experimental data. Data sampling from the Ausherman experiment (millimeter size glass beads), would suggest a value between 0.01 and 0.023. Thus an appropriate first approximation to the normalized injection velocity would be the mean of this range or 0.015. It should be noted, however, that the concept of mixing induced entrainment implies a distribution of injection speeds with a mean value of u_T and a significant variation about this mean. Such a distribution is included as an option in the model and has been applied in simulations performed as part of this study. This effect is important for small scale shocktube simulations, but it is probably not as critical at large scales.

In general, then, the current two-phase flow methodology provides a relatively complete and general description of dusty blast boundary layer flow. As will be described in the following section, demonstration and validation calculations have been performed and have shown that the model is capable of accurately predicting the phenomenology inherent in the boundary layer processes associated with both ideal and non-ideal airblast.

2.2 ENVIRONMENTS SIMULATION RESULTS.

Numerical simulations using the dusty flow model summarized in the preceding section and implemented into the MAGIC turbulent compressible flow model were performed and compared with experimental data. The experimental data sets selected represent engineering scale ideal and non-ideal simulations of a full scale blastwave. Previous laboratory scale simulations have been compared with data taken in the 4" TRW shocktube (Ausherman, 1973) in Traci, et al. (1987). The engineering scale simulations are compared here with data available from the NMERI CERF 6-foot shocktube, (Dudziak, 1985).

As noted above, prior to this current study several laboratory scale simulations were performed as part of the overall multi-year DNA program in order to demonstrate of the capabilities of the two-phase flow modeling methodology. These demonstration simulations comprised a limited parametric study of shock induced dusty boundary layers and considered variations in particle size and injection speeds. The relatively good comparison with the data was encouraging in light of the preliminary nature of these calculations. The Ausherman experiment, however, used dust which consisted primarily of 100-micron particles and, as noted in the previous section, were too large to respond adequately to the turbulent flow. This implied that the good agreement shown between these earlier calculations and experiment was most likely due to the assumptions attendant to the entrainment model implemented, rather than the dust diffusion methodology. Thus, these earlier comparisons may be considered as a validation of the current dust entrainment hypothesis, namely that entrainment is mixing controlled.

Scaling the simulations up to the engineering level experiments was deemed necessary for adequate exploration of the dust diffusion methodology employed in the MAGIC model. To this end, two environments simulations based on experiments carried out in the NMERI CERF 6-foot shocktube were performed. The first, an ideal simulation, was compared with experimental data provided by Dudziak (1985). The second, a non-ideal simulation, was run to delineate the expected differences in the dust cloud characteristics under these conditions. Both simulations assumed identical computational domains and differed only in the treatment of the near surface air layer characteristics. That is, the non-ideal case assumed a near surface helium layer to approximate a hot thermal layer near the ground surface.

The CERF HST6 shocktube has provided a significant source of data to the Defense Nuclear Agency (DNA) Blastwave Technology Program. Numerous "engineering test scale" experiments have been performed in the facility over the past two years, directed primarily at verifying the helium layer simulation approach for non-ideal blastwave waveforms. Within certain limitations, the tests have achieved this objective and in addition have provided selected data sets useful for validating numerical model simulations of the non-ideal wall jet structure and the effect of that flow on the static and pitot pressure fields. These tests provide the basis for the following comparative viscous dusty flow solutions using the MAGIC model. The engineering scale MAGIC simulations of a dusty ideal blast boundary layer relates to the direct simulation of one of these tests, HST6-89 (Dudziak, 1985) for the ideal case and a comparative non-ideal simulation for which no direct test data was available.

A schematic of the HST6 high explosive shocktube with specific description of the helium layer induced precursed shock test section is given in Figure 5. For the test series of interest here, the configuration of the shocktube consisted of a 14 ft driver section with open breech end and some 200 ft of driven section. The shocktube is nominally 6 ft in diameter but includes a floor within the test section, extending from the 60 to 160 ft station, which reduces the shocktube height to 4.5 ft. The driver for these tests varied

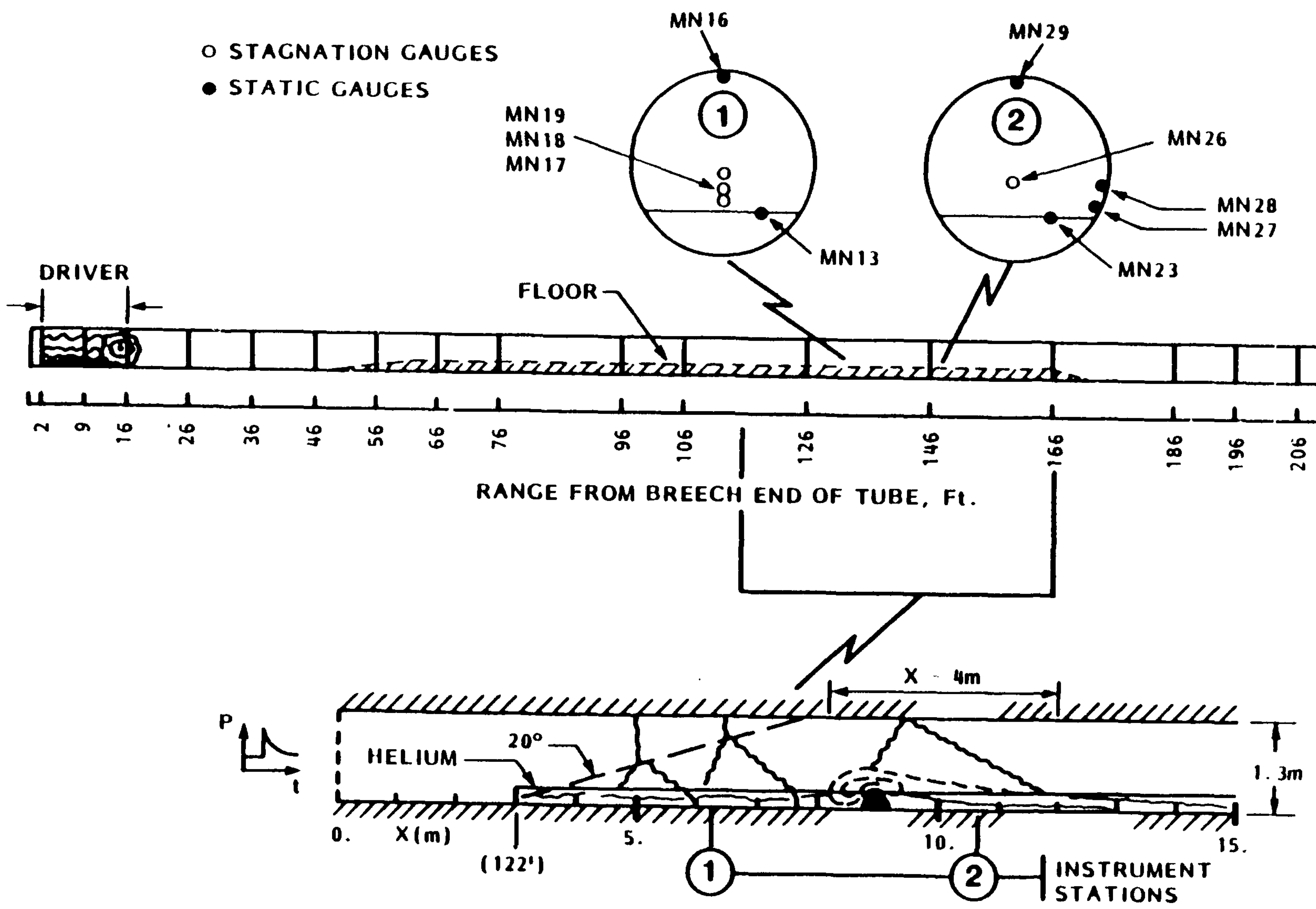

Figure 5. NMERI CERF HST6 Shocktube and Helium Layer - Airblast Simulation Schematic.

somewhat during the development test series. Test HST6-89 had a similar driver to that used in HST6-39, which in previous SAIC studies was used to represent a baseline driver configuration. This driver is also identical to that used in HST6-60, a precursed non-ideal test with a test model included. Test HST6-60 is used for the loads simulation comparisons found in Section 4. The driver consisted of 19 strands of 400 gr/ft PETN det cord distributed throughout the driver test section for a total of 15 lbs. of high explosive. In the test section, this configuration resulted in a relatively clean peaked wave decaying from 50 to 30 psi overpressure and half-peak time constant of from 10 to 15 msec. This driver waveform is approximately a 1:20 scale when compared to a one megaton waveform.

Test HST6-89 was a non-precursed (ideal) test. Tests HST6-39 and HST6-60 were precursed (non-ideal) experiments where the non-ideal airblast waveform was simulated in the test facility by inducing a precursed shock front using a high soundspeed helium layer contained in a mylar "bag" on the floor of the shocktube. A 5 inch thick layer is typically used to replicate the expected full scale thermal layer thickness of approximately 10 ft. As indicated in Figure 5, the helium layer started at the 122 ft station for test HST6-39 and HST6-60. Also shown in this figure are the two instrument stations which provided the only test diagnostics (static and total pressure measurements as indicated) for use in the comparative exercise described below.

The MAGIC model viscous simulation of HST6-89 was performed in two-dimensional rectangular coordinates using the grid design and problem set-up conditions described in Figure 6. The simulation region spans the floor-to-ceiling extent of the shock tube for a 15 m rectangular section around the helium layer test section. The development of the grid design was based on previous experience with shock boundary layer simulations and is believed to provide an accurate representation of the flow. It consists of 200 axial zones of constant 7.5 cm cell-size and 50 vertical zones expanded in a geometric progression from a minimum size of 5 mm near the floor to a maximum zone size of 8 cm near the shocktube ceiling.

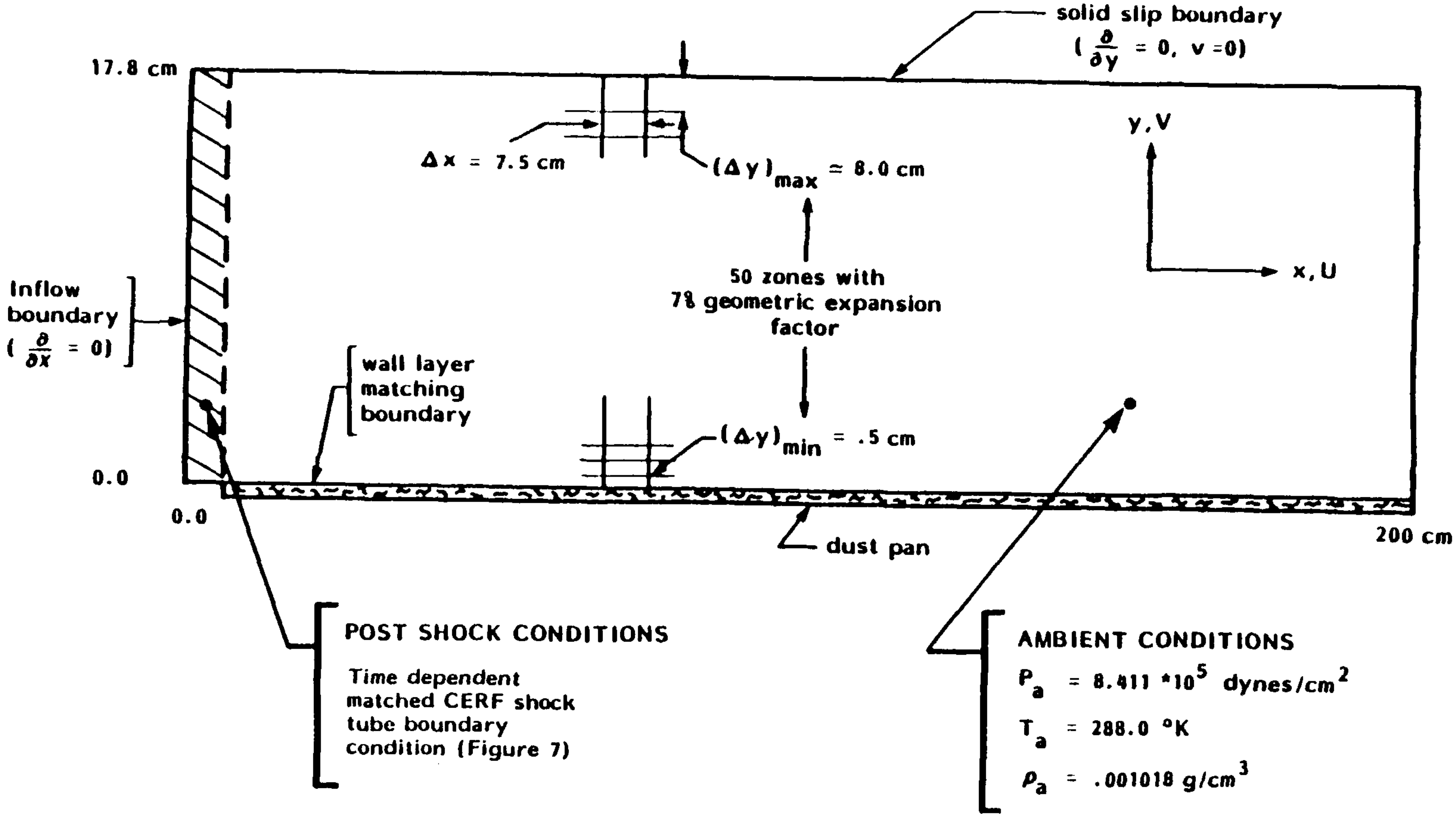

Figure 6. Engineering Scale Shock Boundary Layer Simulations Computational Set-up, Zoning, and Initial Conditions.

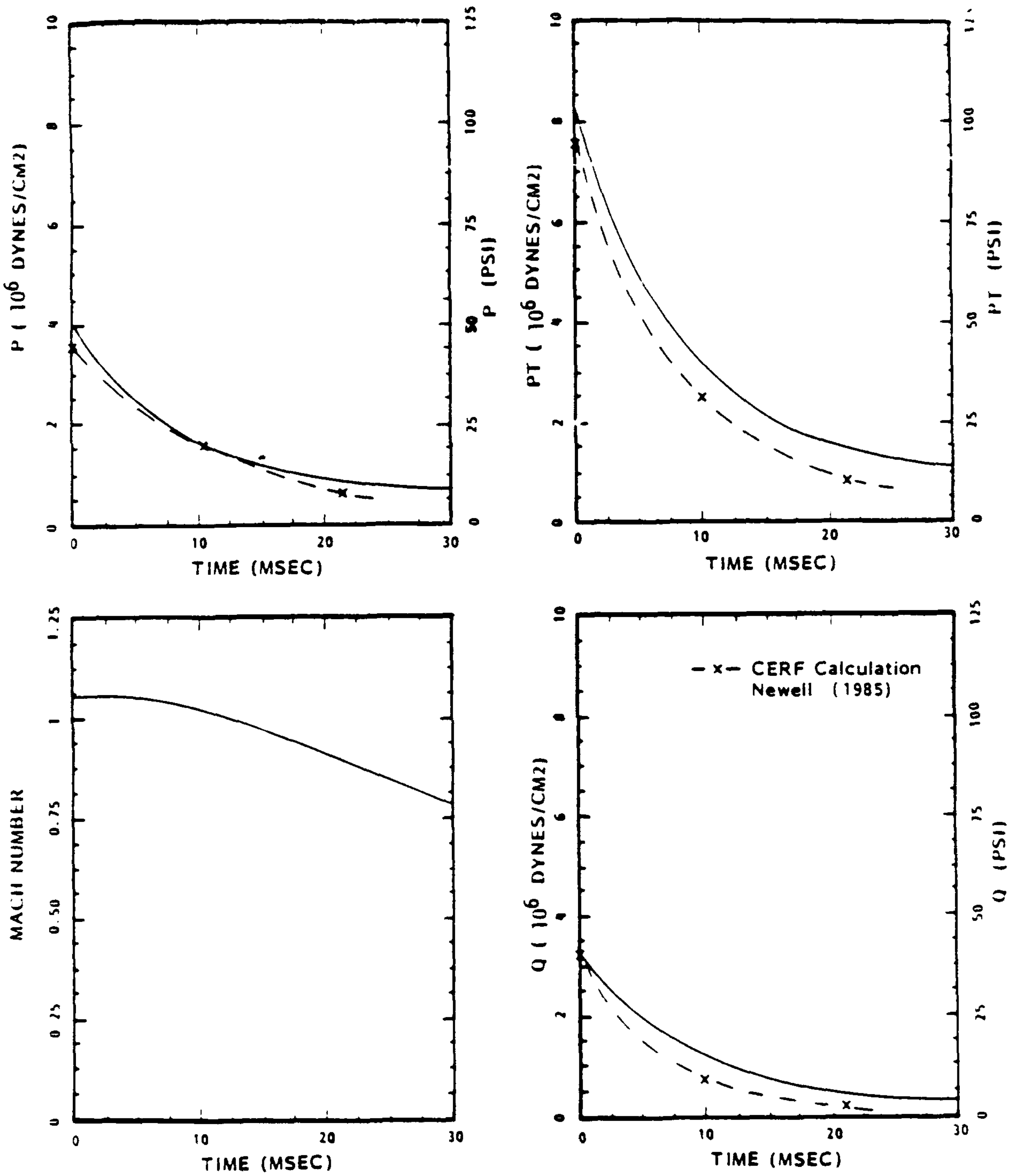

Figure 7. CERF Driver Waveform Flow Properties - Empirical Data Fit at x = 110 ft. Station.

The initial conditions consist of ambient air and a 5 inch thick helium layer extending from the 2 m axial location to the 15 m end of the region. The multi-species flow capability of MAGIC was used to simulate both helium and air components. No attempt was made to simulate the mass of the mylar bag separating the helium layer from the ambient air. Also, the two turbulence quantities were initialized assuming a low level of fossil turbulence with an intensity of u′ = 10 m/sec and scale of 2 mm.

Boundary conditions are also indicated in Figure 6. Boundary layer effects on the top boundary are neglected and an inviscid, solid slip boundary condition is imposed. The right boundary is treated as an outflow boundary with zero gradient conditions used for all flow quantities. The shocktube floor is simulated along the bottom domain boundary using the wall layer matching condition described above. The floor is assumed to be characterized by a 2 mm roughness height. Finally, the inflow boundary, which defines the driver waveform, was specified by defining all flow quantities based on time dependent exponential fits to the actual measured data at locations upstream of the test section. These fits may be termed best approximations to the upstream conditions, since only noncoincident static and total pressure measurements were available. Also a third property is required to define uniquely the flow at a fixed location, since the flow behind a decaying shock is non-homentropic. These data fits are shown in Figure 7 along with the CERF facility calibration calculations of Newell (1986) which were correlated to a range of shocktube data sets. As noted, the data fits compare favorably with Newell′s calculations and thus the inflow conditions described in Figure 9 are believed to provide an adequate description of the actual time dependent flow properties within the shocktube.

Additional boundary conditions consisted of a reflective tube ceiling, an outflow right boundary and a fully rough tube floor. Law-of-the-wall matching at the tube floor prescribed the relevant flow variables at this boundary. Dust entrainment followed the entrainment model described in the previous section with a correlation coefficient for mass entrainment of 0.75 and an injection velocity determined by the local turbulent friction velocity.

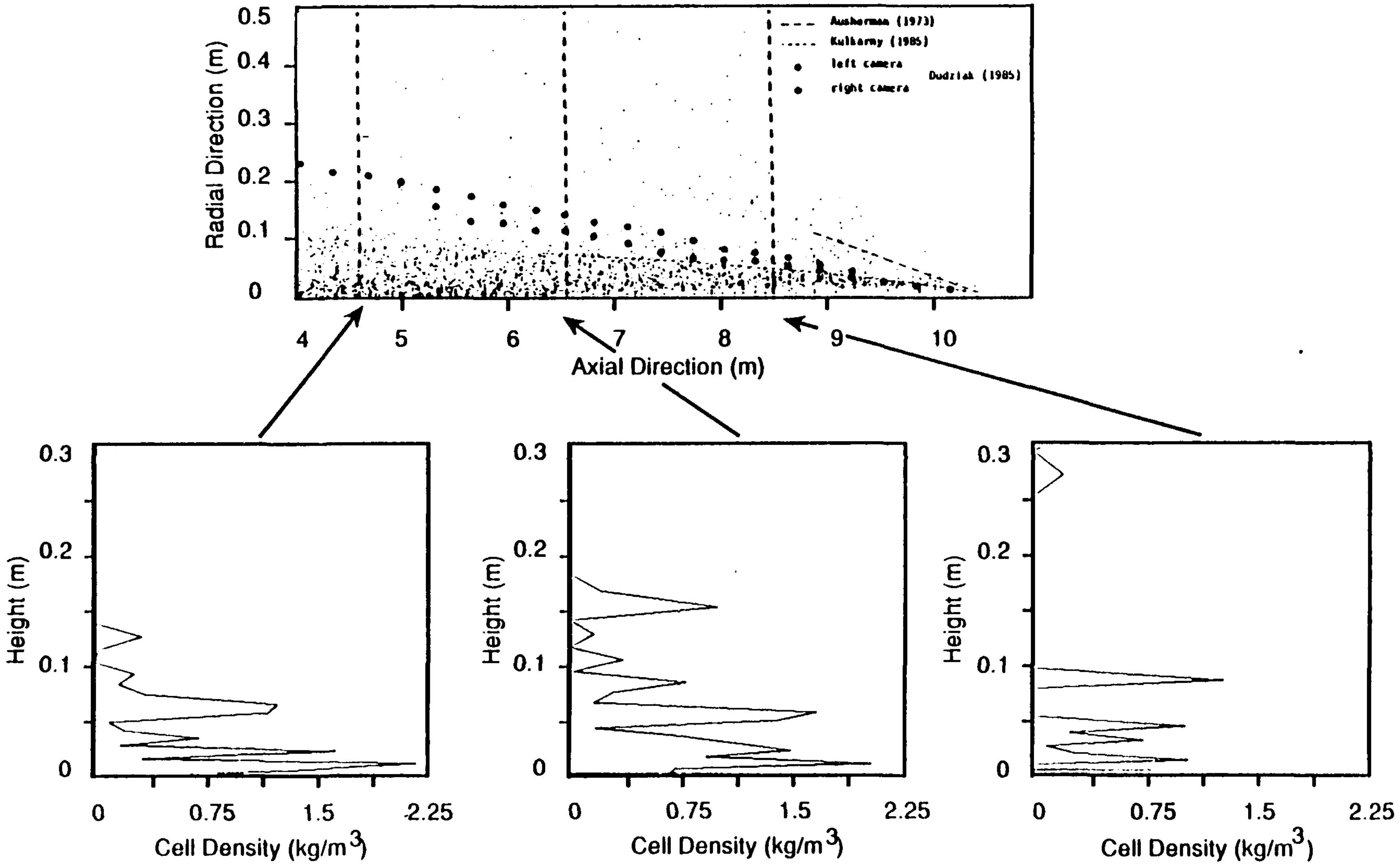

Figure 8. MAGIC Simulation of Ideal Waveform Dusty Boundary Layer CERF Test HST6-89.

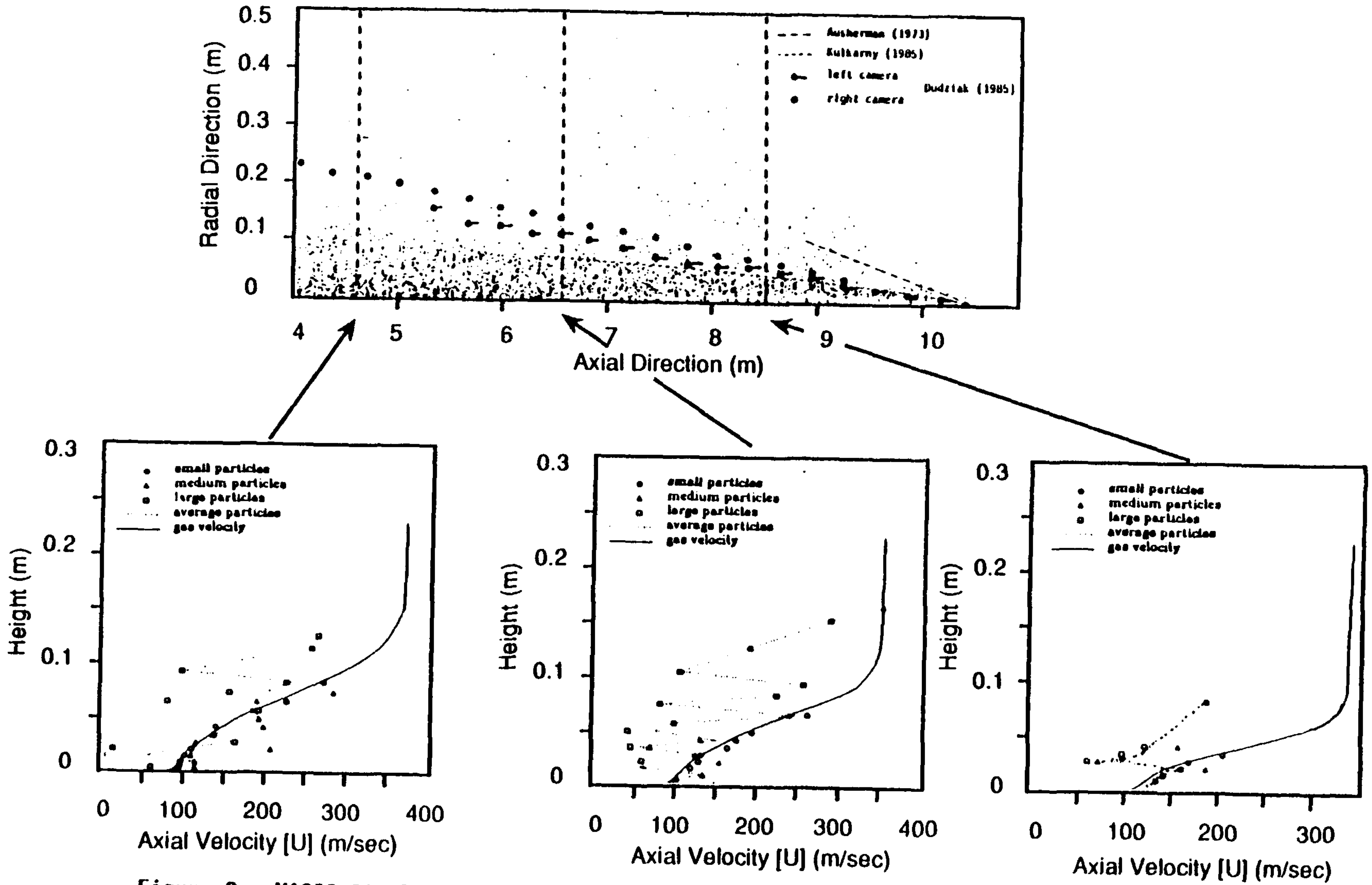

Figure 9. MAGIC Simulation of Ideal Waveforms Dusty Boundary Layer CERF Test HST6-89.

Figure 8, depicts the particle cloud and vertical variation in cell density (gas + dust). This "snapshot" was taken at a point when the ideal blastwave had traversed approximately 9.5 m of the dust pan. Superimposed on the dust cloud depiction are the Ausherman laser extinction data and the Kilkarny (TRW) and Dudziak (CERF tube) optical data. The high flyers in the simulation are in reasonable agreement with the Ausherman data, while the bulk of the dust within the boundary layer matches the optical data well. The cell density plots for the three transverse slices indicated in this figure show the dusty boundary layer growth with time. These plots represent the density along one column of cells with no attempt made to average the densities over several columns. The fluctuations of density with height reflect the stochastic nature of the simulations. Dust densities on the order of two times normal air density are shown to extend up to approximately 4 cm above the soil surface.

Figure 9, repeats the particle cloud description as shown in Figure 8; however, the bottom three figures display the mean particle size, particle size bin and gas flow velocities as a function of axial position and height. The small particles represent dust sizes 10 microns and smaller, while the medium particles refer to dust sizes in the 10 to 100 micron range. The large particles refer to those over 100 microns in diameter. The relative mix of particles is: 20% (by weight) small particles, 30% medium particles and 50% large particles. This mix gives a mass mean of approximately 100 microns and thus is representative of White Sands Missle Range (WSMR) soil. Referring to the three figures at the bottom of Figure 9, it may be noted that the small particles come into rapid equilibrium with the flow, while the large particles, over the ground range shown, do not equilibrate with the flow. In fact, the large particles on average lag the gas flow velocity by about 33%. The medium particles are shown to have come into equilibrium with the flow at a distance of approximately 6 m behind the shock front. With respect to the gas flow, these figures indicate that the particles cause a deficit of momentum within the near surface portion of the boundary layer. This loss of momentum in the near surface layer may prove to be important in loads calculations, since the shape of the boundary layer profile is critical in determining the flow separation point.

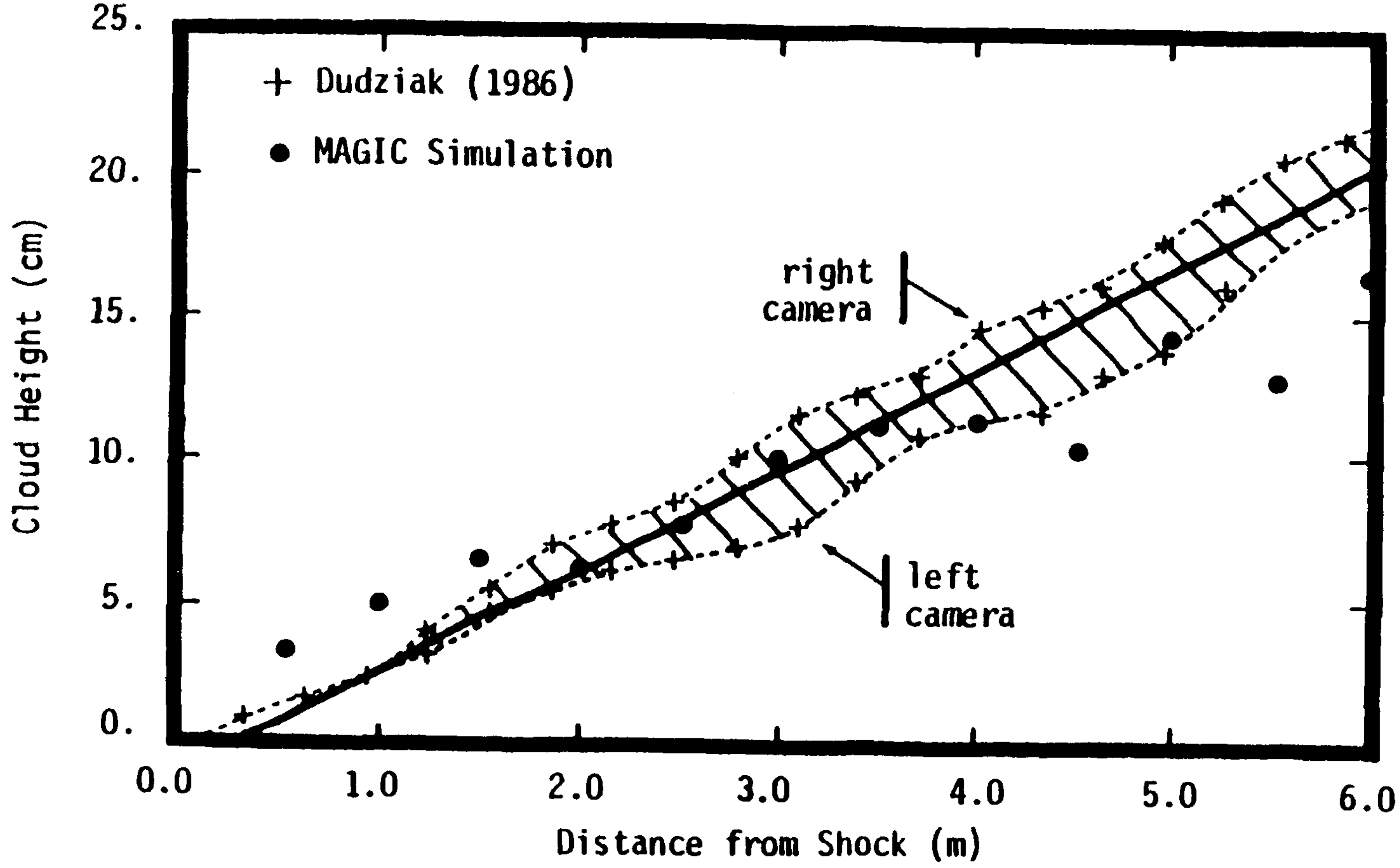

Figure 10. MAGIC Simulation of Ideal Waveform Dusty Boundary Layer CERF Test HST6-89.

Figure 10, is a restatement of the two earlier figures in that it shows the predicted and measured cloud height growth as a function of distance behind the shock. The envelope delineated by the dashed lines represents the Dudziak camera data taken on CERF test HST6-89. The heavy solid line is an approximate linear regression through these data points. The solid circles are the data from the MAGIC simulation over the region shown. Overall, the MAGIC predictions compare well with the data. As noted in this figure, the early trend is for the simulation to overpredict cloud height slightly. This slight overprediction is believed to be due to resolution in that the boundary layer height is slightly overpredicted. From 2 m to approximately 5 m, the MAGIC simulation tracks the data exceptionally well. At distances greater than 5 m, the predicted particle cloud heights fall below the data. However, this is near the beginning of the simulated dust pan in the MAGIC calculation and reflects end effects which are not present in the experimental data since in the experiment the dust pan continued well upstream of the measuring point.

The successes with simulating ideal blast wave properties including dust cloud growth and dust densities within the cloud are encouraging. Of course, the more pertinent problem is the dusty non-ideal airblast environment but unfortunately to date there are no appropriate data sets with which to compare. However, a dusty simulation of a precursed blast flow has been performed and was based on a clean flow CERF 6-foot shocktube test (HST6-39). This test case had previously been used to compare with a clean flow simulation done earlier (see Traci, et. al.; 1987). Thus, the dusty flow results can be used to qualitatively explore dust effects under non-ideal conditions via comparisons with both experiment and previous simulation results. The zoning, dust pan location, particle mix and computational domain are identical to the ideal case discussed above. Figures 11 through 14 present the simulation results.

Figure 11, displays the dust cloud particle positions along with cell density vertical profiles for three locations behind the shock. Fluctuations in the vertical profiles of dust density are due to the stochastic

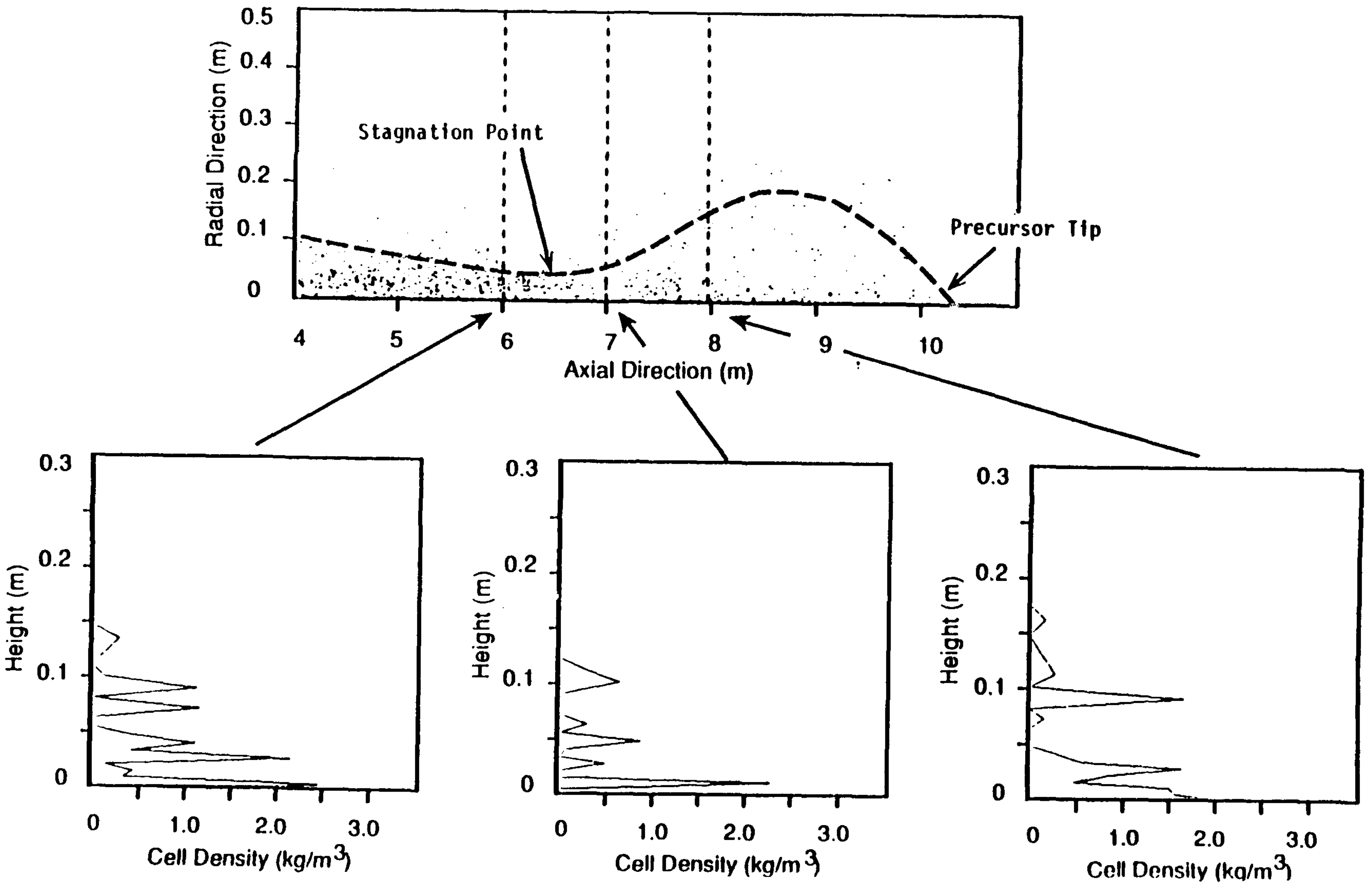

Figure 11. MAGIC Simulation of Dusty Non-Ideal Airblast in CERF HST6 Shocktube Dusty Cloud Depiction and Density Profile.

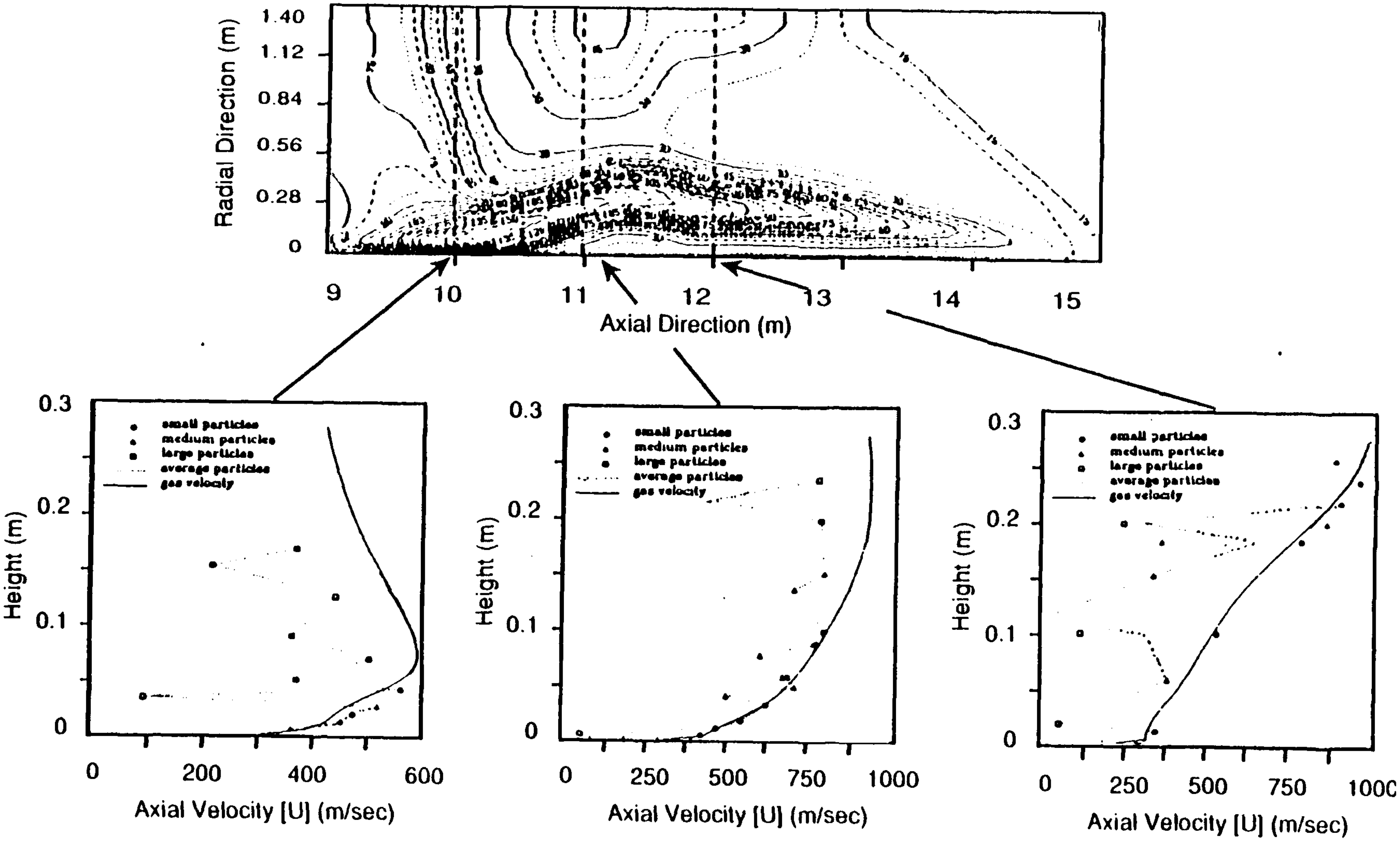

Figure 12. Gas and Particle Velocity Profiles for Dusty Non-Ideal Airblast Shown With Stagnation Pressure Distribution.

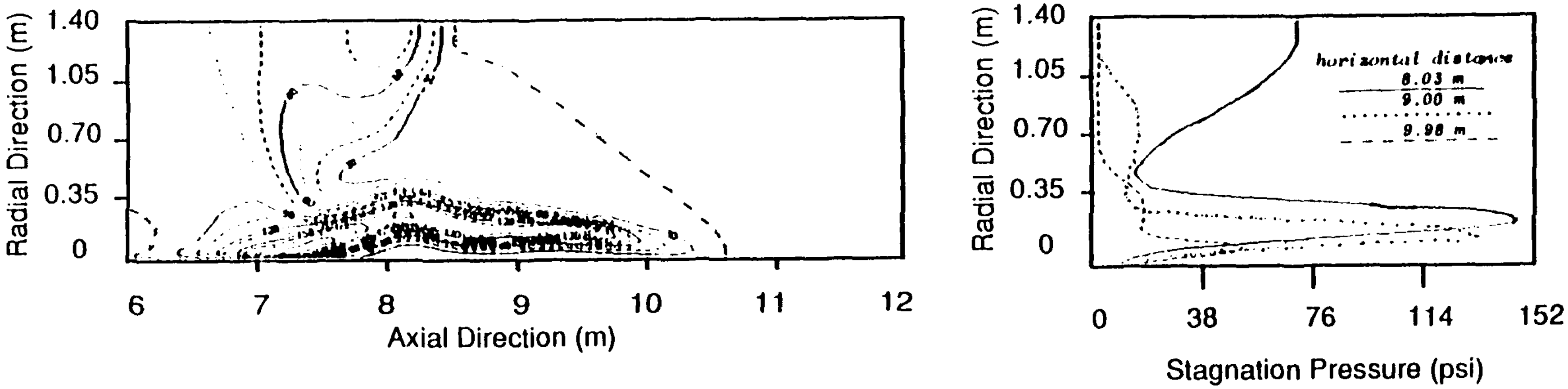

a) Dusty Precursed Flow

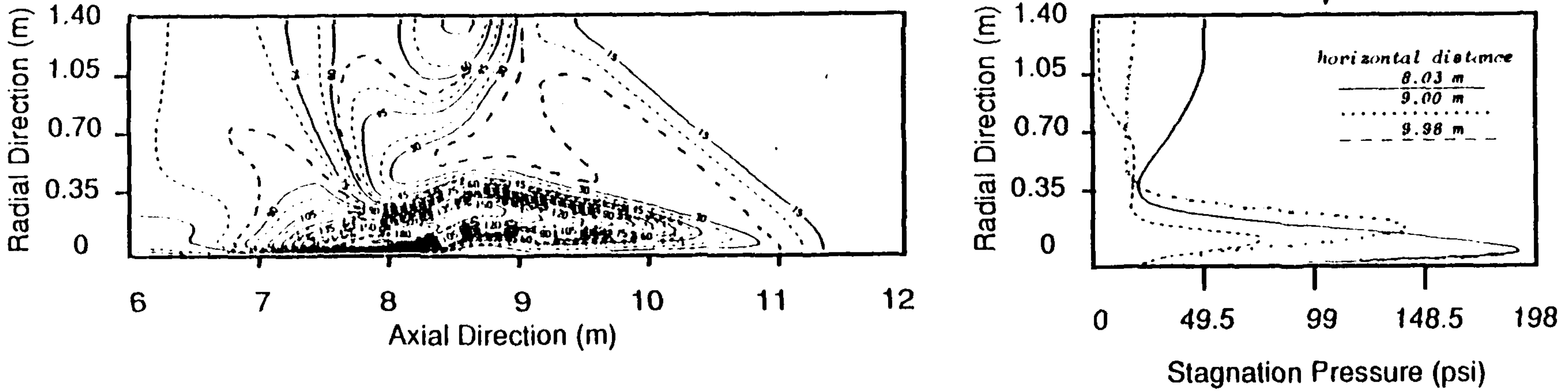

b) Clean Precursed Flow

Figure 13. MAGIC Simulation of CERF Shocktube Case HST6-39 Comparison of Dusty to Clean Flow Simulations Stagnation (total) Pressure Contours and Profiles at t ~ 10 msec.

nature of the discrete particle treatment embodied in **MAGIC** and reflect the caotic nature of the turbulent flow. Differences in the non-ideal airblast dust cloud shape when compared to the ideal case are immediately obvious. Directly behind the precursor tip (approx. 10 m) the dust rises to approximately 0.2 m as a result of the dust diffusing rapidly throughout the wall-jet structure due to the much higher turbulence levels found there. Further back around 6.5 m, the dust cloud envelope is noted to neck down to something on the order of 0.05 m. This location corresponds to the moving stagnation point and indicates that the dust has been squeezed back down towards the floor due to the vortical action of the wall jet within this region. Behind the moving stagnation point the dusty boundary layer begins to grow again behaving very much like the ideal case shown previously. The vertical profiles of total density reflect this evolution, with dust densities near the soil surface being on the order of two times normal air density.

Figure 12, displays the dusty flow evolution at a somewhat later time. The top figure in this viewgraph represents contours of stagnation pressure, giving a reference point for the three lower figures which display particle velocities and mean gas velocity at three locations within the NIAB structure. At the 12 m location it may again be noted that the small particles have come into equilibrium with the flow, while the medium and large particles are noted to lag substantially. At 11 m, however, all particles are in reasonable equilibrium with the flow. Near the stagnation point (10 m) the larger particles are lagging probably due to the fact that the flow rapidly speeds up throughout this region. Overall, however, all particle sizes appear to show reasonable equilibration.

Figure 13, compares the clean flow simulation of HST6-39 (Traci, et al., 1987) with this dusty flow simulation via stagnation pressure contours and vertical pressure profile plots. Immediately obvious from these figures is the fact that the introduction of dust has acted to remove momentum from the near surface flow, displacing the peak stagnation pressure upwards at the 8 m location. The introduction of dust has also served to lower this peak slightly

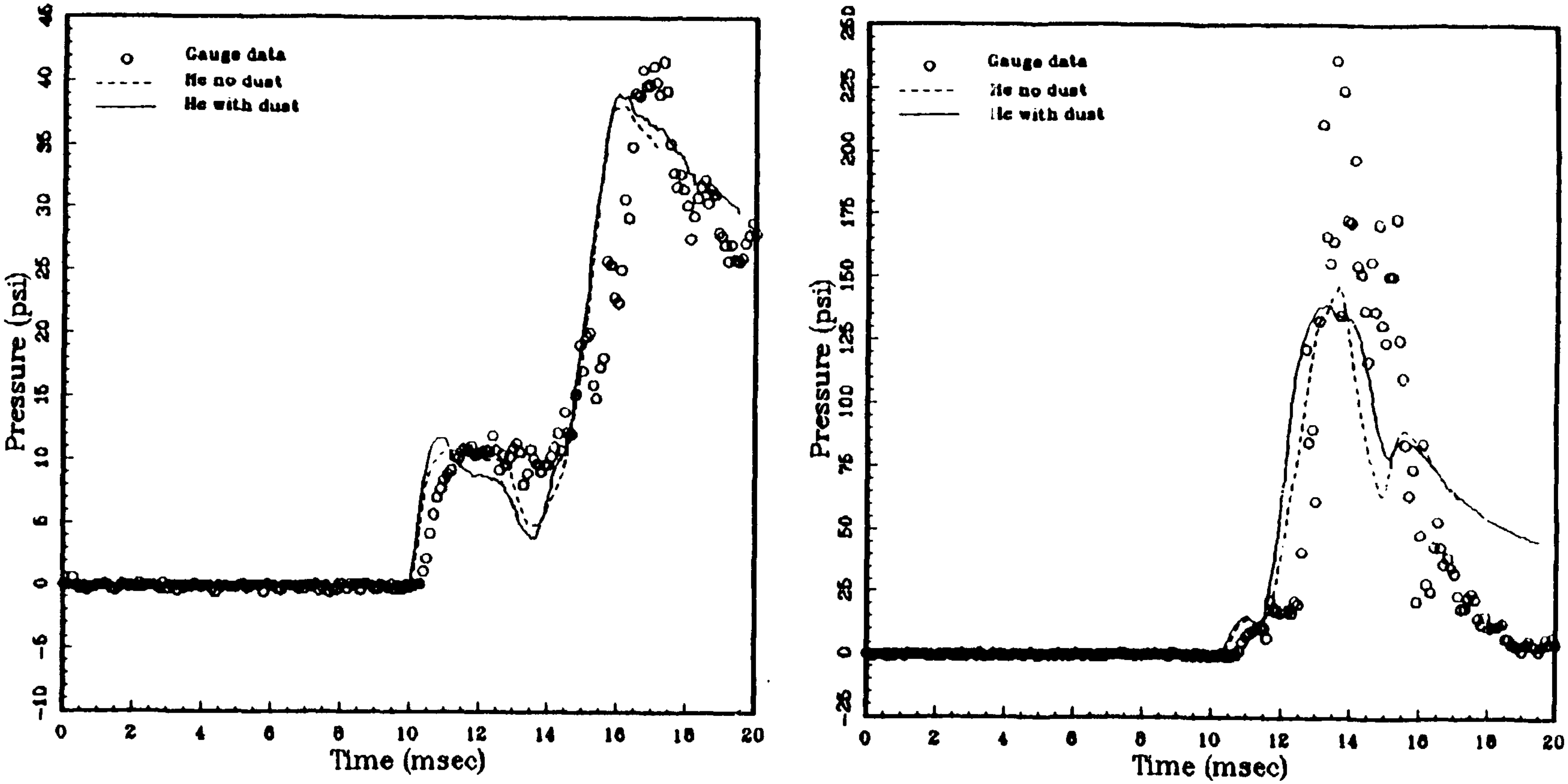

a) Static Overpressure (psi)

b) Total Overpressure (psi)

Figure 14. Dust Particle Effect on Precursed Shockwave Flowfields MAGIC Turbulent Simulations of CERF Shocktube Precursed Shock Test HST6-39 (5" Helium Layer).

from what it was in the clean flow case. The effect of these modifications on vehicle loads requires further investigation.

Finally, Figure 14 compares the clean flow measured static and stagnation overpressures with the clean flow and dusty flow predictions for HST6-39. As noted in this figure, the introduction of dust into the boundary layer has had little noticeable effect on the static pressure wave profile. With respect to the stagnation pressure, the presence of dust has acted to broaden the waveform slightly and probably reflects the upward displacement of the wall jet over that which was predicted for the clean flow case.

2.3 ENVIRONMENTS SUMMARY.

The success of the model comparisons with data gives some degree of substantiation to the assumption that dust entrainment is mixing controlled. In this concept, the effective particle entrainment rate and injection velocity both scale according to the level of turbulent fluctuations in the wall layer. That is, they are proportional to the mixing or shear velocity. The particles are thus entrained via the same turbulent diffusion mechanism that distributes them throughout the boundary layer. The particles, however, are not passive in this process. The simulations reviewed above indicate that the particles have a moderate effect on the mean velocity profile, surface shear and boundary layer thickness and a possible secondary effect on the gas turbulence properties. Each of these effects couple back to modify the fate of the dust.

The simulations have also indicated that on the engineering scale the particles exhibit significant slip relative to the mean and turbulent flow so that the cloud structure is controlled by the statistical variability in the particle injection conditions. This is a significant advantage for the discrete particle model rather than the deterministic continuum two-phase flow models in common use. However, the particle slip effect is probably only significant at the small test scales and becomes less important as the boundary layer and its principal eddies become larger as on the real world scale.

SECTION 3

HIGH-ORDER ACCURACY FCT SCHEME IN A NON-RECTANGULAR GRID SYSTEM

The Flux Corrected Transport (FCT) scheme used in both **BISON** and **MAGIC** is based on the original method of Boris and Book (1973), with modifications to the antidiffusion limiter suggested by Zalesak (1978). The basic one-dimensional algorithm is extended to multidimensions by using an explicit spatial operator splitting technique. This not only allows an efficient solution algorithm to be built via successive application of one-dimensional solutions in each of the coordinate directions, but also, as will be discussed in the next section, has the advantage of treating the non-rectangular grid system in the one-dimensional sense. The FCT scheme in both codes was originally implemented based on the assumption of a rectangular grid system.

For the treatment of an arbitrary flow domain, **BISON** maintains rectangular grids by approximating curve boundaries with stairstep boundary cells. Some reasonable number of grid points at boundaries are thus needed to obtain acceptable accuracies. In **MAGIC**, the arbitrary flow domain can be smoothly approximated by the quadrilateral cells in its generalized coordinate system. However, direct application of the high order accuracy scheme forces the flow domain in **MAGIC** to be strictly rectangular. This restriction defeats some of the versatility of the **MAGIC** generalized coordinate system. For a complicated flow domain, a coordinate transformation is often preferred to transform the irregular domain into a rectangular one. The FCT scheme can then be applied to solve flow variables in this transformed plane. However, the transformation process, in general, computationally time consuming.

An alternative approach to a full transformation of an irregular domain into a regular one is considered here. Because the domain boundary is regular on three sides and includes an arbitrary flow obstruction coincident with the ground plane on the fourth, it is advantageous to consider a "sheared coordinate system" and work entirely in the physical plane. By sheared it is meant that one set of grid lines remains non-curved and parallel, while the other set allows for curvature and converging or diverging grid line segments. This approach has the advantage of eliminating coordinate transformations, but has the disadvantage that the FCT algorithm cannot be applied directly in its standard form.

In order to extend the capability of FCT to treat a "sheared coordinate system", a modified scheme based on simple interpolations of flow variables from non-rectangular grids into rectangular grids was developed. Through its simplicity, it has the advantage of being economical and straightforward to implement, allowing the high-order accuracy of FCT to be efficiently exploited on non-Cartesian grids. Details of the approach are given in Subsection 3.1. Demonstration and validation simulations obtained by applying this modified FCT scheme are found in Subsection 3.2.

3.1 DESCRIPTION OF FCT SOLVER IN NON-RECTANGULAR GRID SYSTEM.

The essential idea of FCT is the application of a corrected diffusive flux to a dispersive transport scheme. The technique localizes the addition of diffusion to only those regions where non-physical oscillations form as a result of dispersive errors. A basic FCT algorithm consists of three finite-difference operations: a transport, then a diffusion, followed by an antidiffusion. For second order accuracy, all these operations can be approximated by three-point formulas. That is, all finite difference operations can always be expressed as a function of the variable being differenced at the three adjacent grid points in the same i-row or j-column of the grid system. The methodology of applying the original FCT scheme in the non-rectangular grid system is based on finding the best adjacent values of the variables to be used in the finite-difference formulas and flux-correction step of the FCT operations.

Figure 15 shows a typical non-rectangular grid system with point C denoting the grid point (i,j) where flow variables are being integrated. Points R and L are the two adjacent points in the i-direction of the FCT calculation.

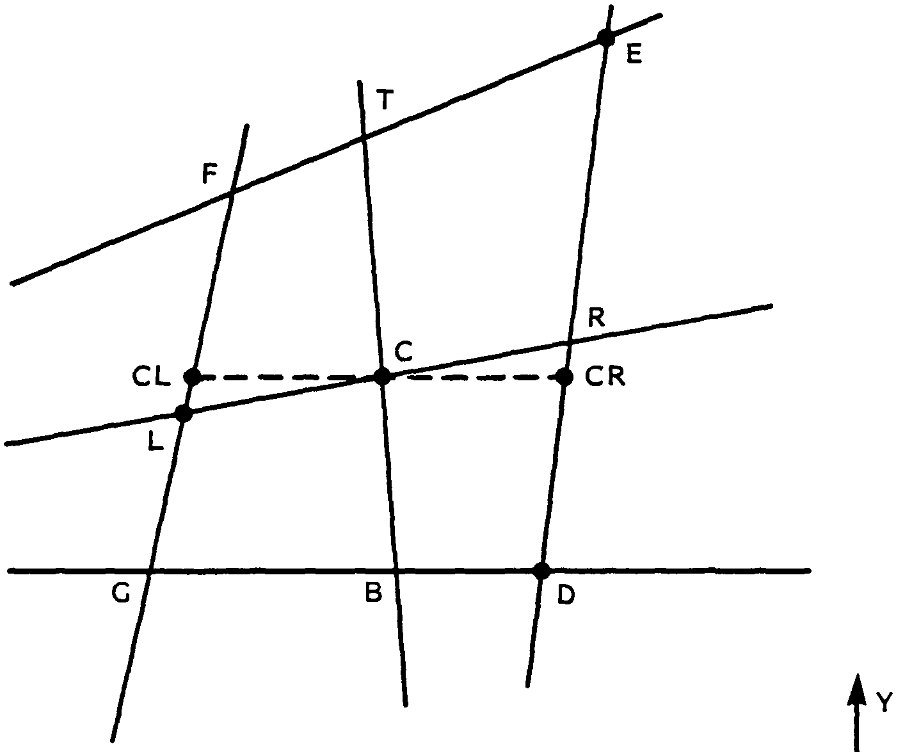

Figure 15. Typical Non-Rectangular Mesh Element.

while points T and B are its two connecting points in the direction transverse to the i-direction. Since explicit spatial operator splitting is employed in the FCT algorithm used here, it is necessary to consider only differencing modifications of the non-rectangular FCT solver in one direction. For the purposes of this discussion, the x-direction is assumed. The extension of the modified FCT scheme to other directions is straightforward. In order to get the correct values of fluxes across point C in the x-direction, a line is drawn past point C and parallel to the x-axis. The intersection points of this line with two adjacent cell faces are designated as the points CR and CL in the figure. If all the values of flow variables in each step of the FCT operation can be accurately evaluated at these points, the FCT scheme in any one of the coordinate systems can be applied correctly. The main task of this modified FCT scheme is thus to calculate accurately all flow variables or fluxes at these points at the beginning of every step of FCT operations.

Assuming all flow variables are known at all grid points at some integration time level, the most efficient method for calculating the unknown values of these variables at points CR and CL is by interpolating. If the slope of RL with respect to the x-axis is not too large, point CR should always lie in the segment connecting points E and D. A three-point (points E, R and D) quadratic interpolation formula, in this case a Lagrange formula, is used to maintain second order accuracy for the interpolated variables at point CR for interior mesh points. The Lagrange three-point scheme applied near a boundary with zero gradient boundary conditions will give erroneous overshoot or undershoot solutions for the boundary cells. Therefore, a lower order interpolation scheme (linear) at flow boundaries is used to prevent this from happening and thus assure robustness in the technique.

It is obvious that the use of interpolation provides correct values of transportive, diffusive and antidiffusive fluxes at all grid points in any coordinate direction. It is equally obvious that the order of accuracy is dependent only upon the order of interpolation applied, though as noted above the higher the order of the interpolation algorithm, the more difficult it is to apply appropriate and consistent boundary conditions. The only remaining uncertainty in the proposed approach is the treatment of the flux limiting step of the original FCT scheme. In the flux limiting step of the modified scheme, the antidiffusive fluxes into or away from grid points are calculated by applying Zalesak's algorithm in one spatial dimension with the antidiffusive fluxes at adjacent grid points being replaced by the interpolated values. Since the interpolated values are always used in the evaluation of fluxes, the maximum and minimum values of the conserved variables are determined by comparing the grid point value with the interpolated values at two adjacent points in the antidiffusion operation. Although explicit effort has been made to investigate the effects of the interpolation procedure on the critical flux limiting step in FCT scheme, the results obtained, by applying this approach to the fluid flow calculations appear to give acceptable accuracy, as evidenced in the validation study discussed in the next section, without introducing additional dispersive errors.

The additional overhead incurred in applying this modified scheme to solve the flowfield in a non-rectangular grid system is very small. Since point CR is always bounded by points E and D when the three point interpolation is used, decision-making, always a time consuming expense in more sophisticated approaches, is avoided in the calculation. It is emphasized that the economy of the approach along with its accuracy were paramount in selecting a viable scheme. Among other factors this meant that all logic added to the current FCT algorithm must meet the criterion of being fully vectorizable. The current procedure meets this goal.

This discussion of the necessary modifications to the FCT scheme to provide an approach suitable to non-Cartesian geometries is intended to present the basic concept of applying interpolation to obtain a regular grid from a non-regular grid on a point-by-point basis. The use of Lagrange and linear interpolation to achieve this goal are but two of the many interpolation algorithms available. Further, should highly skewed or completely general grids be necessary, more sophisticated logic for determining the local regular grid would be necessary. For example, if the slopes of the grid lines are not continuous, second order interpolation cannot be achieved without the employment of a two-dimensional formula, rather than the one-dimensional techniques in use here. The restriction of the current algorithm to moderately skewed grids is one of economy and convenince. In addition to the implementation of alternate interpolating algorithms or more sophisticated logic for treating highly non-regular grids, the selection of optimum values to interpolate could also be explored. That is, the current scheme considers the interpolation of the conserved variables. An alternate scheme might consider the interpolation of the fluxes of the conserved variables, rather than the variables themselves. Thus, it can be seen that the current scheme can take on many variations, and possible refinements of the scheme are valid areas of future study. However, as will be shown in the next subsection, the basic non-rectangular FCT solver developed here is capable of maintaining the suitable computational accuracy for problems of interest to near surface airblast study, and this accuracy is obtained without incurring significant computational cost.

3.2 SAMPLE PROBLEM USING NON-RECTANGULAR GRID WITH FCT.

An ideal test problem for validating the modified FCT scheme on a non-rectangular grid system is the prediction of oblique shock reflection in a high Mach-number flow. This flow possesses the pseudostationary property; i.e., flow variables are self-similar, which facilitates model comparisons with either experimental data or other computational solutions. Further, the flow regime and shock characteristics are highly similar to airblast Mach reflection for non-zero heights of burst.

The problem is defined as follows. A Mach 10 shock in air (ρ = 1.4) travels from left to right, originating in a straight inlet section and impinging on a 30 degree two-dimensional wedge. The interaction of the shock with the wedge produces a reflected shock.

The computational domain was chosen such that the upstream bottom boundary and the wedge surface were conformal to the computational boundary. The grid in the wedge region thus has non-rectangular elements. Two alternate

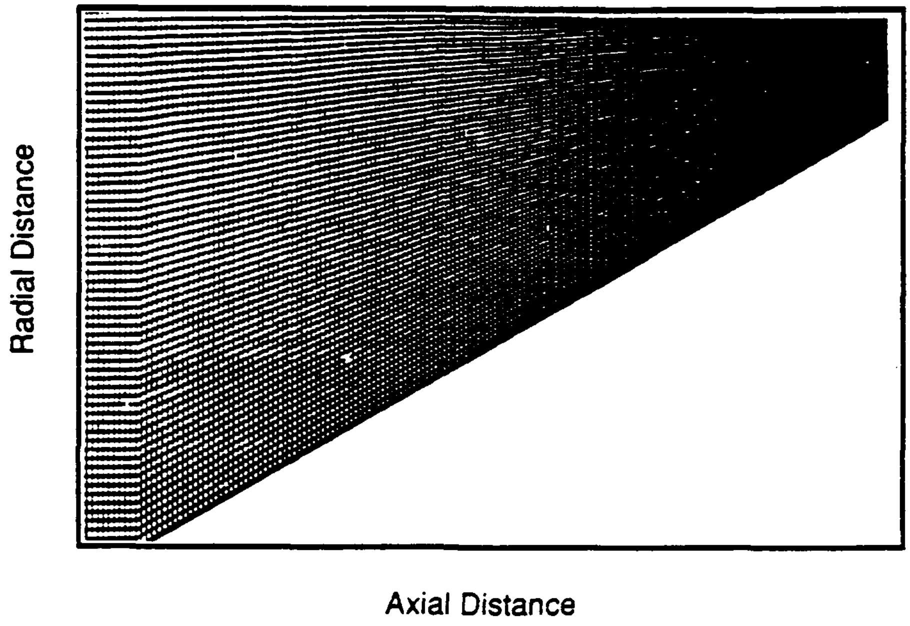

a) Non-Rectangular Configuration 1

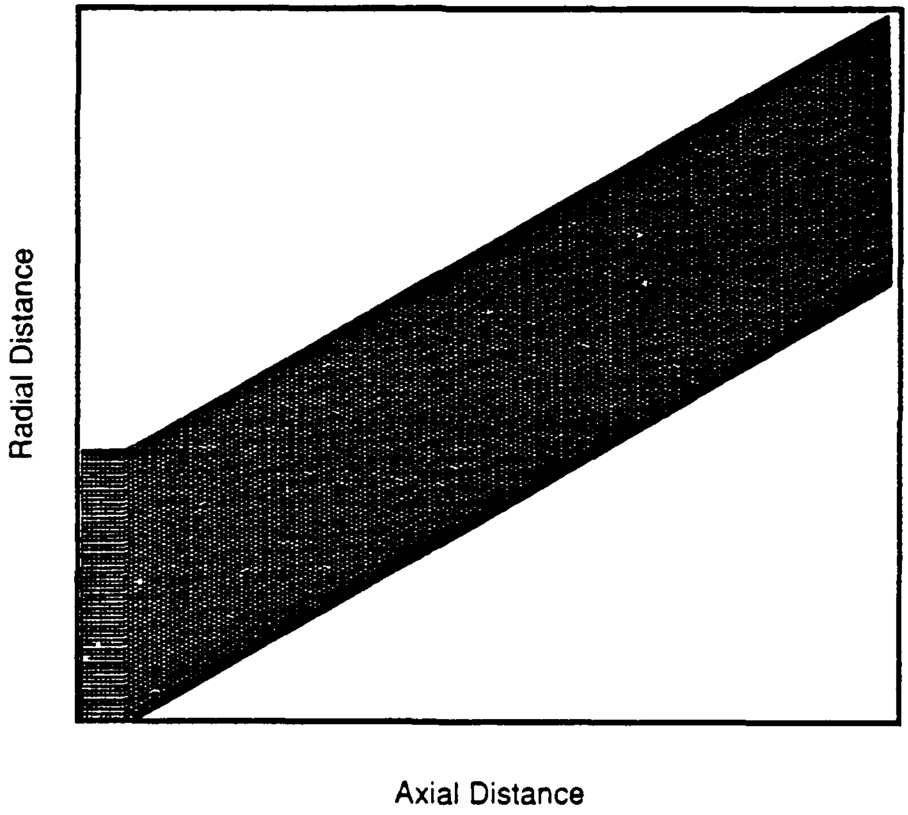

b) Non-Rectangular Configuration 2

Figure 16. Computational Grid Systems Used for the Simulation of Oblique Shock Reflection.

non-rectangular grids were investigated. The first had the top boundary aligned with the incoming flow direction, yielding a converging computational grid system as shown in Figure 16a. This results in a coarser grid near the inlet section with the grid continuously refining downstream of the inlet section. The second non-rectangular grid system, shown in Figure 16.b, was constructed to yield constant grid sizes in both horizontal and vertical directions. Both grids represent "skewed" gridding, and it was the intent to investigate the effect of alternÃte skewed gridding geometries on the predicted flow field. The left boundary for both cases was assigned the values of the initial Mach 10 post-shock flow to force the reflected shock to remain attached to the wedge surface. An outflow, or zero gradient, boundary condition was used for both the top and the right boundaries. At the bottom wall, a reflective boundary condition normal to the wedge was imposed.

Contour plots of flow variables at non-dimensional time 6.33 are shown in Figures 17 through 19. In each figure, the upper plot displays the results obtained with the grid system shown in Figure 16a, while the lower plot shows the results for the Figure 16b grid system. For this combination of incident shock strength and wedge angle it is expected that the resulting shock-wedge interaction would produce a double Mach stem structure. It should be noted that by varying the wedge angle and Mach number, the reflected shock may be either regular or any one of several types of Mach reflection. This structure is clearly evident in these figures. In addition, the slipstream lines (contact discontinuities) are in evidence in the density contours shown in Figure 17. Referring to Figure 17, the first Mach stem and contact discontinuity are well resolved in both simulations. The second Mach stem, although weak, can also be identified from the plots. Like many other numerical methods, the second contact discontinuity extending from the second triple point is too weak to be resolved.

Compared to the thickness of the incident shock, the reflected shock is shown to be broader for both grids and is probably due to the fact that in the vicinity of the reflected shock the flow direction is not aligned with the grid. Further, the staircase structure along the reflected shock is thought to be a function of both the grid resolution and the characteristic of the

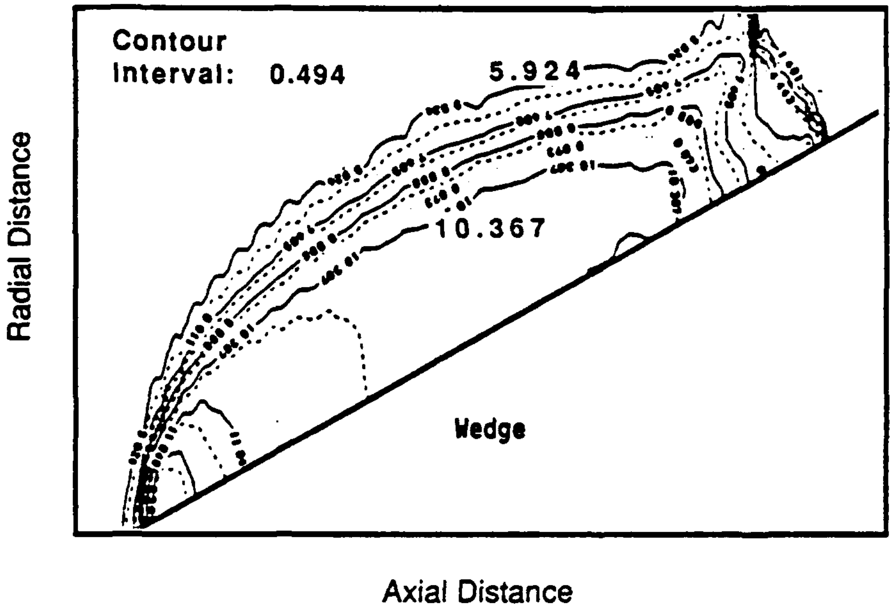

a) Non-Rectangular Configuration 1

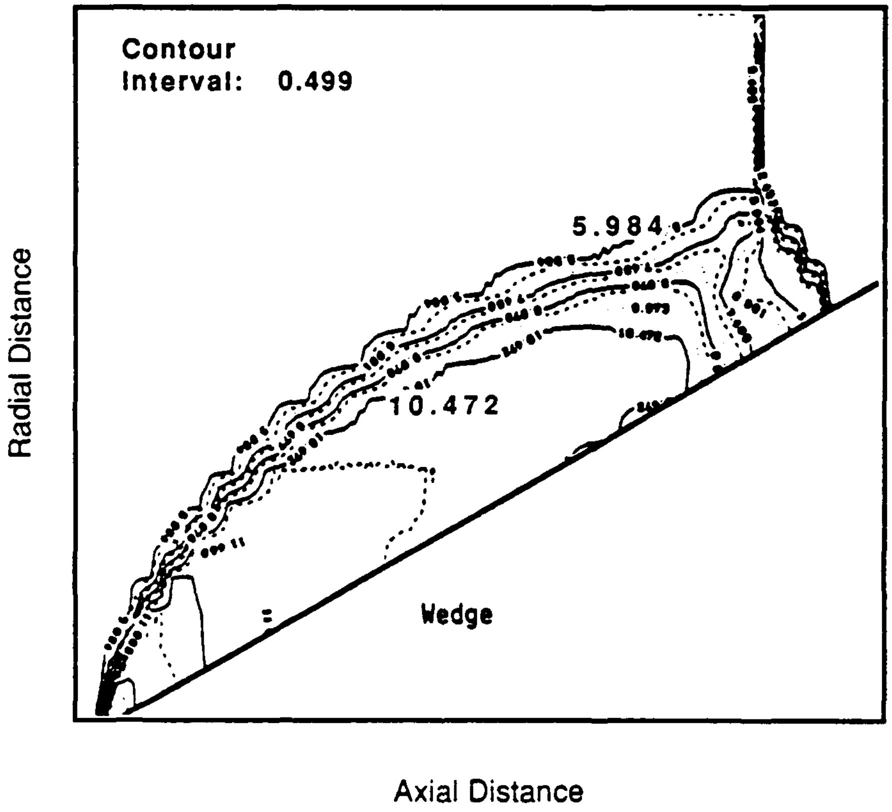

b) Non-Rectangular Configuration 2

Figure 17. Density Contours of Oblique Shock Reflection on a 30° Wedge.

current monotonicity constraint imposed as part of the spatially split FCT scheme applied to multi-dimensional flows.

In addition to the flow similarities noted above, there are flow differences between the two gridding schemes. Comparing Figures 17a and 17b, it is noted that the leading shock in Figure 17a is smoother than its counterpart in Figure 17b. This is probably a result of the higher resolution within this region employed in the first grid system. Additionally, the forward moving wall jet, discernible in Figure 17a, is not in evidence in Figure 17b, again due to resolution differences. Overall, however, the two gridding systems appear to yield substantially similar results, at least in terms of density profiles.

Pressure contours at the same computational time are shown in Figure 18a and 18b for both grid systems. These figures indicate larger variations in the flow structure for the two grid systems. In Figure 18a, there appears to be some boundary influence on the flow due to the gridding near the wedge surface. This is not in evidence in Figure 18b. These differences may be due to the converging nature of the first grid system. Finally, the fluid speed contours are shown in Figures 19a and 19b. Two Mach reflection structures can also be observed from these plots. The location of the first contact discontinuity can be seen clearly, whereas the second contact discontinuity can be only vaguely identified in Figure 19.

Comparing these results with those obtained by other numerical models (for example, Collela and Woodward, 1984) for the calculation of an oblique incident shock reflecting from a horizontal wall, it may be noticed that the shock structures in this study are slightly more dissipative than those predicted for a rectangular grid system. However, this is expected since an interpolation scheme, which is always dissipative, is used in the modified scheme for a non-rectangular grid system. Further, the application of splitting on grid systems not strictly aligned with the flow produces additional numerical inaccuracies. For complicated flow structures, strict flow alignment with the grid can never be realized, and thus there will always remain some inaccuracy. Overall, however, it is important to point out that this modified FCT scheme has

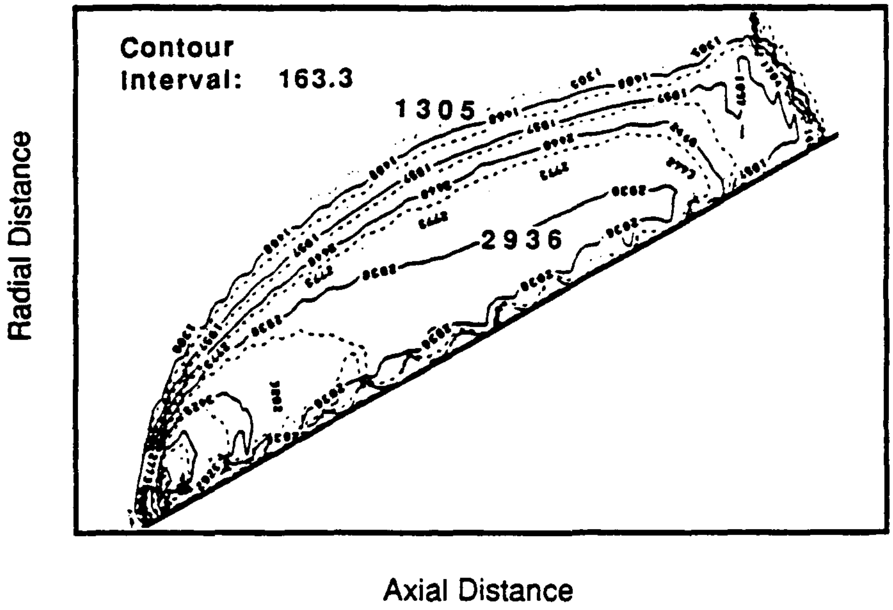

a) Non-Rectangular Configuration 1

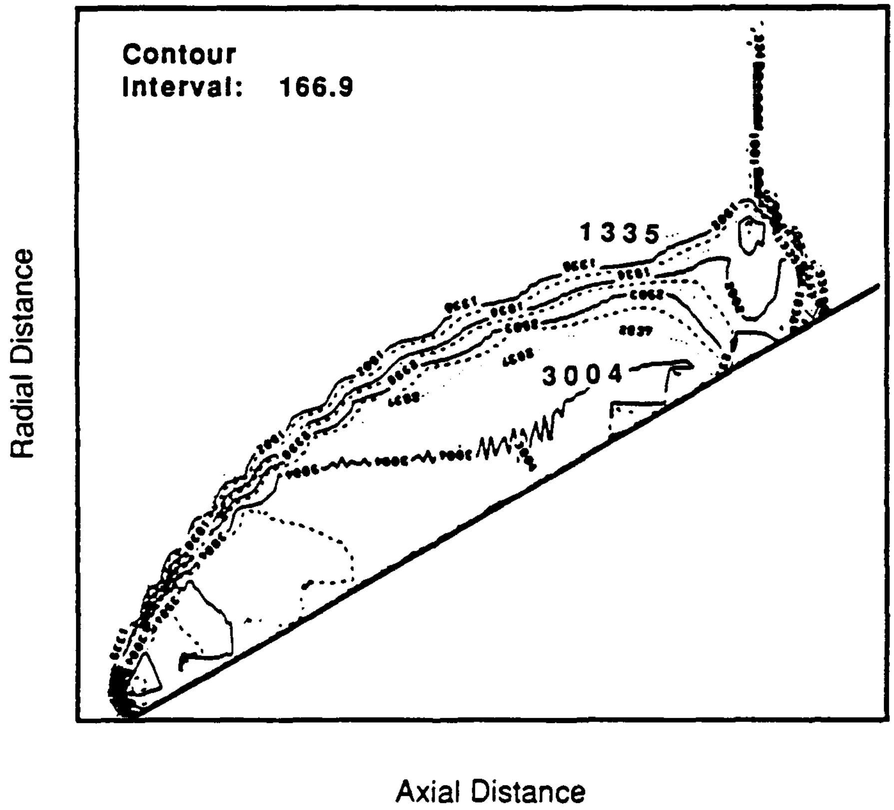

b) Non-Rectangular Configuration 2

Figure 18. Pressure Contour of Oblique Shock Reflection on a 30° Wedge.

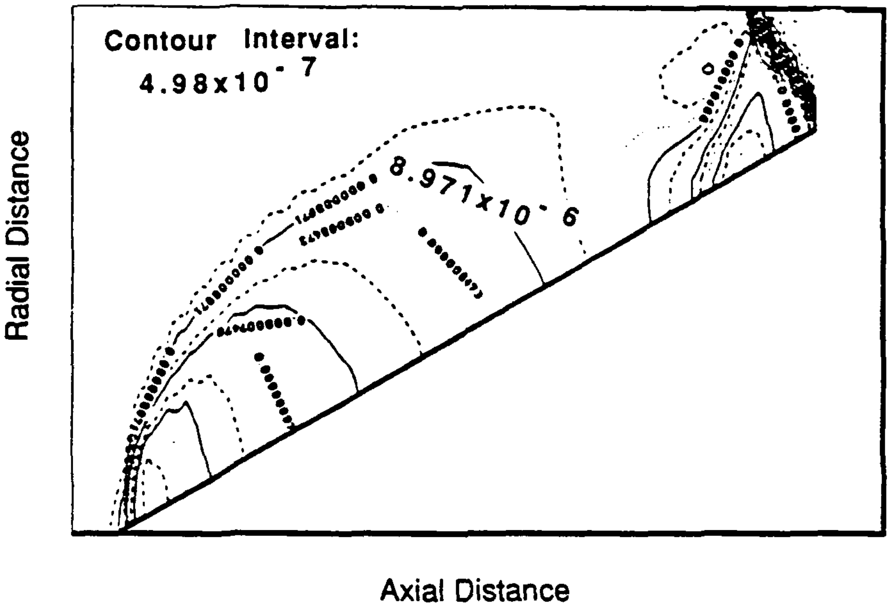

a) Non-Rectangular Configuration 1

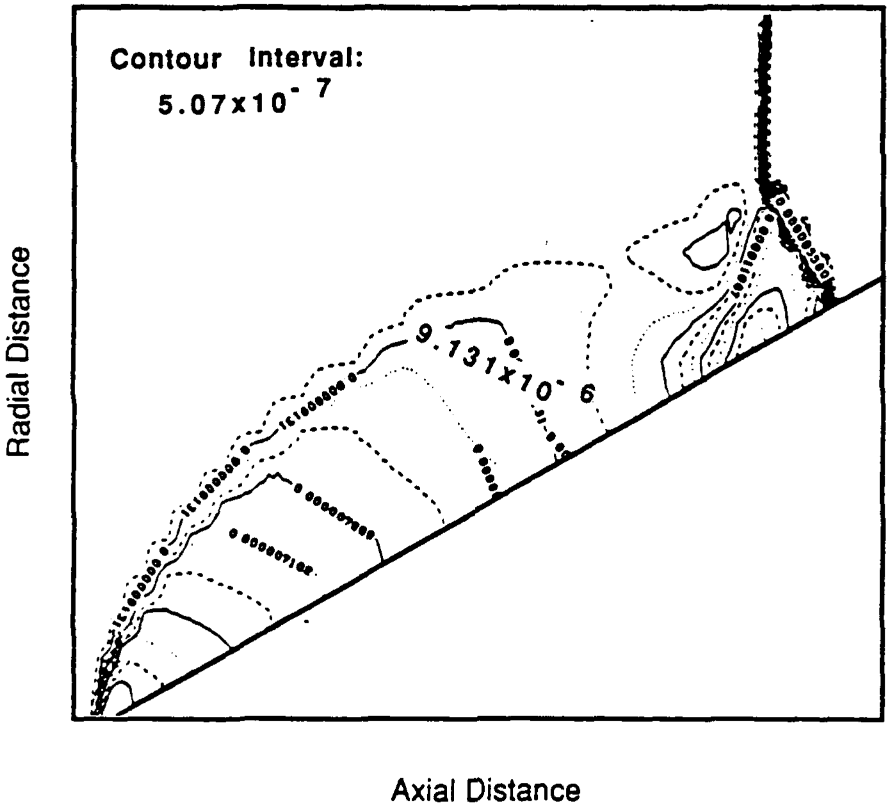

b) Non-Rectangular Configuration 2

Figure 19. Flow Speed Contours of Oblique Shock Reflection on a 30° Wedge.

been able to resolve most of the important flow structures for a complex oblique shock reflection problem by the use of a simple and efficient modification to the algorithm employed in the **MAGIC** model.

SECTION 4
LOADS SIMULATIONS IN DUSTY FLOW ENVIRONMENTS

Numerical simulations of non-ideal airblast flows around HML bodies using the **MAGIC** numerical model, which are the basis for vehicle load predictions, are typically performed using a "sequential multi-grid" approach. As noted in Section 2, this involves the interfacing of turbulent Navier-Stokes simulations of the near surface flow field (the driving force) with the vehicle flow field solution (the driven flow). This approach is motivated by the differing resolution requirements that exist between the relevant flow regimes, from the high resolution needs in the immediate vicinity of the quasi-bluff body to the much larger characteristic length scales associated with the global blastwave flow.

In a prior study (Traci, 1987), the sequential multi-grid was successfully demonstrated for a set of NMERI CERF experiments in the six foot horizontal shocktube. The objective of these calculations was to assess the quality of the **MAGIC** program predictions for the aerodynamic loads experienced by typical HML configurations in a clean non-ideal airblast environment using the CERF engineering scale measurements as a basis for comparison. The hallmark calculation in this study consisted of a solution for test case HST6-38 which involved an instrumented 5 inch radius circular cylindrical model subjected to a 50 psi overpressure blastwave and the non-ideal environment resulting from a 5 inch high layer of helium extending upstream and downstream of the model. A detailed discussion of the numerical simulation for this test condition is included in Traci (1987), and a comparison of the predicted and measured force component histories are shown in Figure 20 for this non-ideal airblast environment. The agreement is generally quite good. The maximum lift and drag levels are accurately predicted, and the waveform histories agree favorably, especially that for the lift force component. (At late time, the horizontal force component comparison does not compare as well because the quasi-steady drag, based on the integration of the pressure measurements, is unexplainably near zero for experimental data).

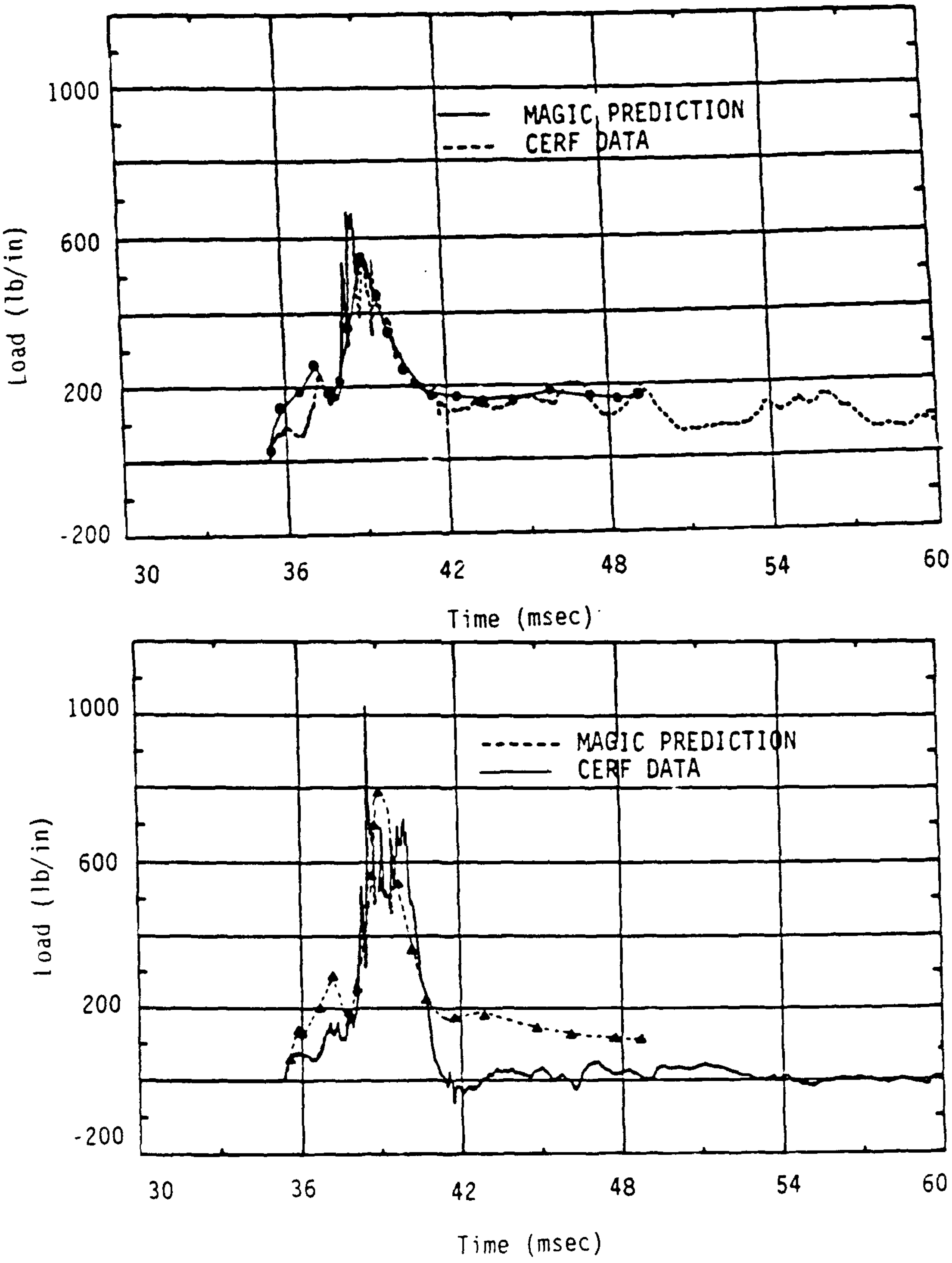

a) Lift force component.

b) Drag force component.

Figure 20. Comparison of MAGIC prediction and measured force component histories for HST6-38 (5" helium layer).

Comparisons of surface pressure distributions around the model were equally favorable, which indicate that the detailed flow physics around the model are correctly simulated. A number of parametric/sensitivity calculations also demonstrated that the success of these comparisons is critically dependent upon the number of the higher order models in the **MAGIC** code, namely:

- **a higher order advection scheme (FCT)**
- **a dynamic two-equation (k-w) turbulence model**
- a multi-species transport (for the helium layer shocktube experiments)
  and
- the sequential multi-grid formulation.

Based upon these results, it was concluded that the **MAGIC** model can accurately simulate, at the engineering test scale, semi-bluff-body loads in a clean non-ideal airblast environment.

The principal thrust of the current study was then to extend the assessment and applications of the sequential multi-grid methodology employing the **MAGIC** code for load predictions in non-ideal environments that contain dust. Section 4.1 describes an extension of the sequential multi-grid interfacing methodology which was required for flow fields which contain particulates. Section 4.2 presents the results of the **MAGIC** simulation for the dusty non-ideal airblast flow around a typical HML bluff body, the purpose of which was to assess and demonstrate the accuracy of **MAGIC** predictions at the engineering test scale. Finally, Section 4.3 demonstrates the ability of **MAGIC** to perform non-ideal airblast (NIAB) HML load calculations for the full scale environment.

4.1 DUSTY FLOW SEQUENTIAL GRID TECHNNIQUE DEVELOPMENT.

The sequential multi-grid methodology has proved highly accurate for the prediction of loads on vehicles in clean flow. The technique should prove just as accurate in two-phase flows, but in order to apply it to these flows, some model generalizations were necessary to insure that all dusty flow parameters were properly transmitted from Region I (environment domain) to Region II (vehicle domain).

For two-phase (dusty) flow, **MAGIC** considers a Monte Carlo solution for particle transport and dispersion. The treatment provides for full coupling between the particles and the gas via a complete set of Lagrangian dynamic equations for the particle motion. Turbulent dispersion effects are included and make use of local turbulence properties. The consideration of two phases adds additional flow parameters which must be communicated properly between the computational regions. Further, the statistical nature of the solution technique complicates considerably the manner in which this additional information is communicated.

Complications due to the stochastic approach arise due to the treatment of particle scouring from the ground plane. The particles within the flow are represented by an ensemble of macro-particles which are randomly generated (swept-up) by the fluid motion behind the shock. This implies that a new particle may be introduced into the flow field at any point within the flow and at any time. Thus it is no longer possible to control the Region II simulation based only upon initial and boundary conditions from the Region I simulation.

To overcome these complications, a "snapshot" method has been developed. Periodically throughout the computation of the Region I solution snapshots are taken of the particle positions and attributes (velocity and size). This snapshot is then cropped so that only those particles contained within the Region II domain are considered. Upon taking the first snapshot all particles' attributes within the cropped region are saved. Subsequent snapshots save only those particles which have appeared in the cropped region since the previous snapshot. These data are then communicated to the Region II simulation at the appropriate times in the computation.

The new regional coupling scheme for two-phase flow calculations was tested. Tests indicate that it is possible to identically reproduce a regional calculation. For example, Figure 21 shows the predicted speed and particle locations behind a shock for an original (before implementing the new techniques and considering the entire domain to be Region I) simulation of a TRW 17 inch shocktube event (Ausherman, 1973). Figure 22 displays the same test problem, but in this case the computational domain is treated as a Region II simulation. That is, a Region I simulation was completed first in which snapshots were taken every ten cycles and saved. These snapshots were then utilized by the Region II simulation as outlined above. As can be seen from these figures, the results are nearly identical. To investigate the sensitivity to frequency of snapshots, the same procedure was repeated saving the snapshots every twenty-five cycles, rather than ten, Figure 23. Again little difference is noted, and while it appears that computational accuracy is insensitive to the frequency of snapshots saved, additional simulations should be undertaken to confirm the minimum number of snapshots required to maintain accuracy. Having implemented the proper interfacing procedures between Region I and Region II domains for dusty flows, it was then possible to proceed with the application of the sequential multi-grid methodology to evaluate loads in a two-phase flow.

4.2 DUSTY NON-IDEAL AIRBLAST LOAD SIMULATION: HST6-60.

NMERI CERF test shot HST6-60 was selected as the baseline case upon which to assess and demonstrate the accuracy of the **MAGIC** model predictions for vehicle loads predictions in a dusty non-ideal airblast environment. These data were selected due to the absence of "full scale" measurements which could be used as a basis for comparison and validation. The NMERI CERF experiments provided a reasonably well controlled and characterized non-ideal environment about realistic HML geometries at the overpressure range of interest and obtained pressure measurements of sufficient quality for an initial assessment of the numerical simulations.

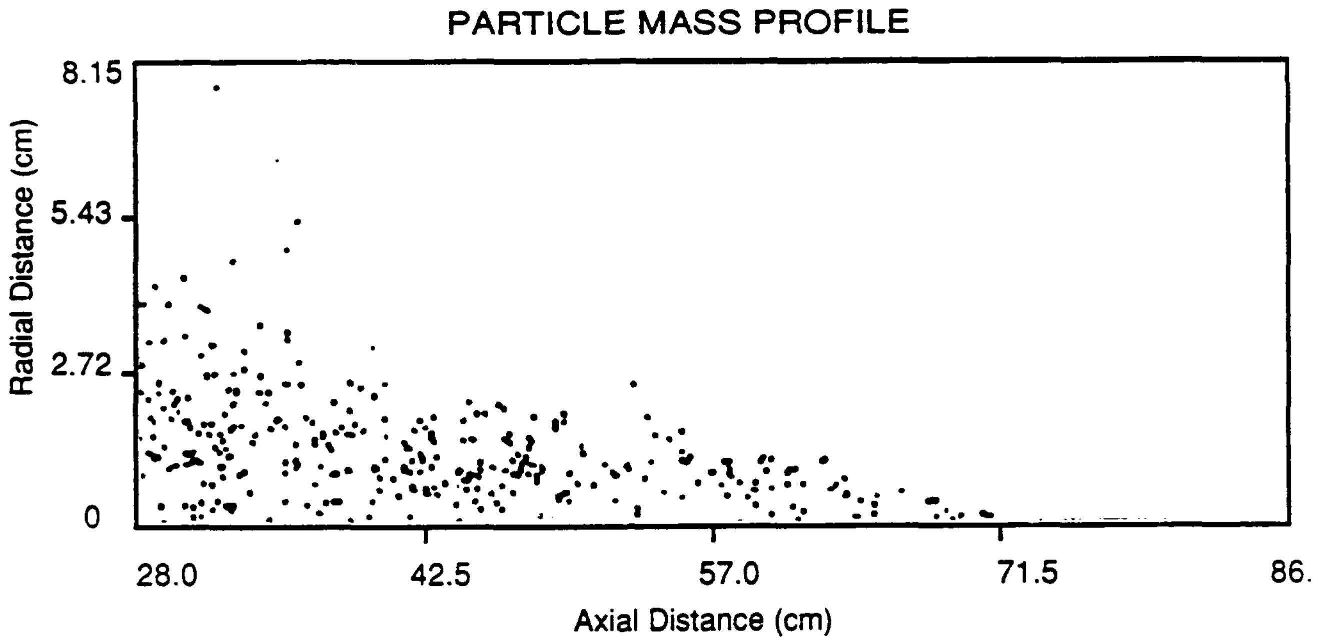

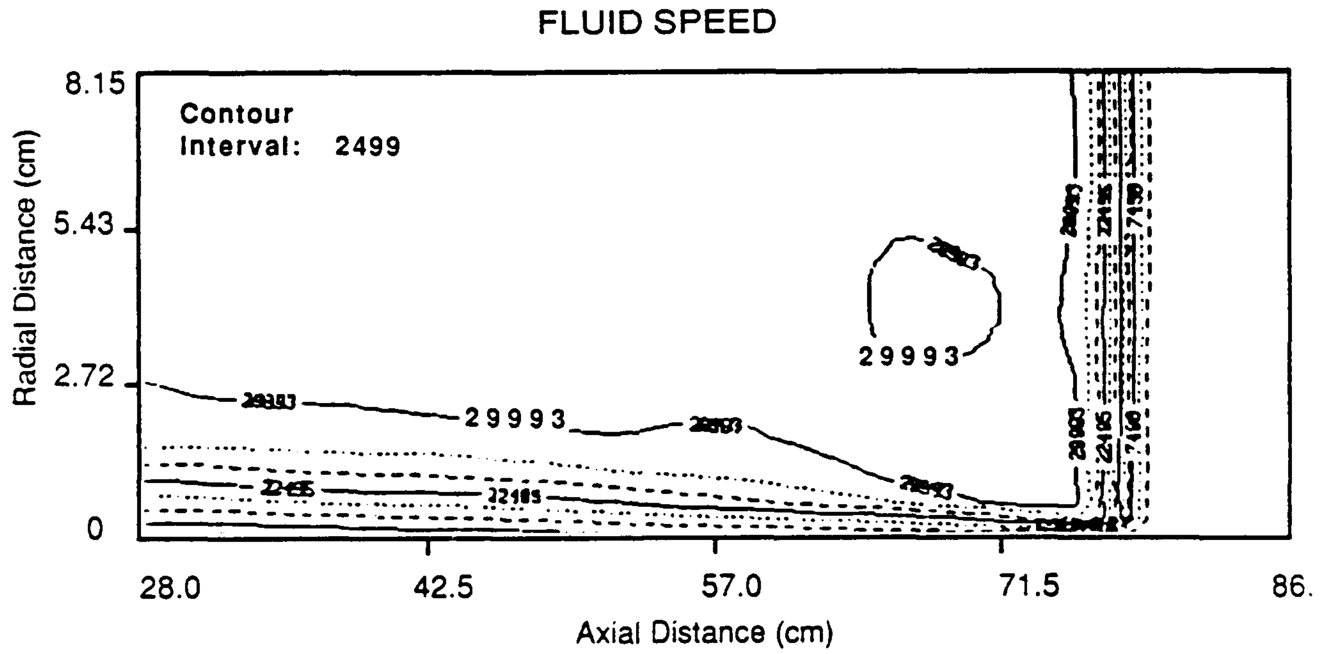

Figure 21. TRW 17" tube dusty flow simulation - Region 1.

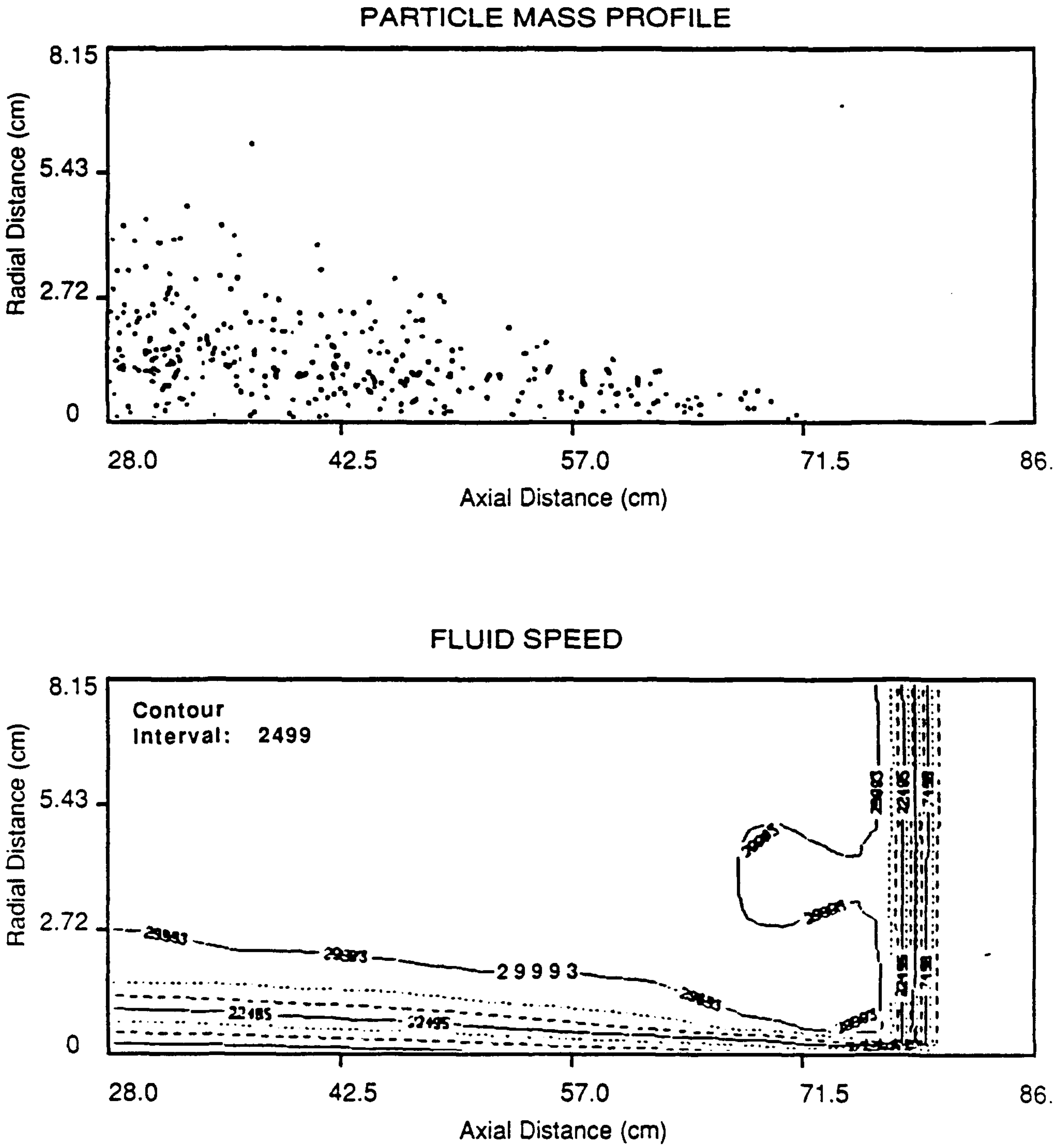

Figure 22. TRW 17" tube dusty flow simulation-
Region II - Data at every 10 cycles.

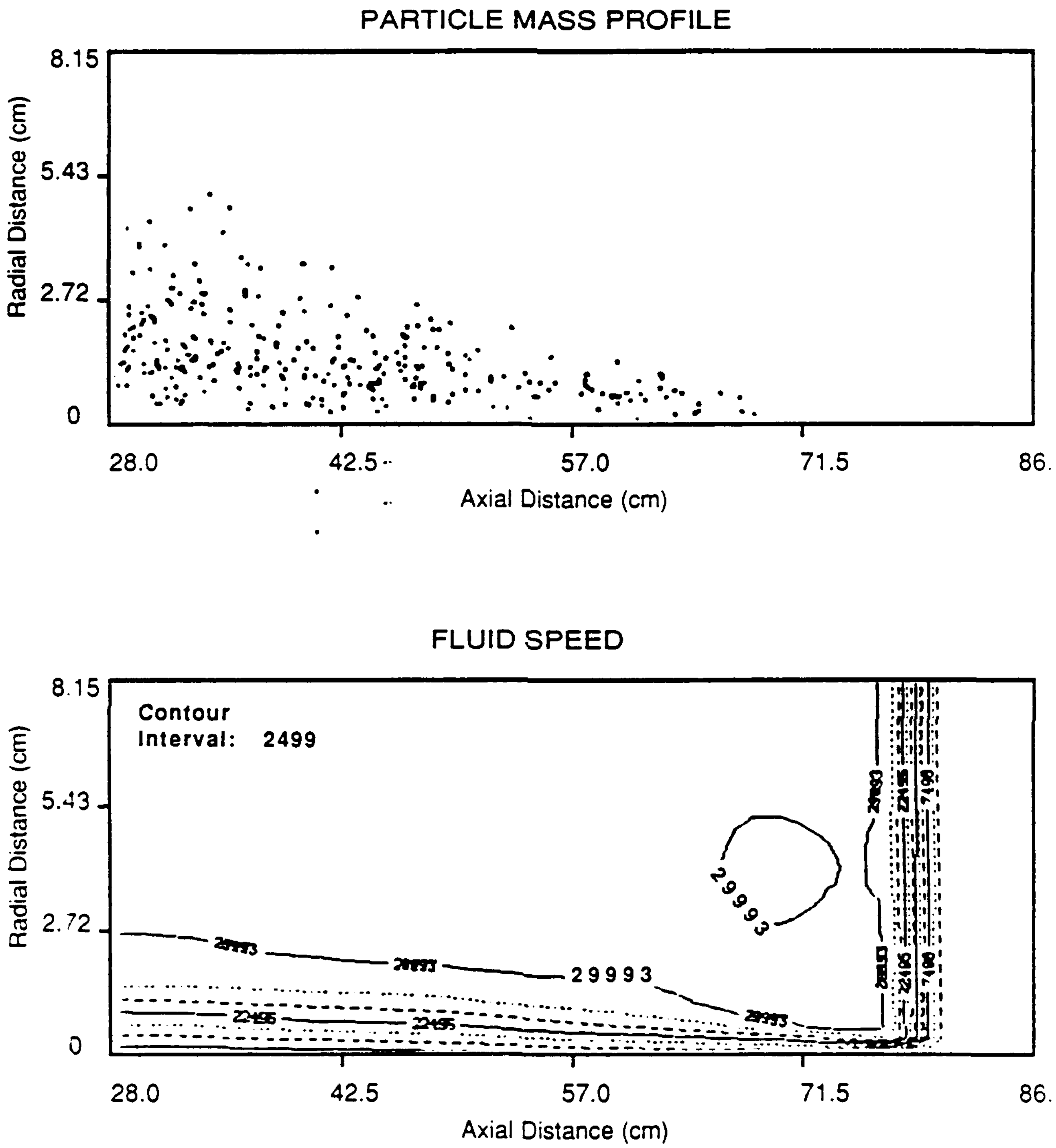

Figure 23. TRW 17" tube dusty flow simulation -
Region II - Data at every 25 cycles.

The simulation set-up for case HST6-60 is depicted in Figure 24. The triangular HML generic shape (figure 25) was located at station 122.75 from the breech end of the shocktube. A precursed flow was achieved with a 5 inch high layer of helium gas that extended from station 102.75 ft to 132.75 ft. Thus the helium layer extended 20 ft in front of the model, or nearly 50 model heights. The average helium concentration in terms of mole fraction for HST6-60 was 94 percent, and a 0.25 mil thick mylar membrane restricted the helium.

The "standard" driver was used for this test. It consisted of the reverse ignition of 19 strands of 400 gr/ft PETN det cord (15.2 lbs) located between stations 2.25 and 16.25 ft. This driver yields an overpressure of approximately 50 psi at the model station. This is the same environment simulation that was achieved in test shots HST6-38 and HST6-39, which have also been modeled using the **MAGIC** code (Traci, 1987).

The numerical simulation of this test was performed in a manner similar to the calculation method for HST6-38 and HST6-39. Time dependent two-dimensional Navier-Stokes calculations using **MAGIC** were performed for a portion of the shocktube. The upstream boundary of the Region I environments domain was located at a station (upstream of the helium layer) at which overpressure measurements were available. For test HST6-60, the upstream boundary was located at the 61.4 foot station, and the pressure measurements were used to derive the time dependent boundary conditions at the left-hand side of the Region I domain. The outflow boundary was located 2.5 ft downstream of the model, and supersonic outflow boundary conditions were imposed. In the vertical direction, the solution domain extended from the tunnel flow (located at $z = -1.573$ ft from the centerline) to the top of the shocktube ($z = 3$ ft). No slip boundary conditions were imposed along the solid surfaces, and surface roughness equal to 2 mm was used along the tunnel walls. On the HML model, a smooth wall condition was employed ($k = 0.01$ mm).

The dust pan started at the same axial location as the helium layer (102.75 ft) and extended to the model station. In the numerical simulation,

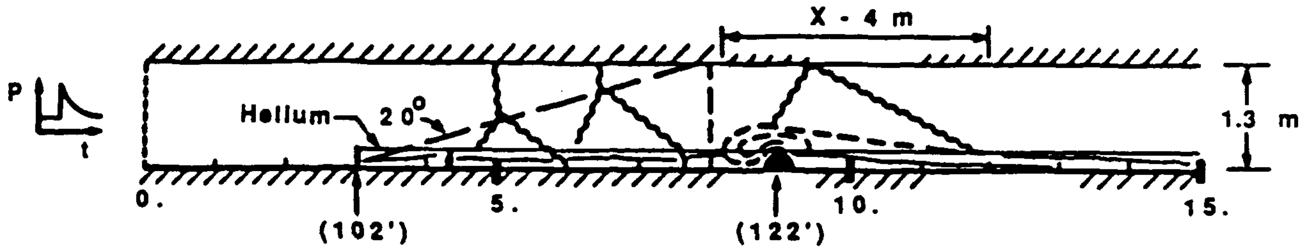

Date: 1-25-35

Time: 14:00

Ambient temperature: 44.0 °F

Ambient pressure: 12.2 psi

Relative humidity: 55 percent

Surface wind: 290°/5 kts

Local sound speed: 1100 ft/s

Driver: 19 strands of 400 gr/ft PETN det cord

location: 2.25 ft to 16.25 ft (range to upstream and downstream ends of driver with respect to coordinate system origin, x-axis)

total explosives weight: 15.2 lb

plane detonator

reverse ignition (toward open breech end of tube)

Shock tube configuration: open breech

Test environment: dust section

location: 102.75 ft to 122.75 ft (range to upstream and downstream ends of section with respect to coordinate system origin, x-axis)

material: sand, silt

top surface of dust section even with shock tube floor (z = -1.56 ft)

Thermal layers:

location*: 102.75 ft to 132.75 ft	location*: 167.57 ft to 179.30 ft
height: 5 in	height: 5 in
mylar thickness: 0.25 mil	mylar thickness: 0.25 mil
average helium concentration: 94.1 percent mole fraction	average helium concentration: 94.9 percent mole fraction

(* - range to upstream and downstream ends of thermal layer with respect to coordinate system origin, x-axis)

Model: triangular

location: 122.75 ft to upstream face of model with respect to coordinate system origin, x-axis

Figure 24. CERF test HST6-60 simulation arrangement.

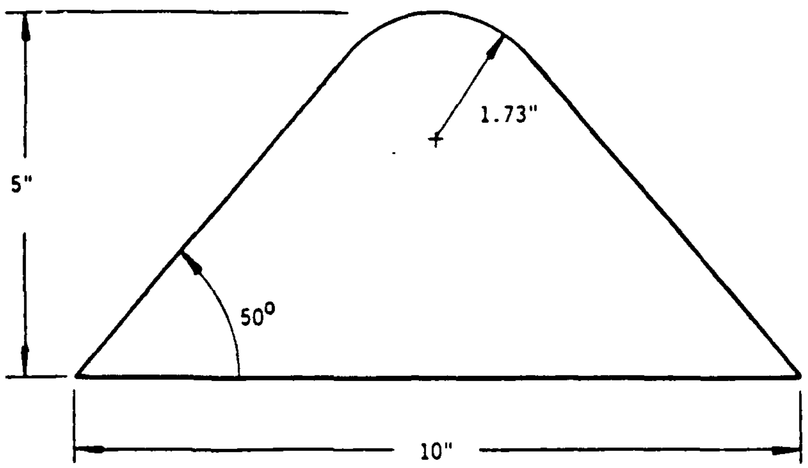

Figure 25. Generic HML geometry.

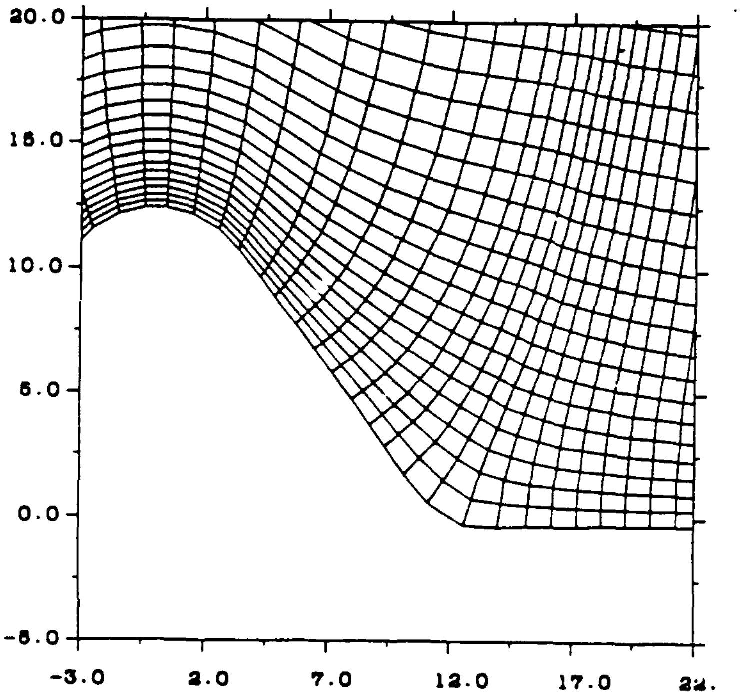

Figure 26. Conformal grid around generic HML model.

the same mixing controlled entrainment model and particle size distribution described in Section 2.2 (for the dusty Hst6-39 calculation) was used.

An important aspect of the methodology for performing numerical simulations of the flow over HML configurations is the strategy employed for grid generation. It is imperative that a nearly orthogonal, body-aligned grid network be constructed about the surface(s) of interest in order to accurately enforce the desired boundary conditions within the numerical scheme. Although typical HML geometries alone are not extremely complex, the flow must be computed with the HML shapes superimposed upon the ground surface. In order to address this issue, a method was developed to generate surface-aligned grid networks for typical HML geometries (superimposed upon a ground plane) using conformal transformations.

The basic approach is to construct a sequence of conformal mappings which transform the physical HML cross-section of interest to a nearly straight line in the transformed plane. A rectangular grid network constructed in the transformed plane will then correspond to a body-aligned grid in the physical space because the mapping is conformal. Figure 26 presents the actual grid in the vicinity of the generic HML model for test HST6-60. The coordinate lines are orthogonal, surface aligned, and "stretched" in a continuous manner, all of which contribute to an accurate numerical simulation.

Consistent with the sequential multi-grid methodology, the calculation was performed in two parts. The solution domain extended from station 61.4 ft to station 130 ft, and the first calculation simulated the dusty, non-ideal environment in this domain without a model in the flow. A Cartesian oriented grid system was employed, and the solution history was saved across the shocktube at station 120.5 ft. That is, for each computational cell, the time history of each of the calculated flow quantities (velocity component, thermodynamic state variables, turbulence quantities, etc.) were saved from the Region I solution. These properties were then used as boundary conditions to drive the Region II calculation, where the axial domain extended from 102.5 ft to 125.5 ft, and a conformal grid was constructed around the HML model located at 122.75 ft. In addition, the snapshot method described earlier was used to interface the particle positions and attributes (velocity and size) between the Region I and Region II calculations.

Figure 27 presents comparisons of the **MAGIC** code predicted surface pressure histories on the generic HML model with the experimental data for test shot HST-60. Predictions are shown for both clean and dusty flow simulations of the non-ideal (helium layer) HST6-60 environment. On the forward face of the model, the pressure histories correspond to the classic waveform in a non-ideal environment: namely, the initial low level rise in pressure due to the precursed flow, followed by a brief expansion, and then the wall jet arrival and decay.

The agreement between the calculations and measurements is generally quite favorable. On the forward face of the model, the peak surface pressures are predicted quite well, particularly for gauges 200 to 203, where the difference in the peak pressures are 5% and 20%, respectively. However, it is difficult ascribe a meaningful percentage variation due to the exhibited unsteady or fluctuating character in the measured pressure when the wall jet arrives at the model. It is clear however, that the width of the predicted pressure pulse agrees well with the measured width. It is also clear that the measured high frequency oscillations in pressure would not contribute significantly to the overall impulse imparted to the model. This conclusion is relfected to a degree in the model lift and drag comparisons shown in Figures 28 and 29, which are discussed below.

Near the top of the model, a strong flow expansion process occurs. The forward facing gauges in this vicinity (204 to 26) register higher peak pressure levels than the numerical simulation, which simply indicates that the flow expansion initiates slightly sooner in the calculation. The circumferential gradients are quite large in this region, and modest differences in the overall flow features can be magnified by comparing histories at specific locations within this domain. On the leeside of the model, the calculated and measured pressure levels are both quite small and have a minimal effect on the total loads.

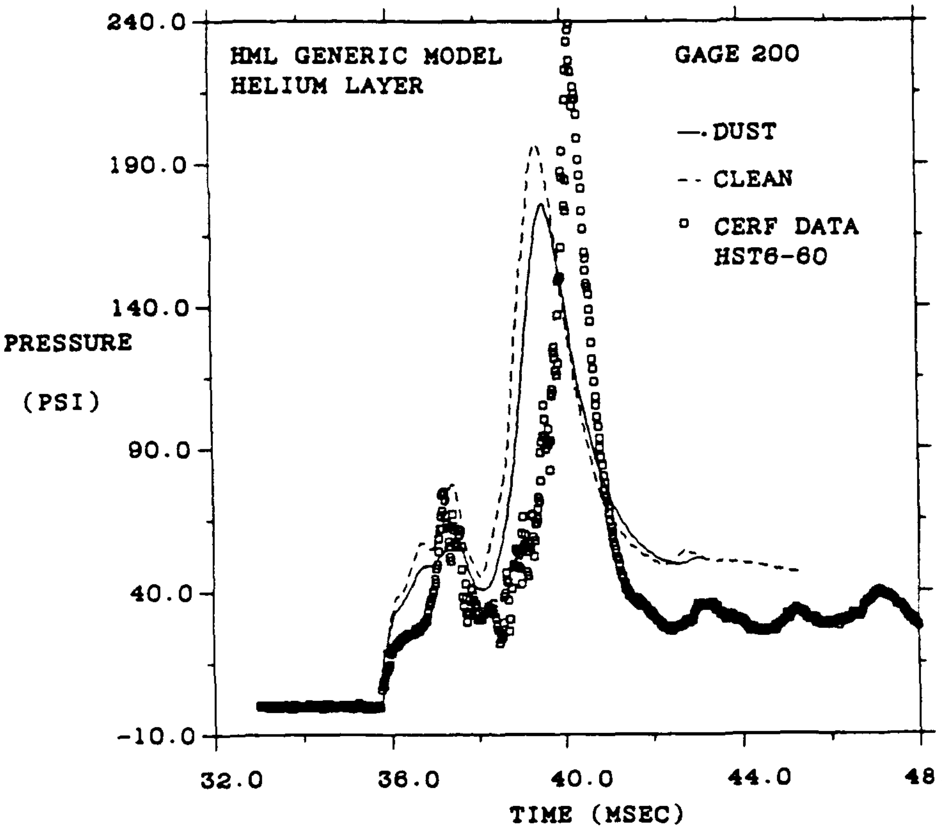

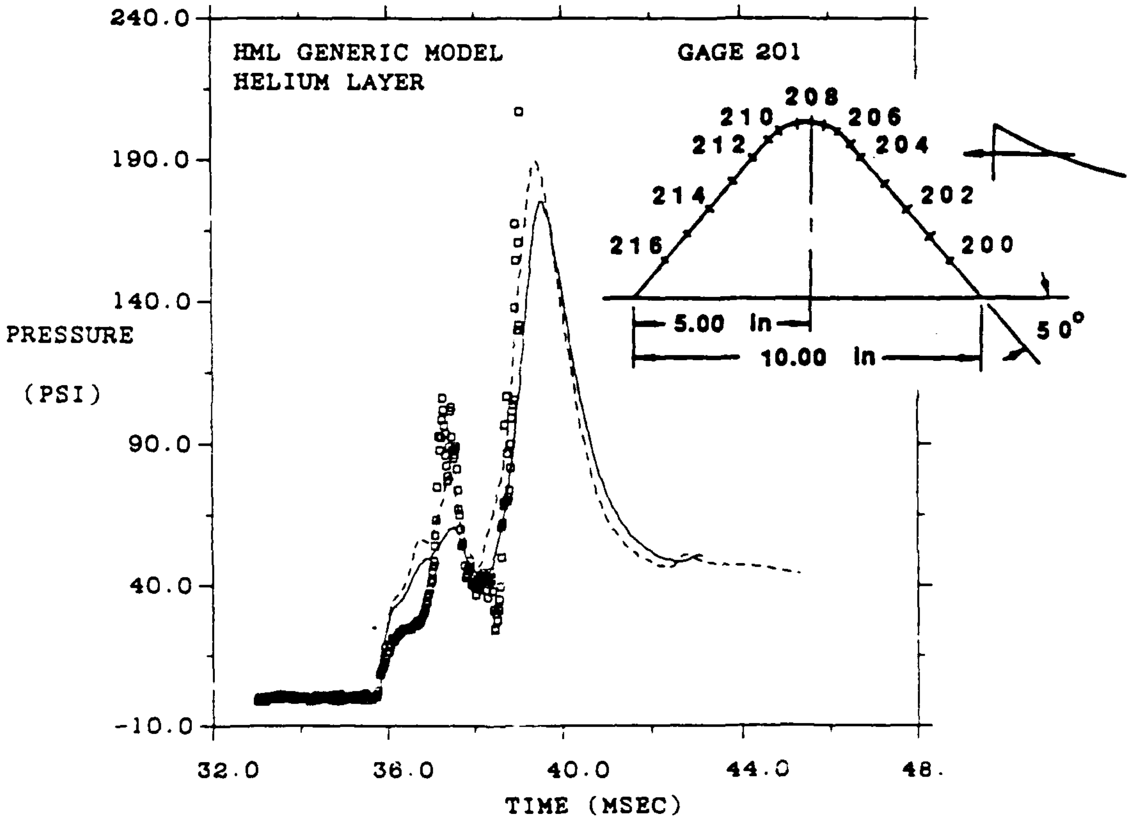

Figure 27. Comparison of MAGIC prediction and surface pressure measurements for HST6-60 (Continued).

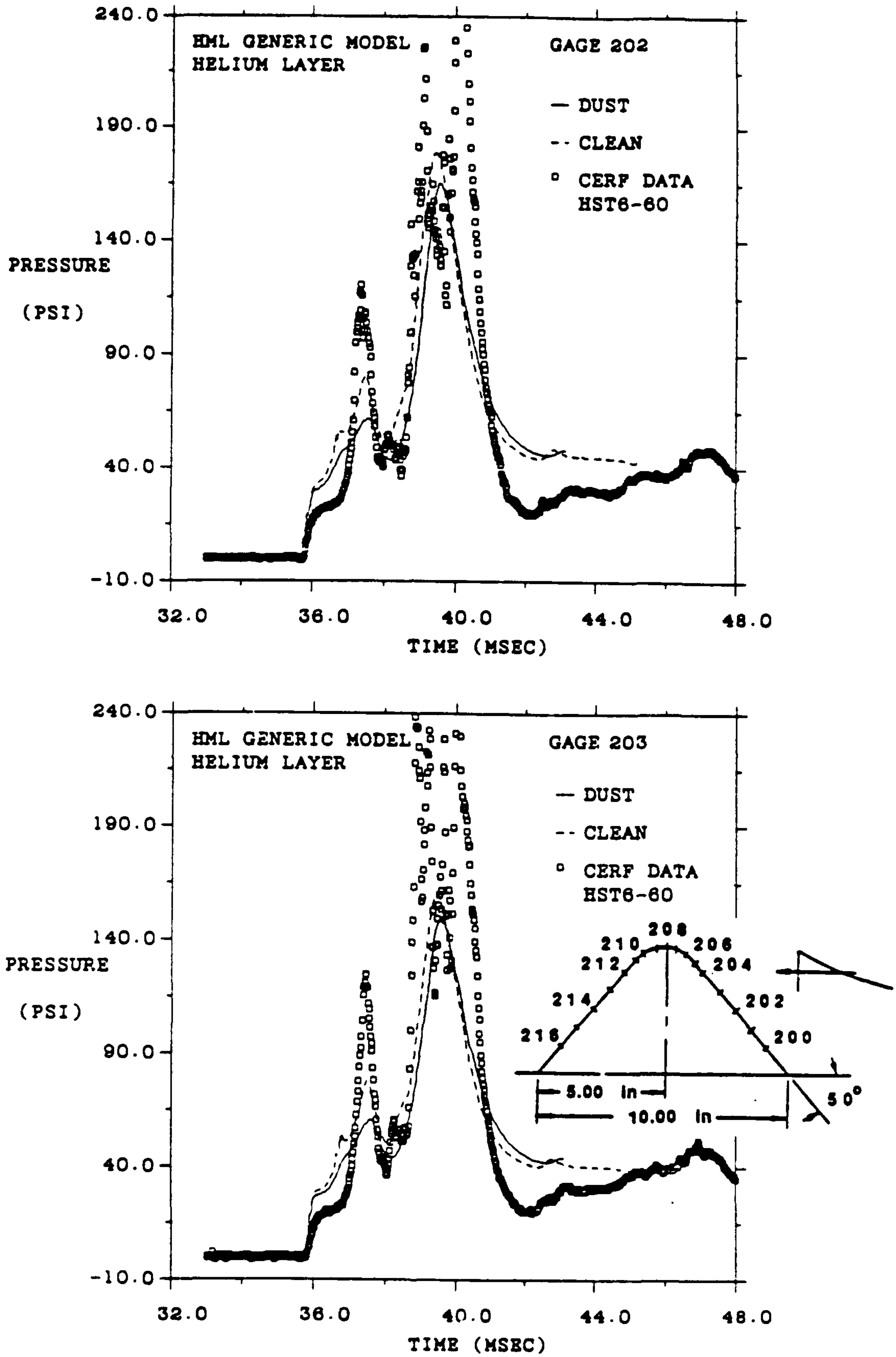

Figure 27. Comparison of MAGIC prediction and surface pressure measurements for HST6-60 (Continued).

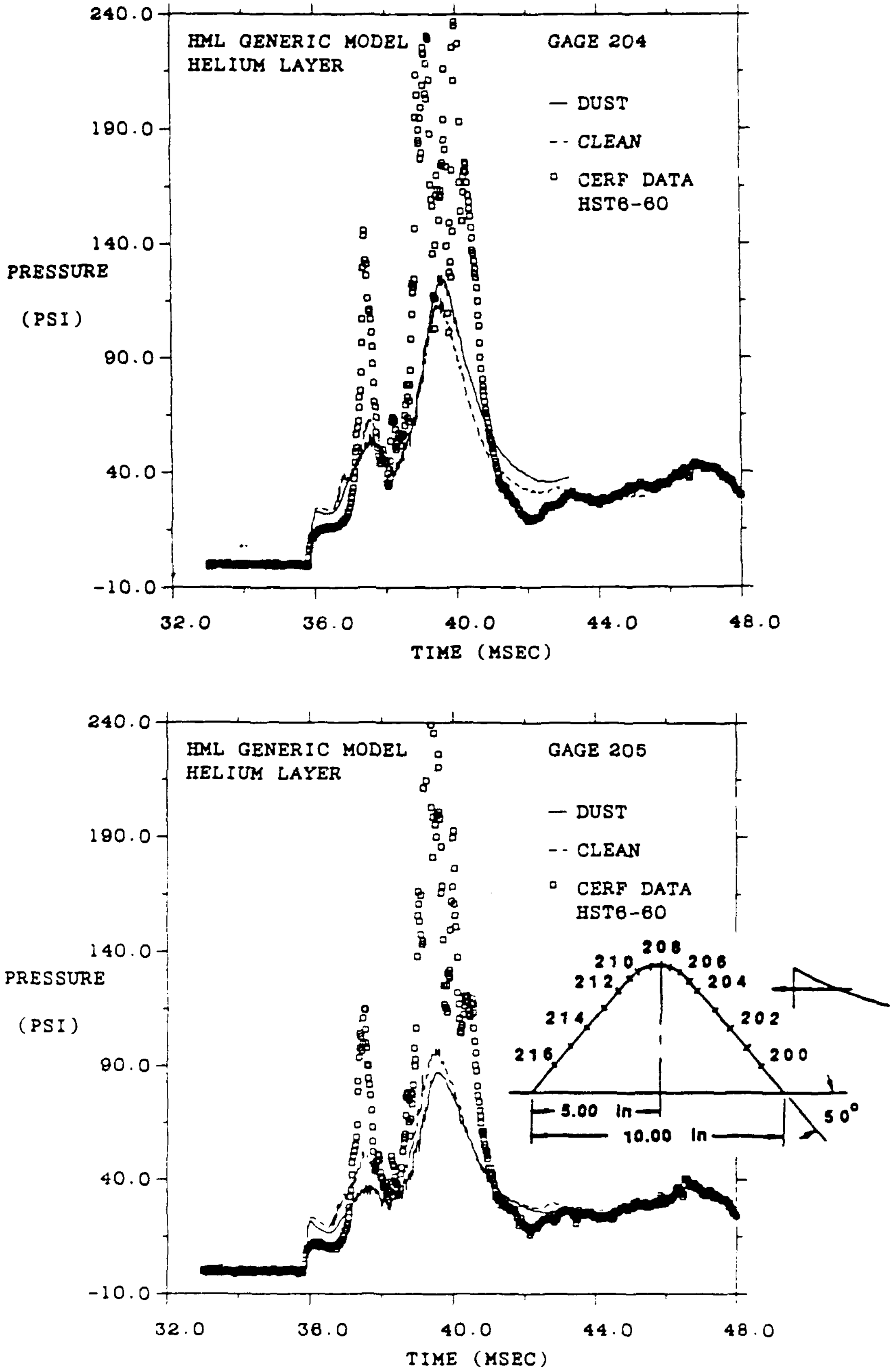

Figure 27. Comparison of MAGIC prediction and surface pressure measurements for HST6-60 (Continued).

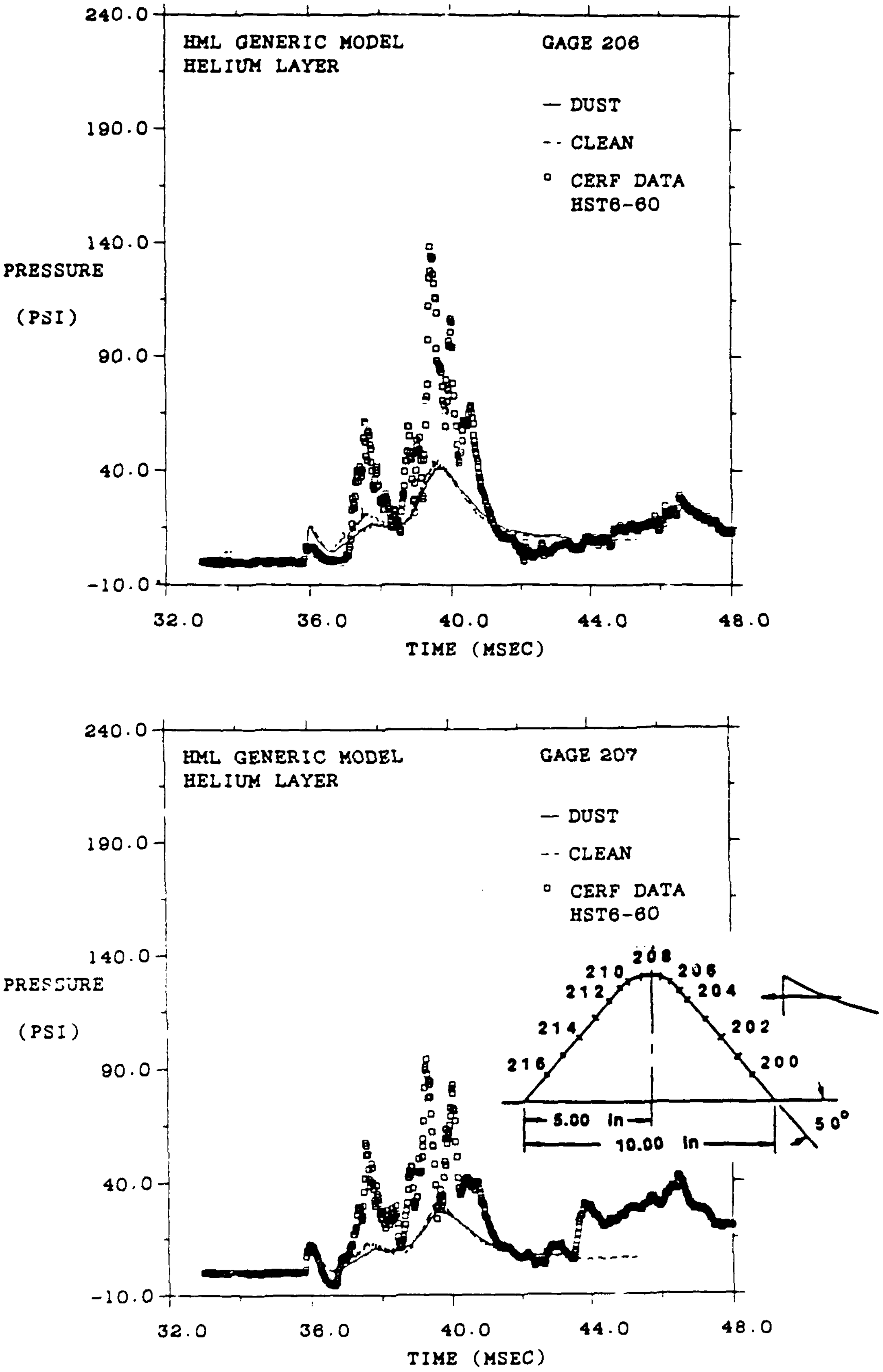

Figure 27. Comparison of MAGIC prediction and surface pressure measurements for HST6-60 (Continued).

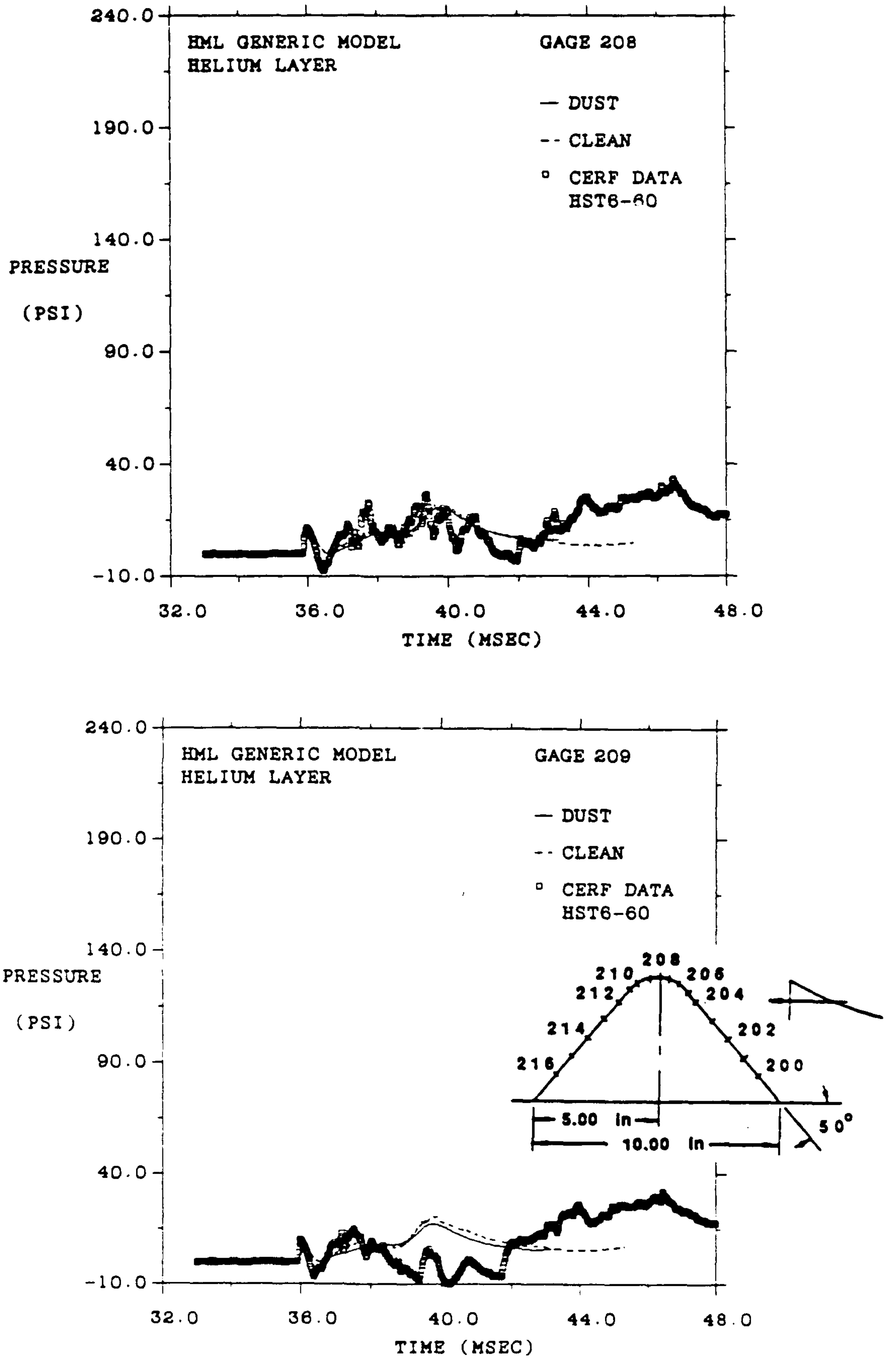

Figure 27. Comparison of MAGIC prediction and surface pressure measurements for HST6-60 (Continued).

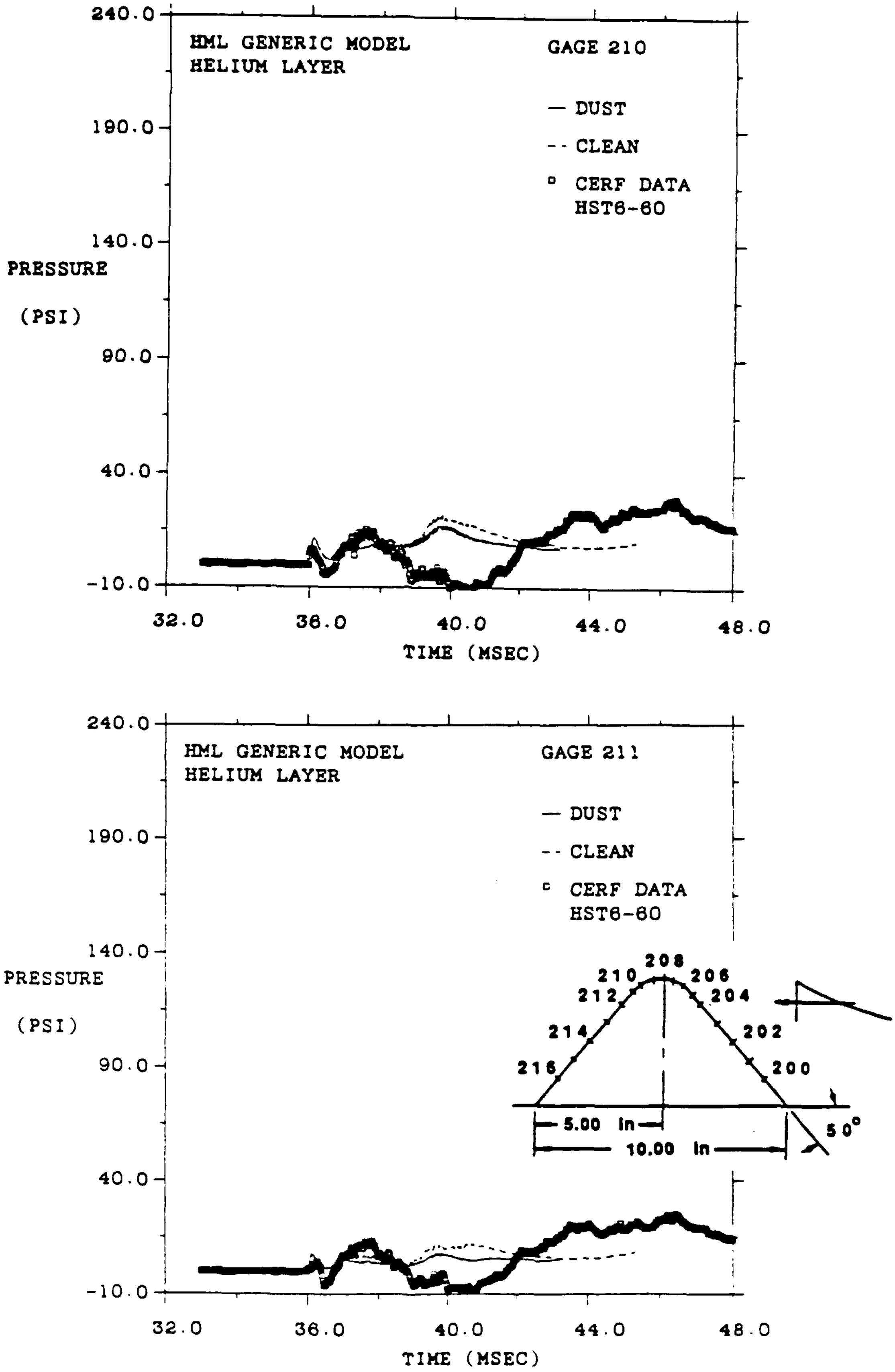

Figure 27. Comparison of MAGIC prediction and surface pressure measurements for HST6-60 (Continued).

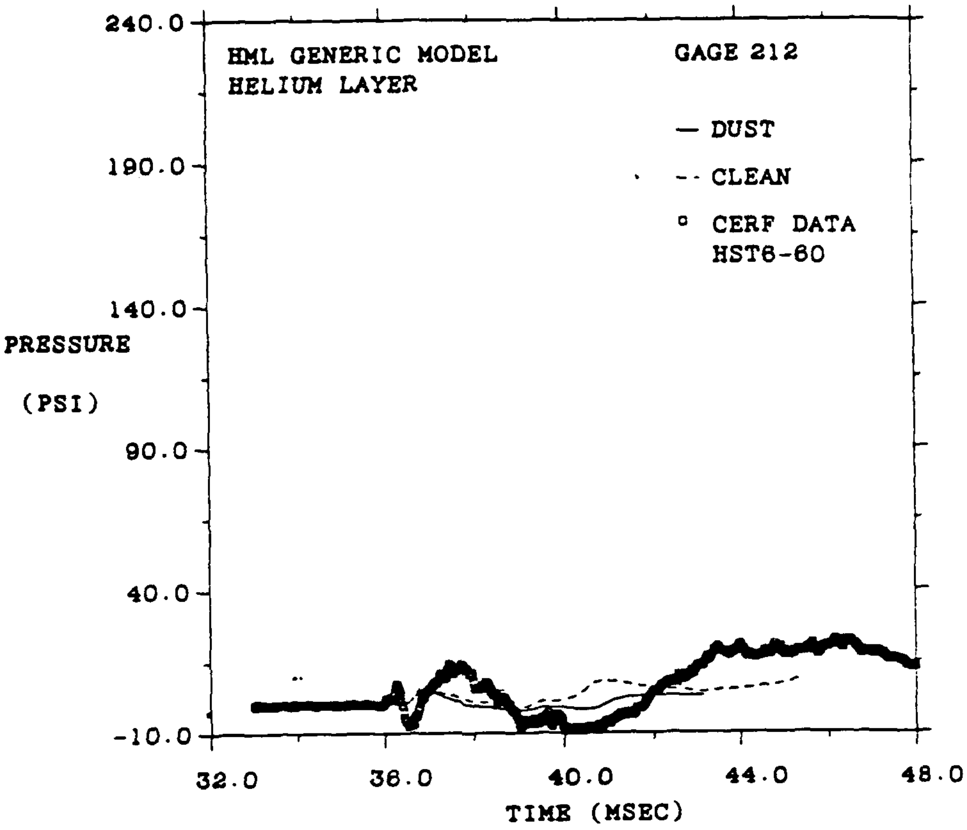

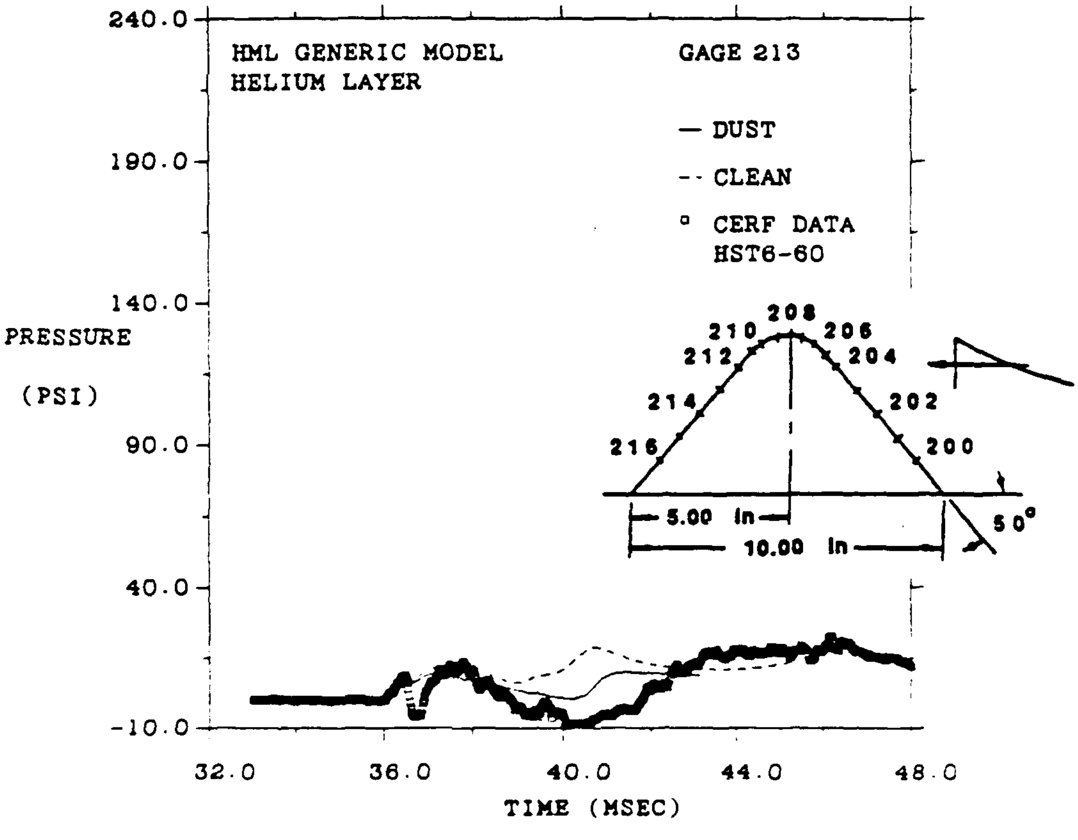

Figure 27. Comparison of MAGIC prediction and surface pressure measurements for HST6-60 (Continued).

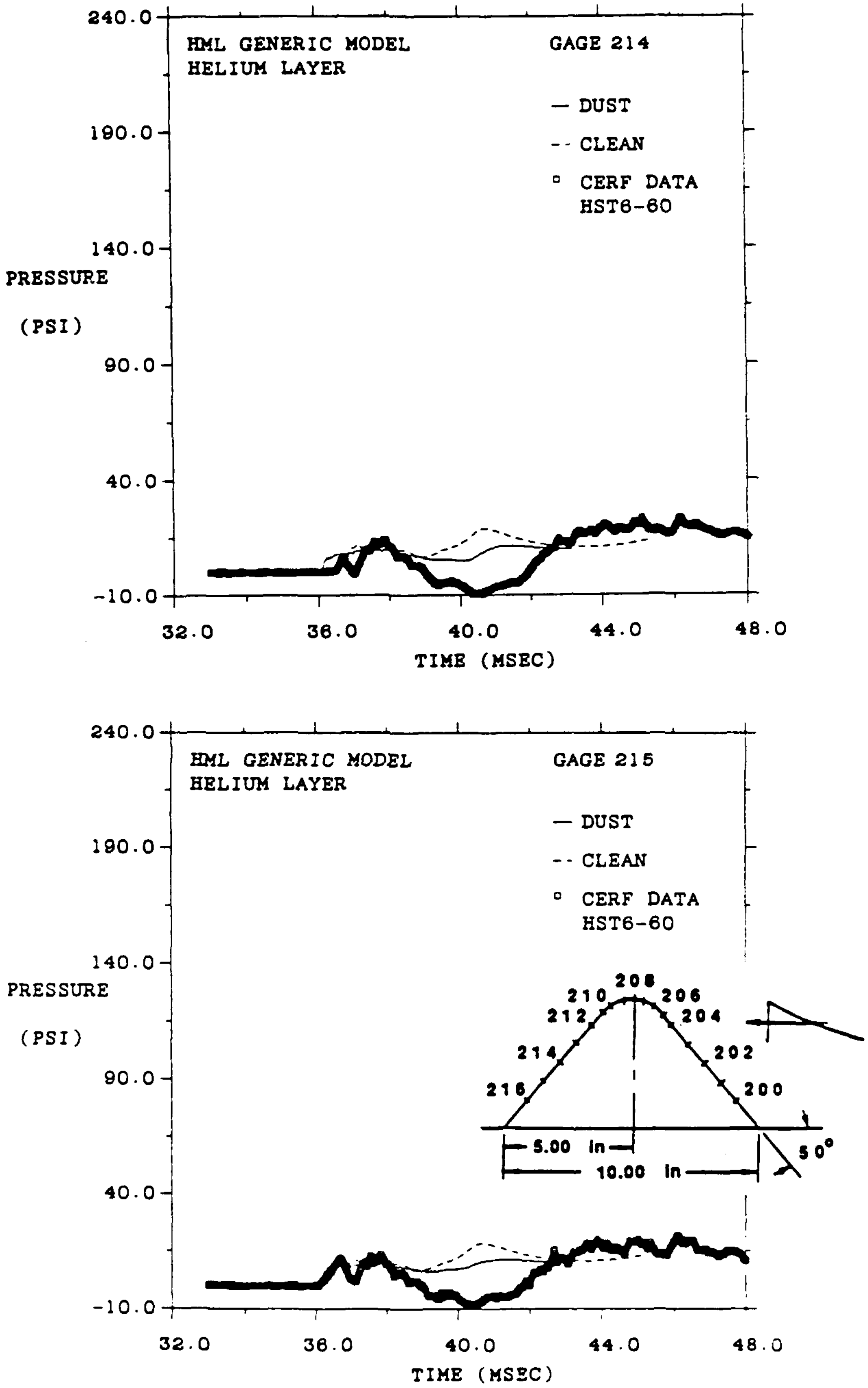

Figure 27. Comparison of MAGIC prediction and surface pressure measurements for HST6-60 (Concluded).

In order to isolate the effect of dust on the vehicle loads, **MAGIC** calculations were performed for the HST6-60 non-ideal environment for both clean and dusty flows. The dashed lines in Figure 27 indicate the predicted pressure histories around the HML model corresponding to a clean environment. Comparison of the clean and dusty flow simulations indicates the anticipated two-phase flow effects. First, the maximum surface pressures experienced by the model in the dusty flow region are reduced. This is due to the attenuation of the wall jet intensity through the momentum transfer to the entrained dust particles. Also, the duration of the pressure well (between the instant of peak precursor strength and the arrival of the wall jet) is greater for the dusty flow case. This portion of the waveform can usually be associated with a brief transient period of flow separation on the upstream side of the model. Due to the loss of momentum in the inner portion of the dusty boundary layer approach flow, the period of upstream separation is extended with dust.

Figures 28 and 29 present a comparison of the predicted and "measured" force component histories experienced by the model for HST6-60. (In this case the measured forces were obtained by integrating the pressure measurements because a force balance was not used.) The overall agreement between the **MAGIC** results and the measured force components is fairly good. Of particular interest are the maximum lift and drag loads, which are predicted quite accurately. However, there is a difference in the predicted and observed duration of the loads imparted by the wall jet flow. There is also a difference between the calculated and deduced late time loadings during the quasi-steady drag phase after the wall jet has passed the model. This apparent discrepancy warrants further attention because 1) the trends do not seem to be substantiated by the pressure history comparisons, and 2) it has been previously demonstrated that the **MAGIC** code is capable of modeling load distributions during the quasi-steady flow phase (see Figure 20 and Traci, 1987). This ability should not be compromised due to the presence of dust particles in the flow.

Finally, the issue of modeling dust particle interactions with the model surface warrant discussion. Because the **MAGIC** code employs a discrete model for an ensemble of macro-particles, several possible approaches can be

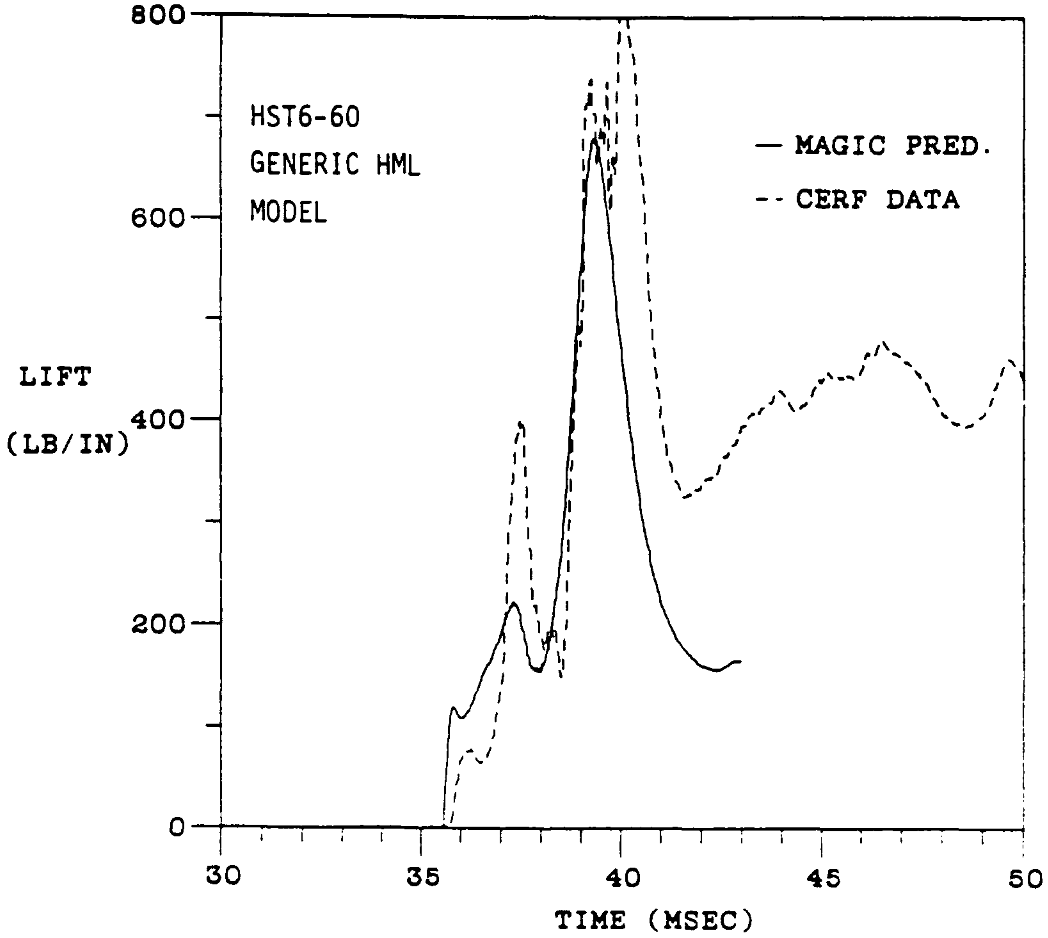

Figure 28. Comparison of MAGIC prediction and measured lift force history for HST6-60.

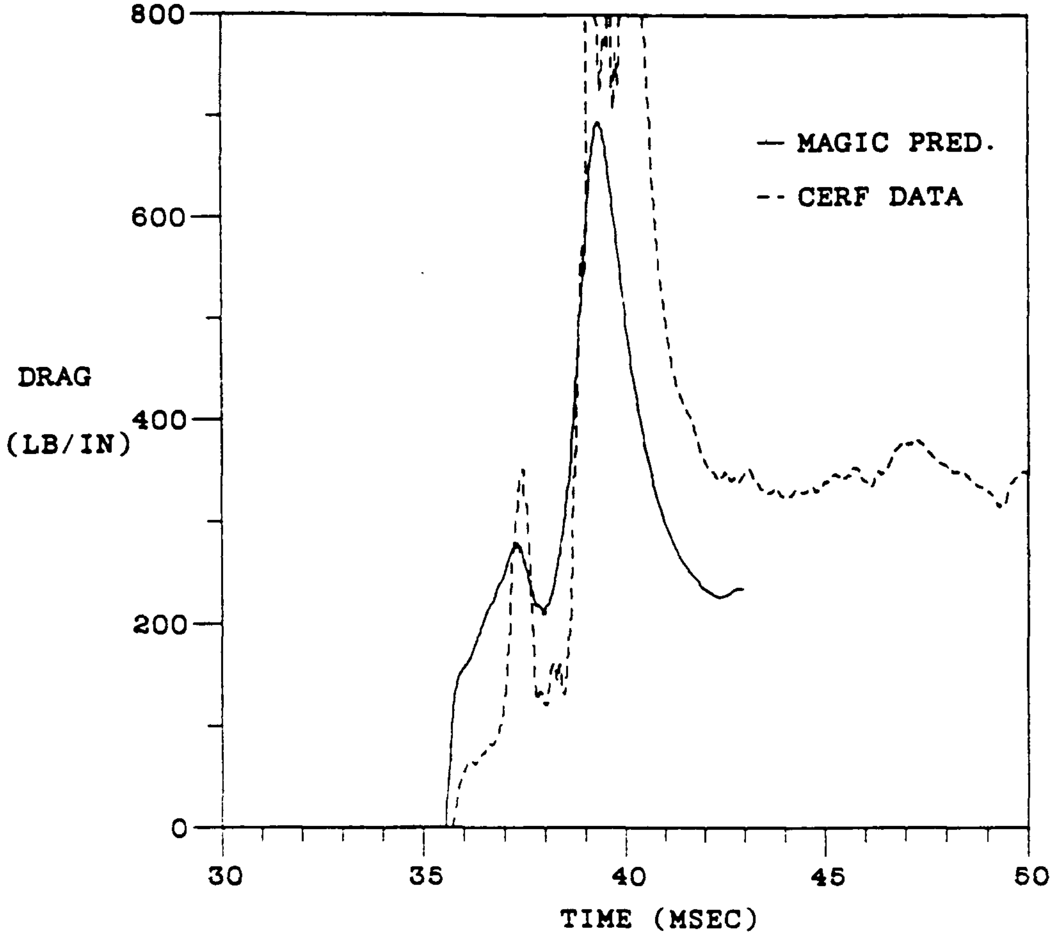

Figure 29. Comparison of MAGIC prediction and measured drag force history for HST6-60.

adopted to model the subsequent physics of individual particles after they impact the model. The principal options consist of particles which adhere (particle stick) to the surface, and either elastic or inelastic rebound models. In this simulation of HST6-60, the former model was used: impacting dust particles were simply allowed to stick to the model. The current discrete particle modeling approach is not restricted to particle adhesion on a surface (as is the case for continuum two-phase flow modeling treatments), and further tests involving alternative particle rebound methodologies is an area of future study. However, before applying alternate boundary treatments, a suitable model for particle rebound appropriate to the morphology of the particulates must be developed.

Although the overall dust density is substantial relative to the gaseous (air-helium) density, the particulate impact has a very small contribution to the total loads experienced by the model for this test. Therefore, it would be expected that vehicle loads would be substantially unchanged if momentum transfer was doubled, as would be the case with an elastic rebound model. There is a caveat to this, however. Because **MAGIC** utilizes a discrete, not a continuum, particulate model it is possible, as was mentioned above, to model the interaction effects between the particles which deflect from the model surface and the approach flow. This has not been done to date for HST6-60. However, unlike a continuum model, the current discrete approach is not limited by the presence of particle "crossing trajectories". These effects are easily treated, provided a reasonable model for the particle-boundary interaction is formulated.

The nature of the non-ideal flow structure about the cylindrical model is depicted in Figure 30 to 41. Velocity vector and contour plots are presented at three different times, each corresponding to an instant during a particular period of interest during the waveform development. The three snapshots are at 37.2, 39.3 and 43 msecs, which correspond to characteristic precursor, wall jet, and quasi-steady flow times, respectively.

Velocity vector plots in the vicinity of the model which illustrate the development of the flow around the body with time are presented in Figures

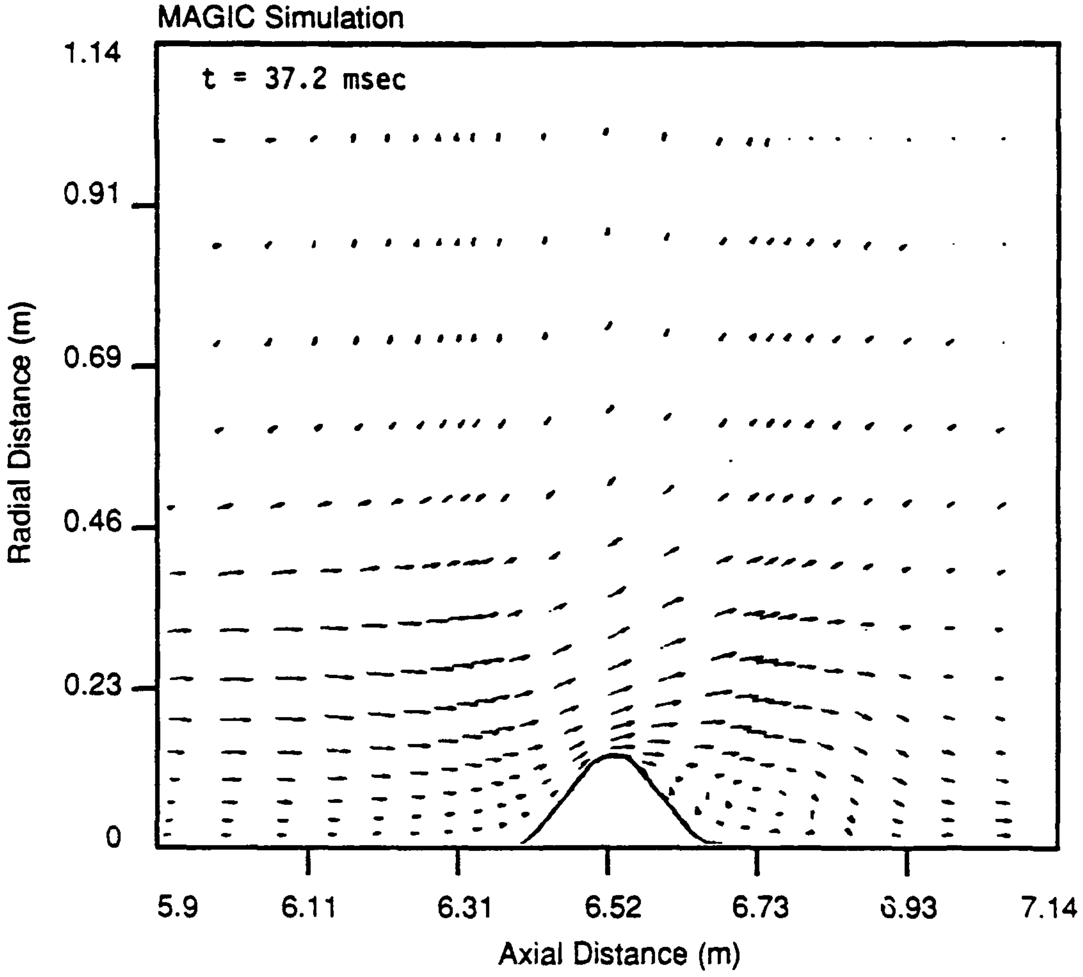

Figure 30. Velocity vector distribution during precursor flow for HST6-60.

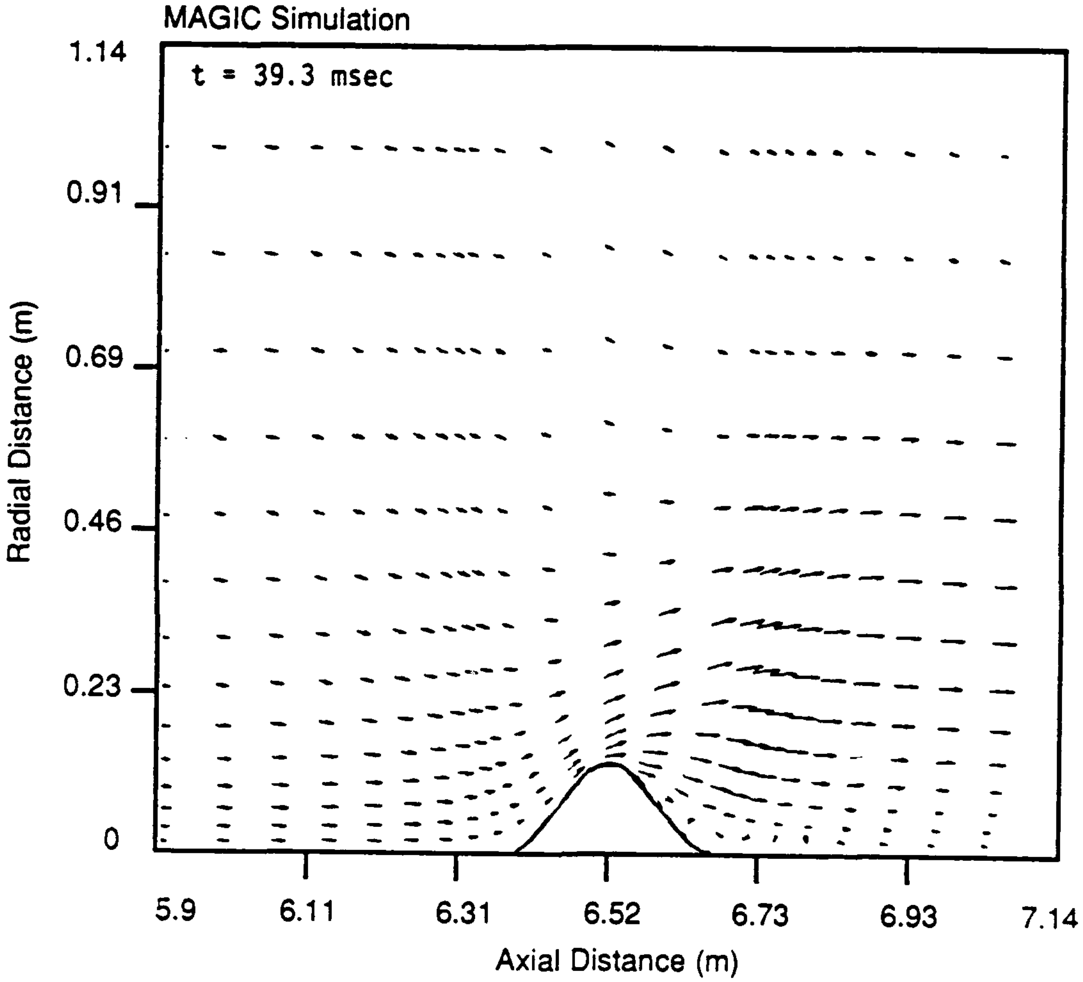

Figure 31. Velocity vector distribution near maximum vehicle loading for HST6-60.

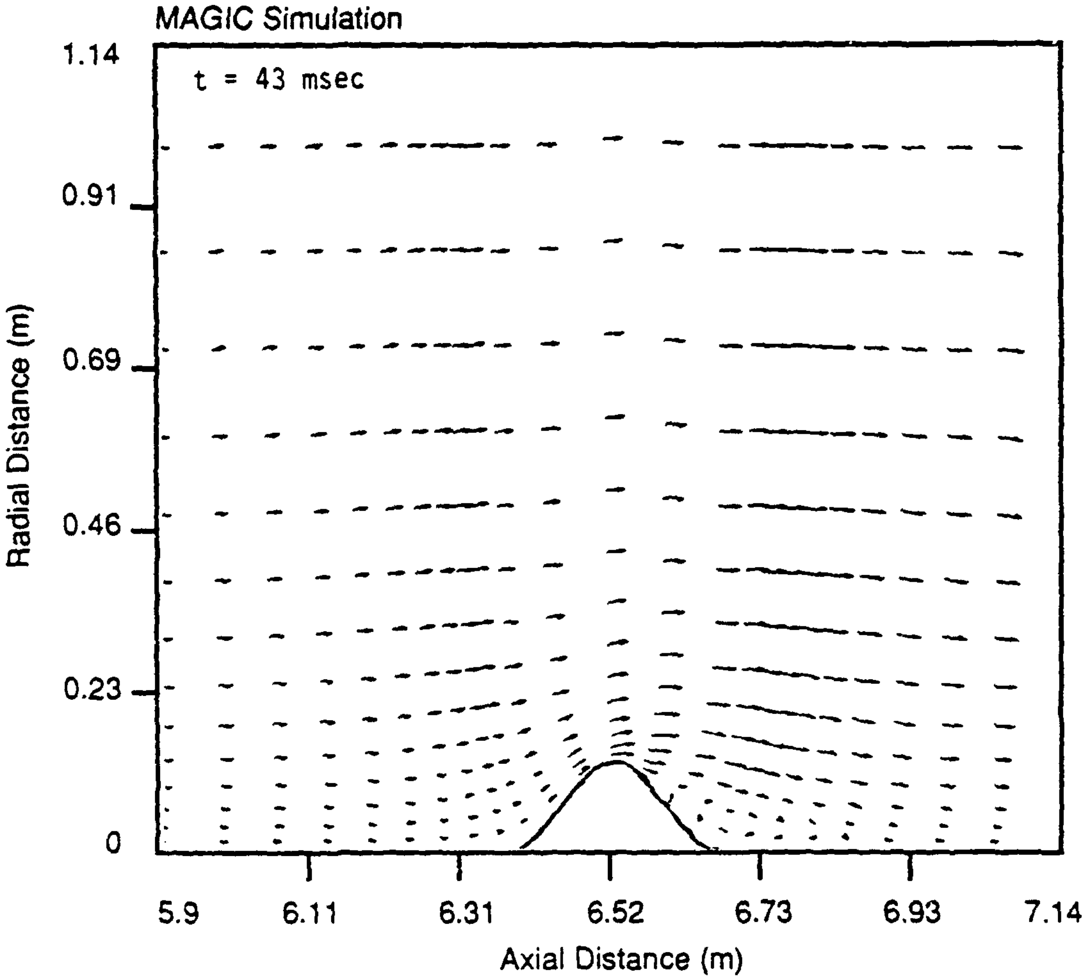

Figure 32. Velocity vector distribution during quasi-steady flow phase for HST6-60.

30 through 32. (For the purpose of clarity, velocity vectors are depicted at every other radial and axial computational cell in the flow domain.) The solution indicates that the flow is separated on the downstream side of the model at all three snapshots in time. In addition, the arrival of the precursor shock and flow, as well as the beginning of the wall jet flow can be discerned in Figure 30.

Figures 33 through 35 present contour plots of the fluid speed at the three times of interest. The flow is subsonic in the immediate vicinity of the model, and as such accelerates over the forward face, attains its maximum speed over the top, and decelerates over the back side. The figures also provide insight to the nature of the approach flow (in particular, the height and intensity of the wall jet), as well as the extent of the separated zones around the model.

Static pressure contours are illustrated in Figures 36 through 38. The flow compresses at the model base, then undergoes an increasingly rapid expansion as it approaches the top of the model. In Figure 37, the coalescence of pressure contours ahead of the model is indicative of a strong detached shock wave, as the approaching wall jet flow is supersonic. In contrast, the approach flow is subsonic at both the earlier (t = 37.2 msec) and later (t = 43 msec) snapshots.

Finally, Figures 39 through 41 present stagnation pressure contours at the three characteristic times of interest. These figures illustrate particularly well the nature of the approach flow and the interactions which occur around the model. In Figure 39, the precursor and main shocks are evident, as well as the arrival of the highly energetic wall jet flow, which is centered about 2 model heights above the tunnel floor. In Figure 40 (t = 39.3 msec), the main shockwave flow interacts with the model, which yields large stagnation pressure levels along the forward face and sends an oblique shockwave into the stream. Finally, the contours in Figure 41 (t = 43 msec) are indicative of a weaker and uniform flow, characteristic of the quasi-steady flow associated with the decaying blastwave.

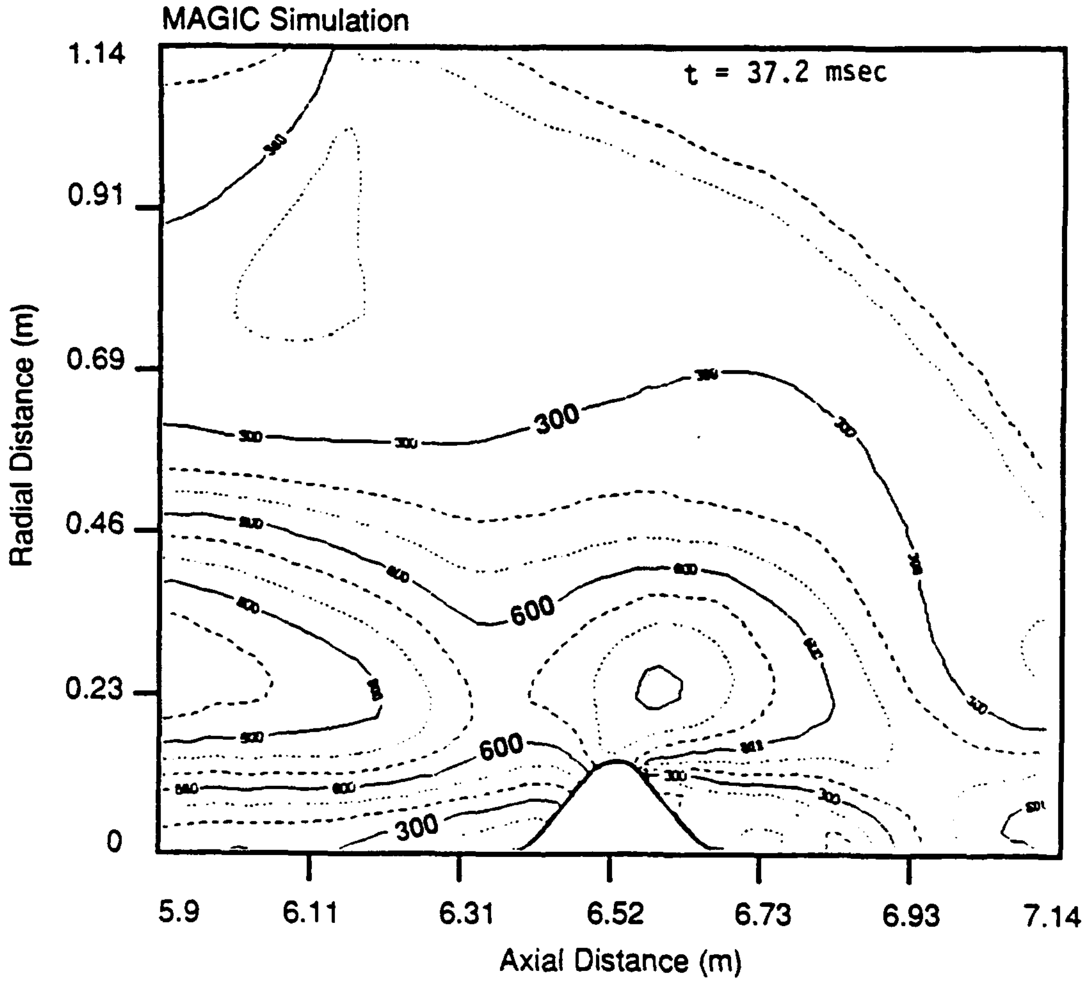

Figure 33. Flow speed contours (m/sec) during precursor flow for HST6-60.

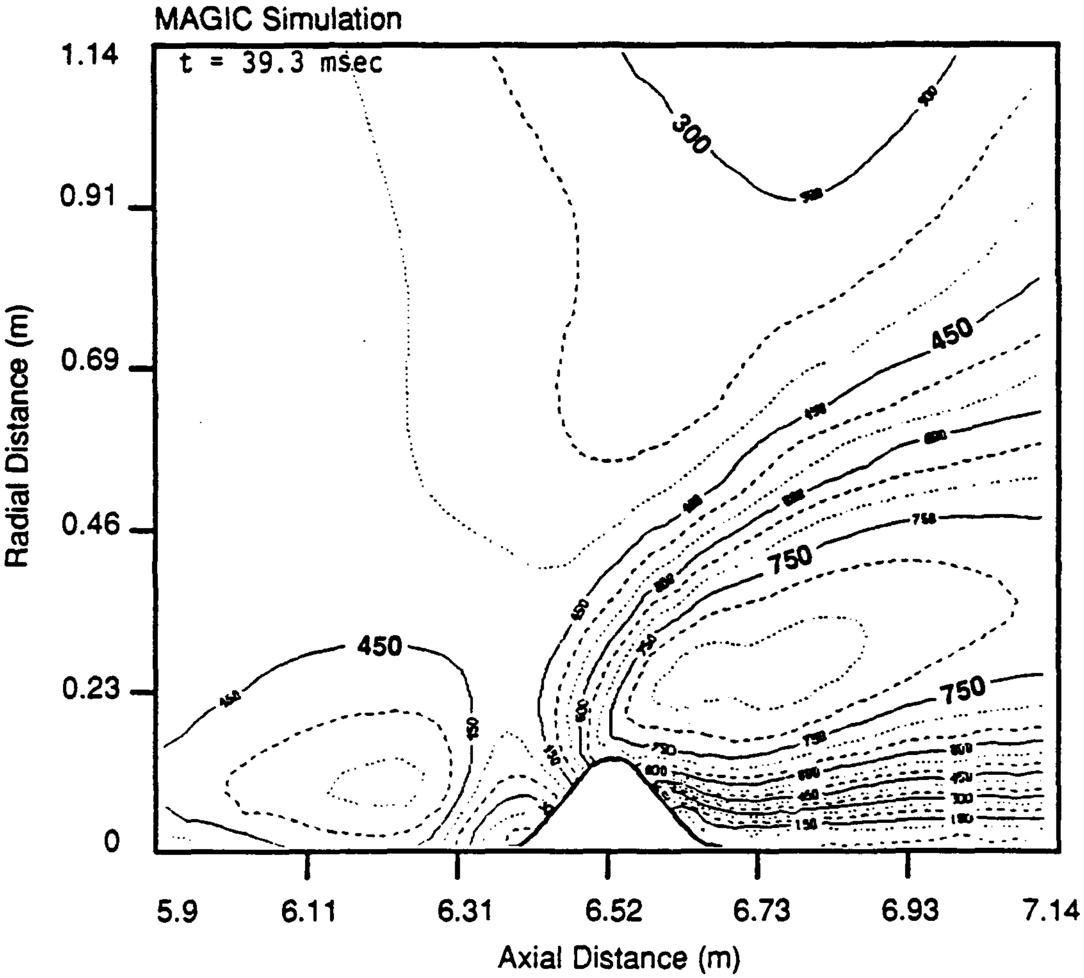

Figure 34. Flow speed contours (m/sec) during maximum vehicle loading for HST6-60.

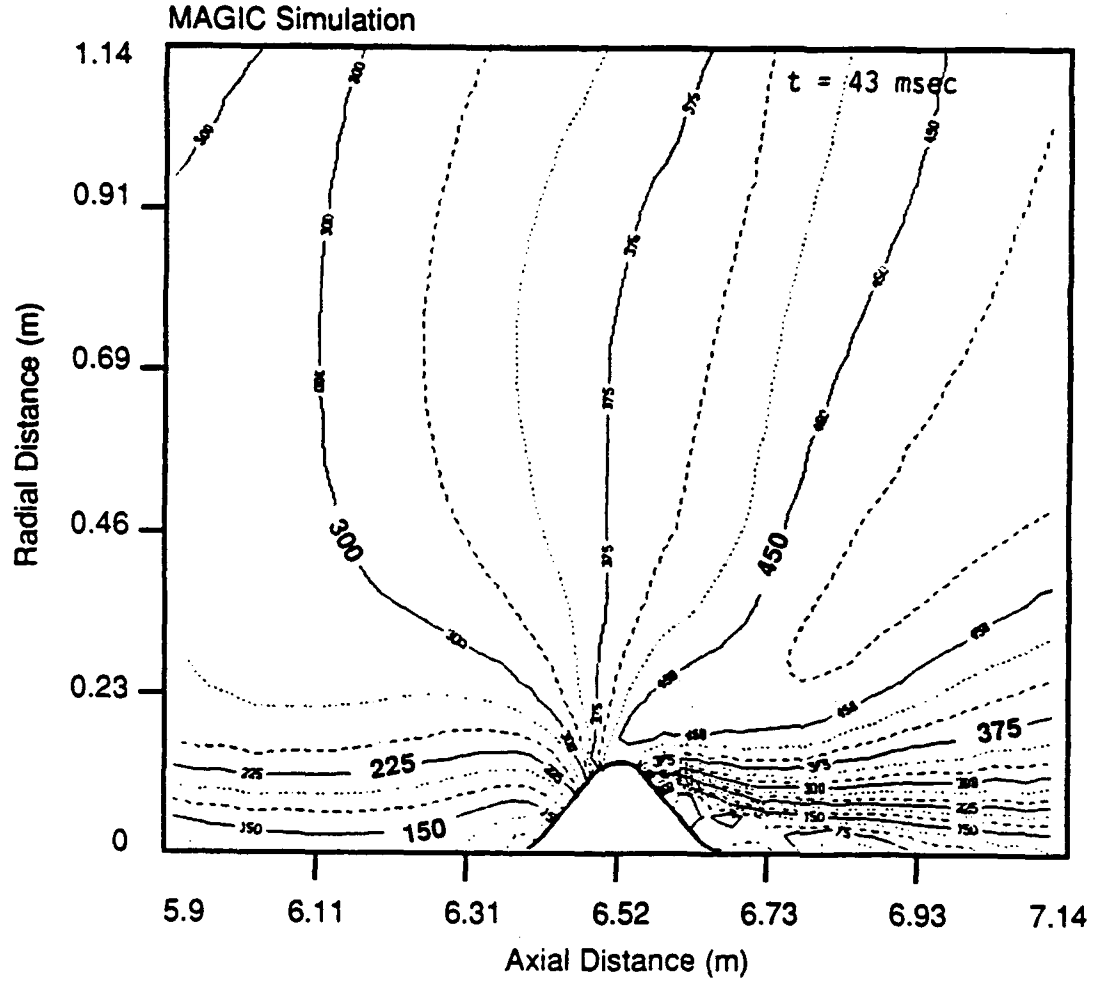

Figure 35. Flow speed contours (m/sec) during quasi-steady flow phase for HST6-60.

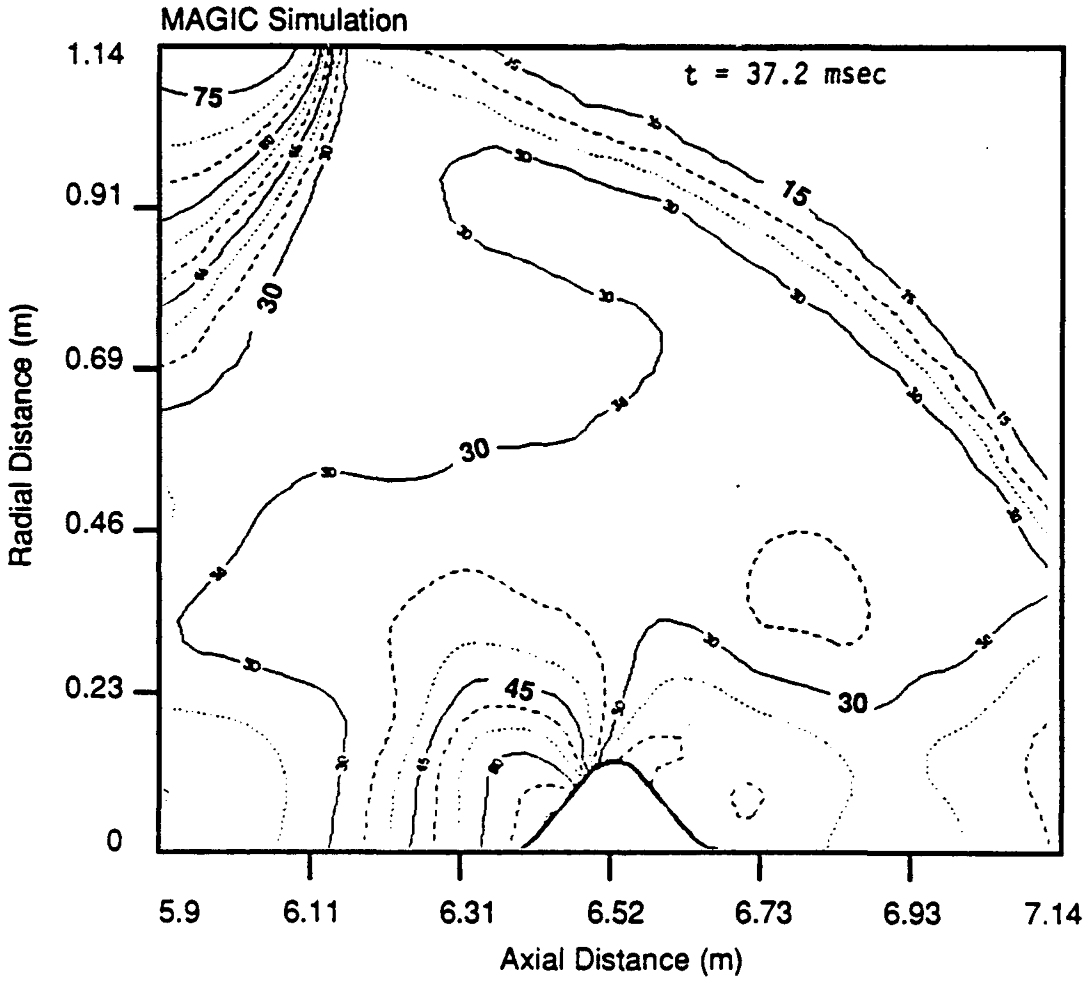

Figure 36. Static overpressure contours (psi) during precursor flow for HST6-60.

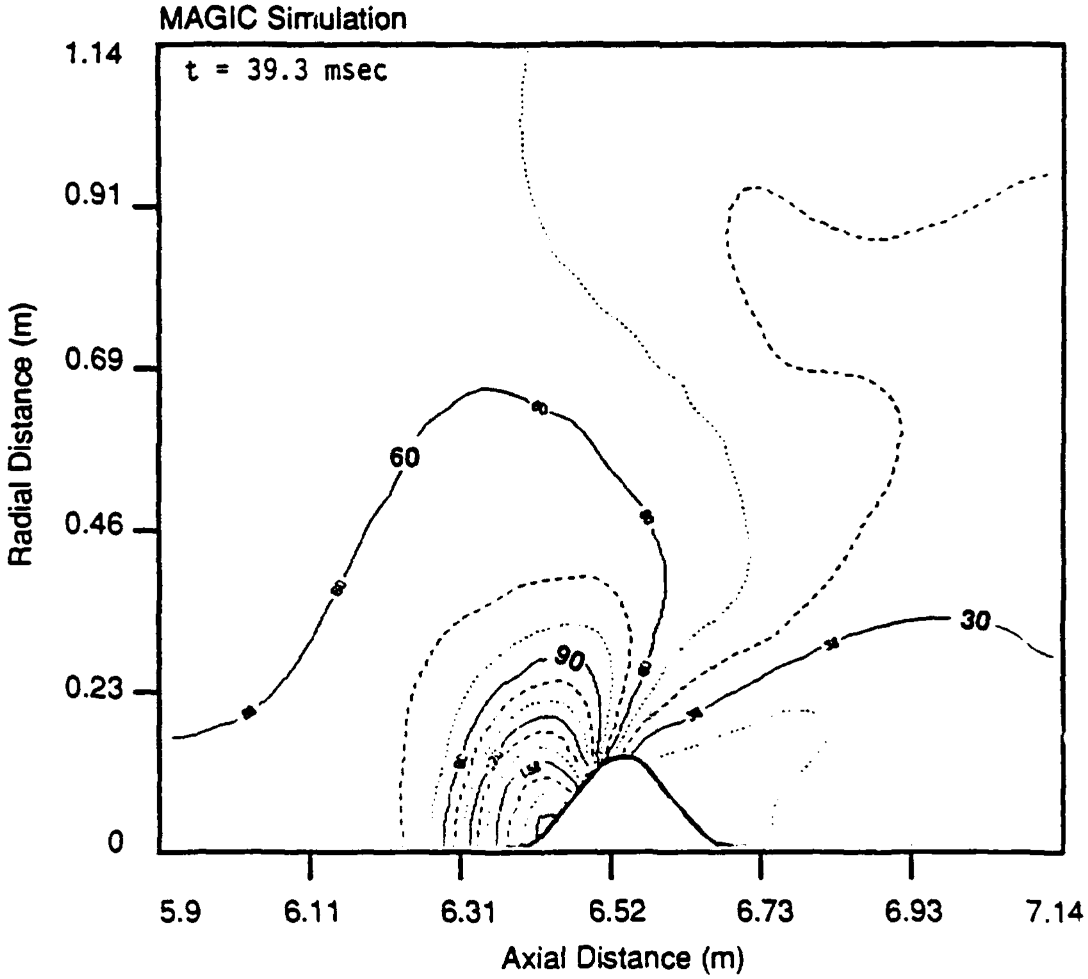

Figure 37. Static overpressure contours (psi) during maximum vehicle loading for HST6-60.

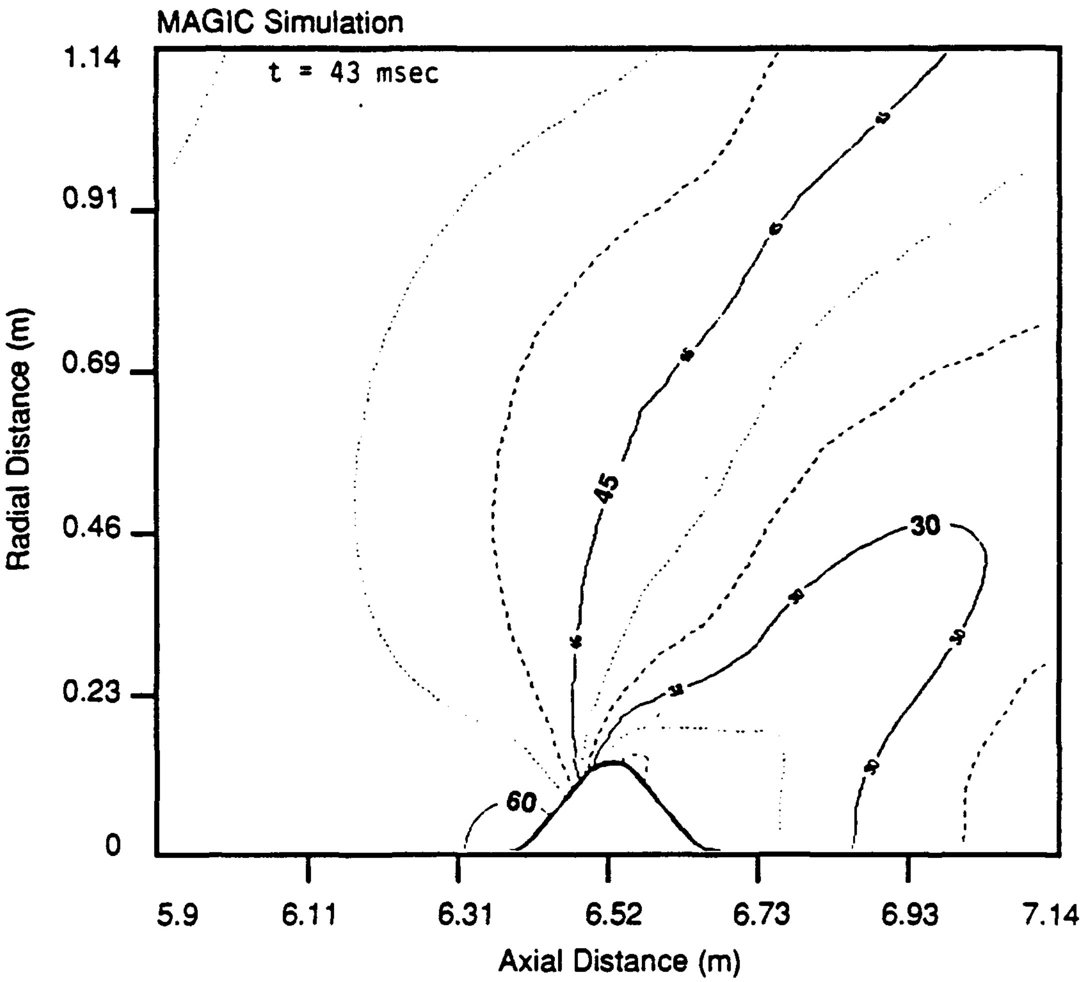

Figure 38. Static overpressure contours (psi) during quasi-steady flow phase for HST6-60.

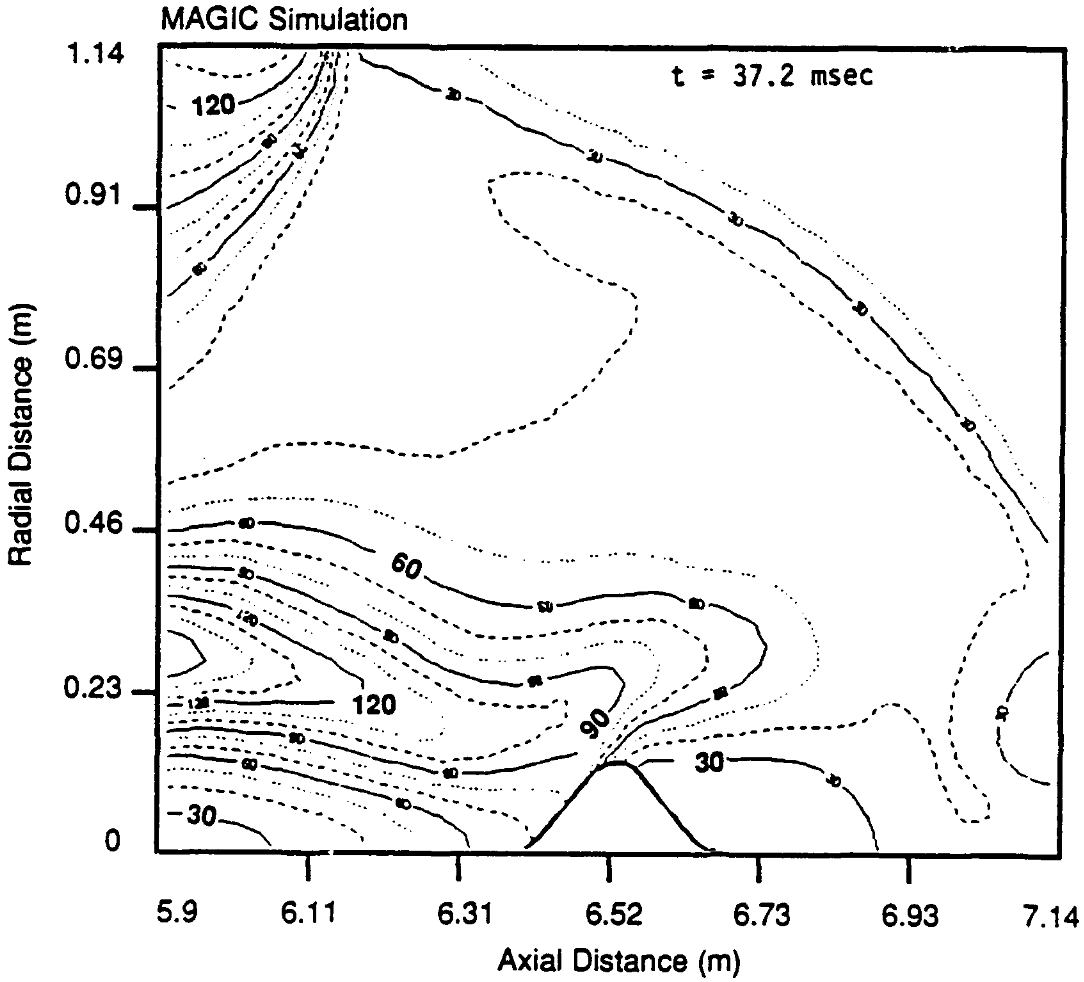

Figure 39. Stagnation pressure contours (psi) during precursor flow for HST6-60.

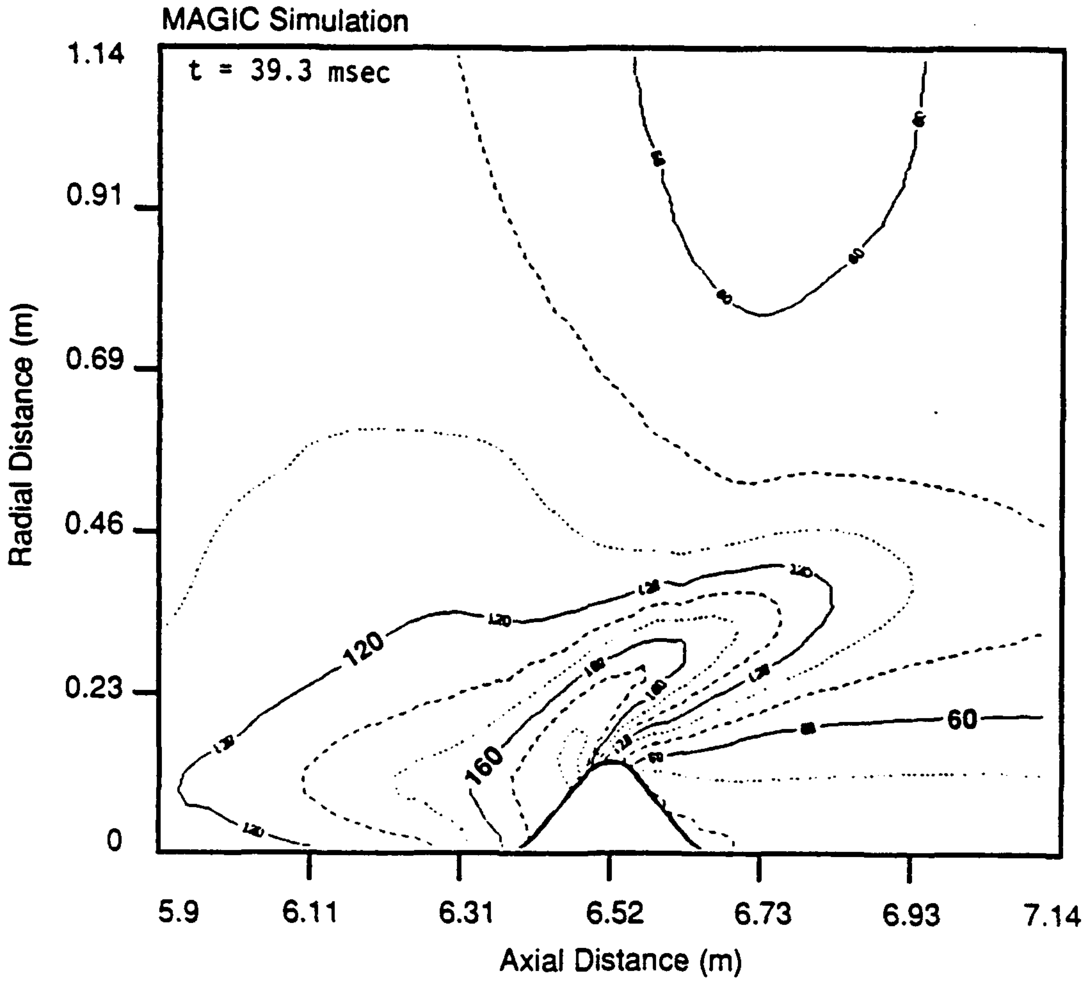

Figure 40. Stagnation pressure contours (psi) during maximum vehicle loading for HST6-60.

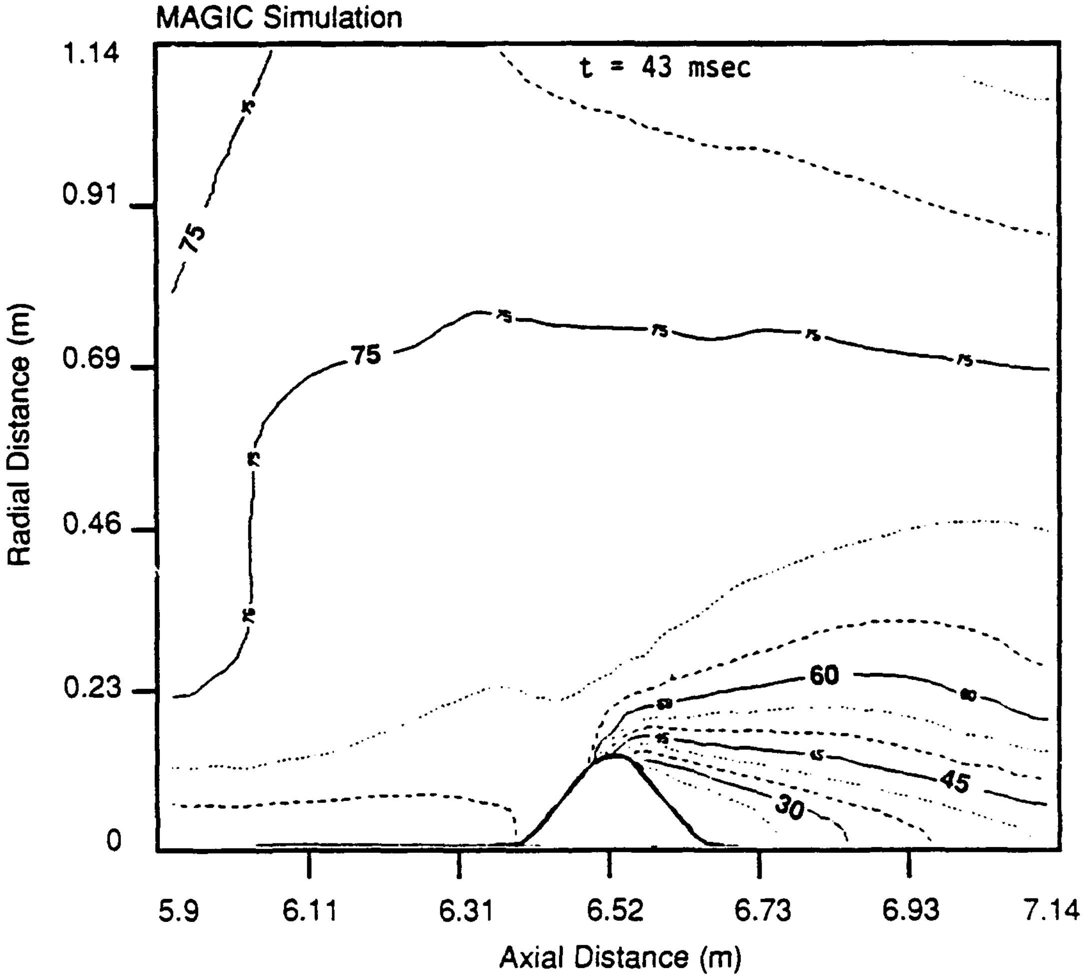

Figure 41. Stagnation pressure contours (psi) during quasi-steady flow phase for HST6-60.

In summary, the **MAGIC** predictions for HST6-60 are generally in favorable agreement with the experimental measurements. In particular, the maximum lift and drag loads are predicted quite accurately. Additional effort should be devoted to the assessment of the two-phase flow modeling, using both engineering and "full scale" experimental results; however, the initial comparisons with the HST6-60 simulation provide a degree of confidence in the **MAGIC** predictions for HML loads predictions in dusty, as well as clean, non-ideal environments.

4.3 FULL SCALE HML LOADS SIMULATION.

To date emphasis has been placed upon comparisons of **MAGIC** predictions with NMERI 6 foot shocktube data for the purpose of validating the model. In particular, attention has been focused upon the tests HST6-38, 39 and 60, which simulate non-ideal environments (resulting from a helium layer) with and without an HML model. This work has demonstrated the accuracy of the sequential multi-grid methodology and the **MAGIC** code at the engineering test scale.

In addition to focusing upon the validation of the methodology for dusty flows, the other primary objective of the current study was to address the issue of scales between the engineering tests and the full scale environment. In order to initiate this task a "large scale" **MAGIC** calculation was performed corresponding to the HST6-38 case scaled by a factor of 15 (in space and time). In the scaled space the HML model becomes a 6.25 ft radius semi-circle, and the solution domain extends to about 11 model heights vertically and 12 model heights horizontally. The driver conditions are those that were calculated for the non-ideal approach flow for HST6-38, except the time-dependent variables at the driver station were stretched in the vertical direction (by a factor of 15) and the time duration was extended by a factor of 15. This is consistent with the sequential multi-grid approach. Interestingly, this problem scales the HML to a NIAB flow for a yield near that of the Minor Scale Test.

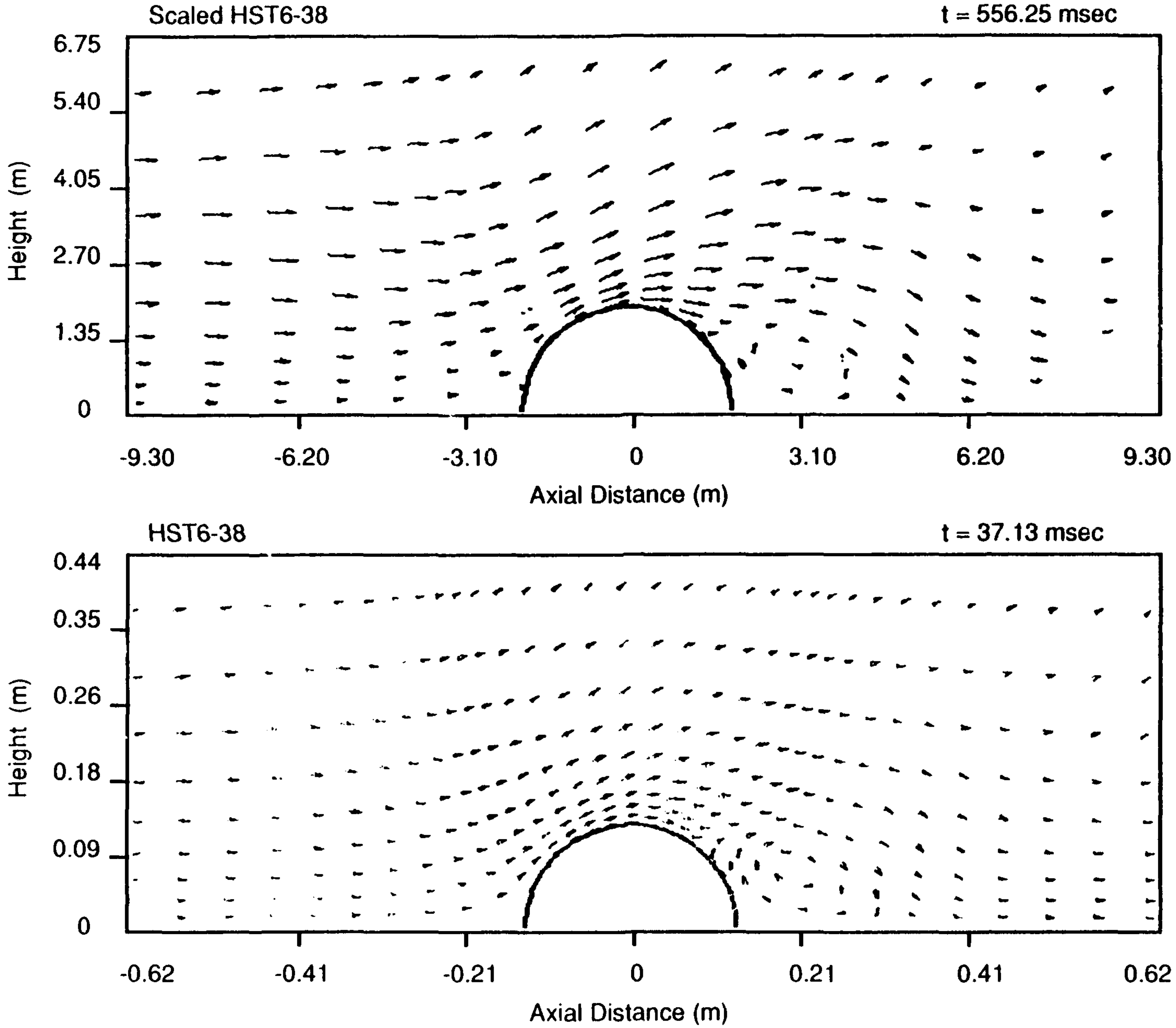

Figure 42. Velocity vector distributions at time of peak precursor strength.

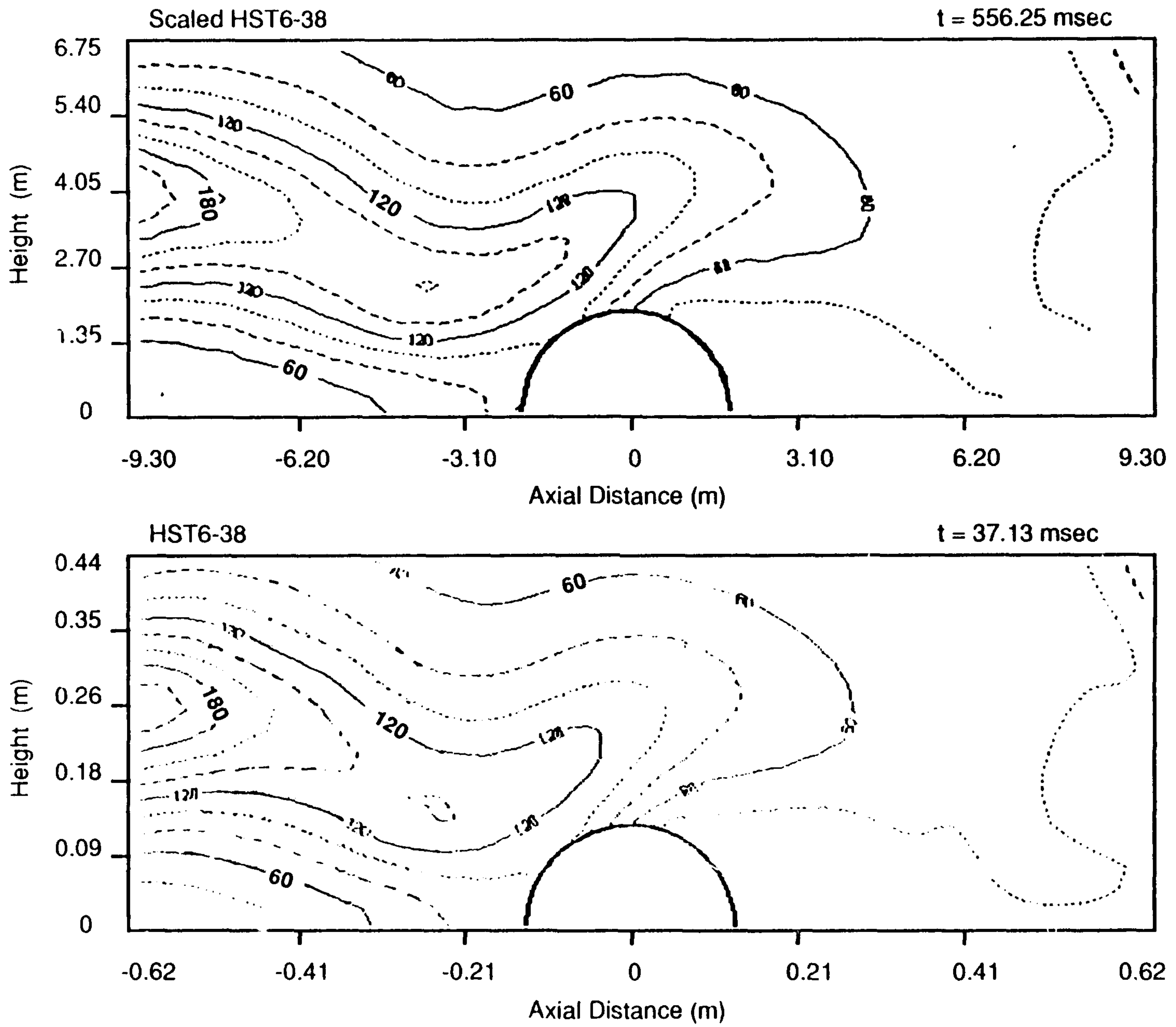

Figure 43. Stagnation pressure contours at time of peak precursor strength.

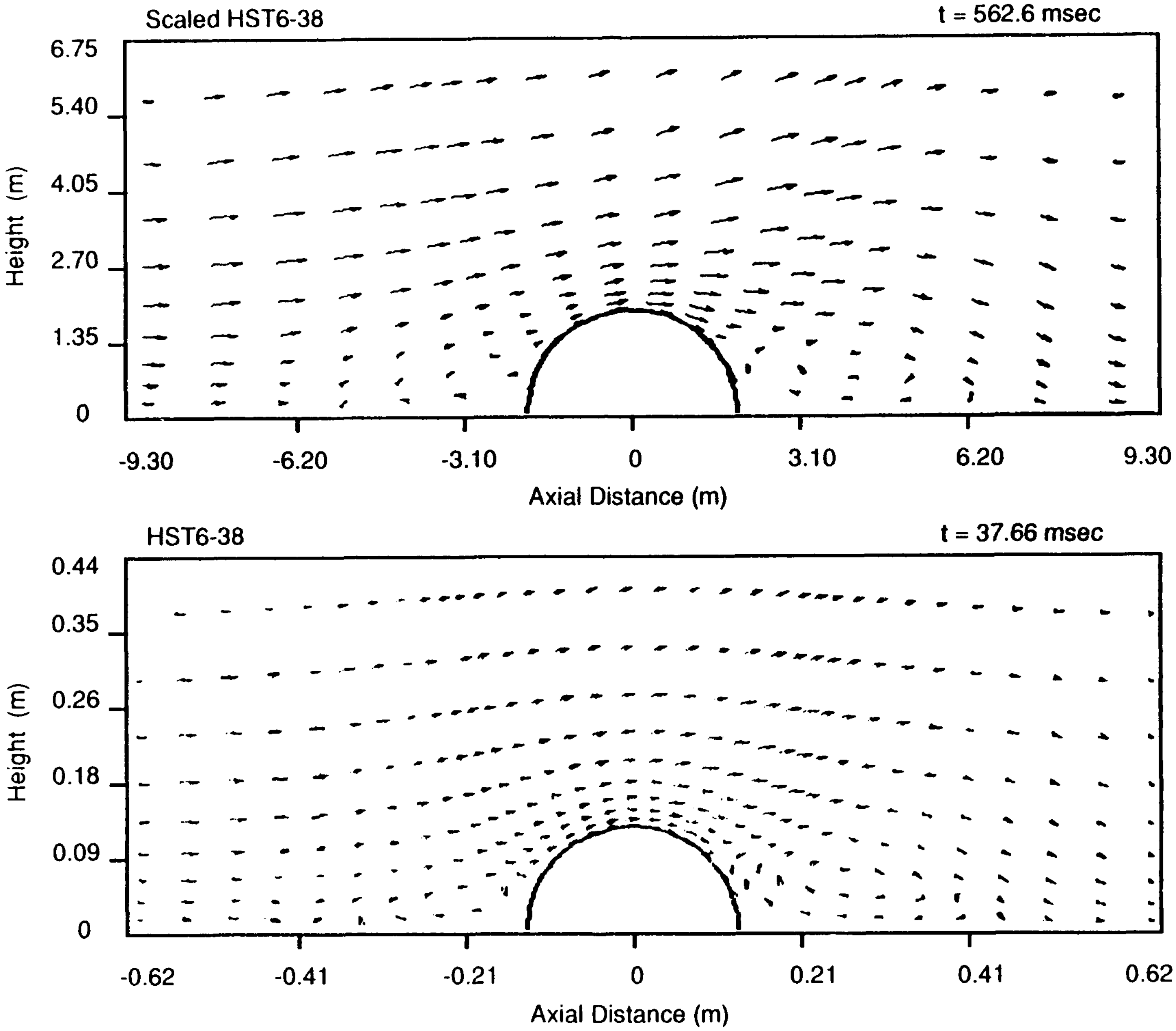

Figure 44. Velocity vector distributions at time of pressure well.

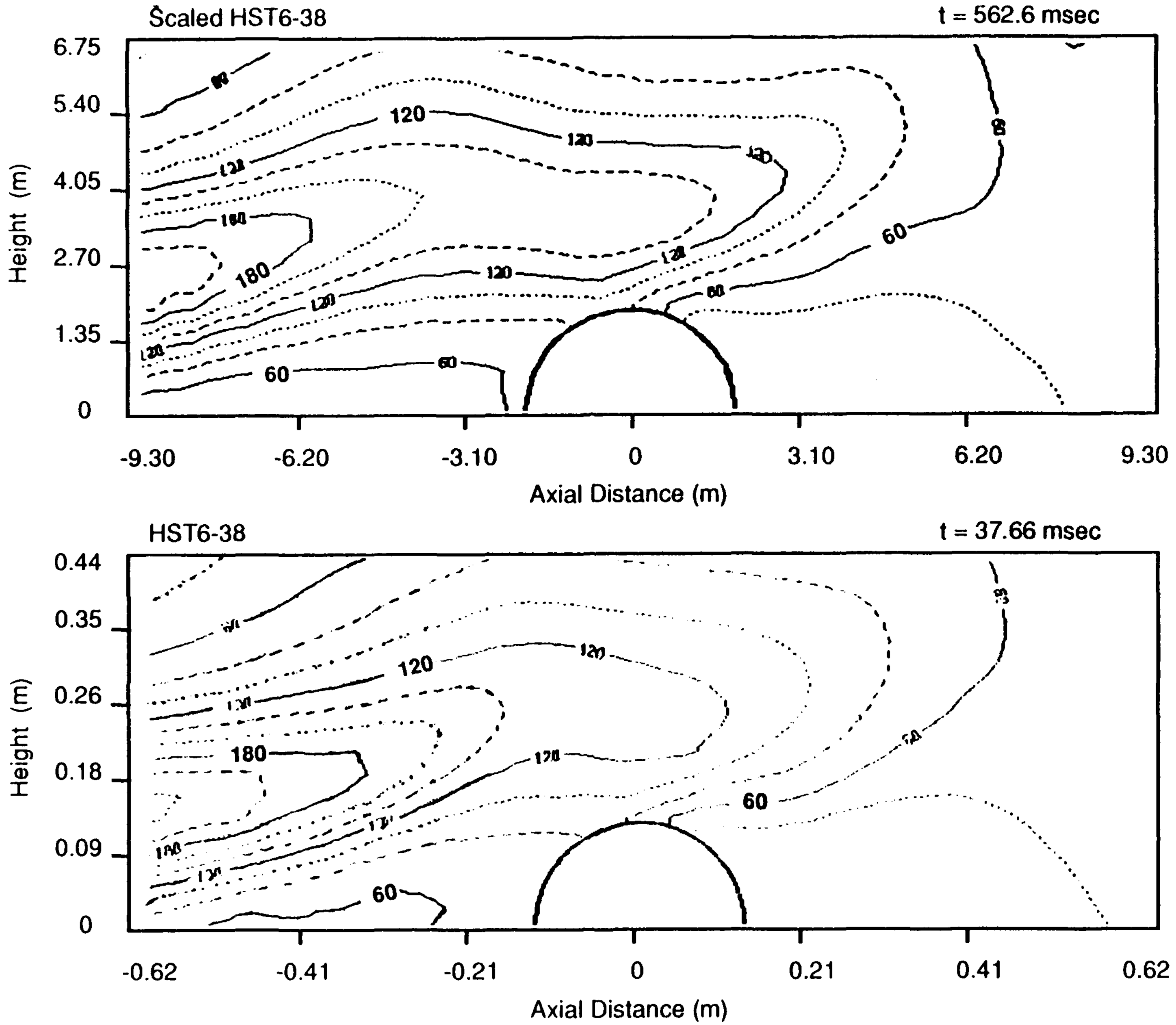

Figure 45. Stagnation pressure contours at time of pressure well.

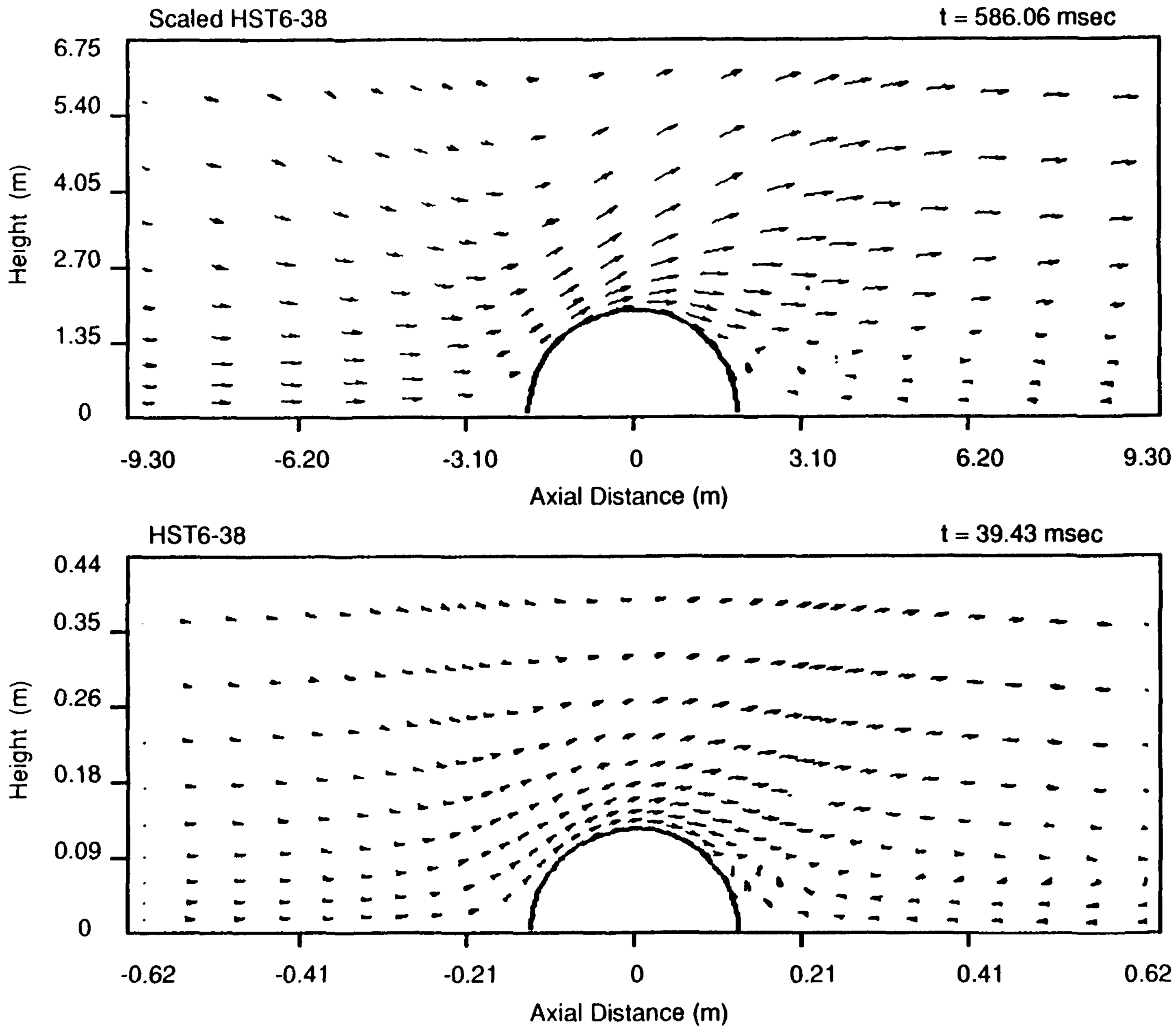

Figure 46. Velocity vector distributions at time of peak dynamic pressure.

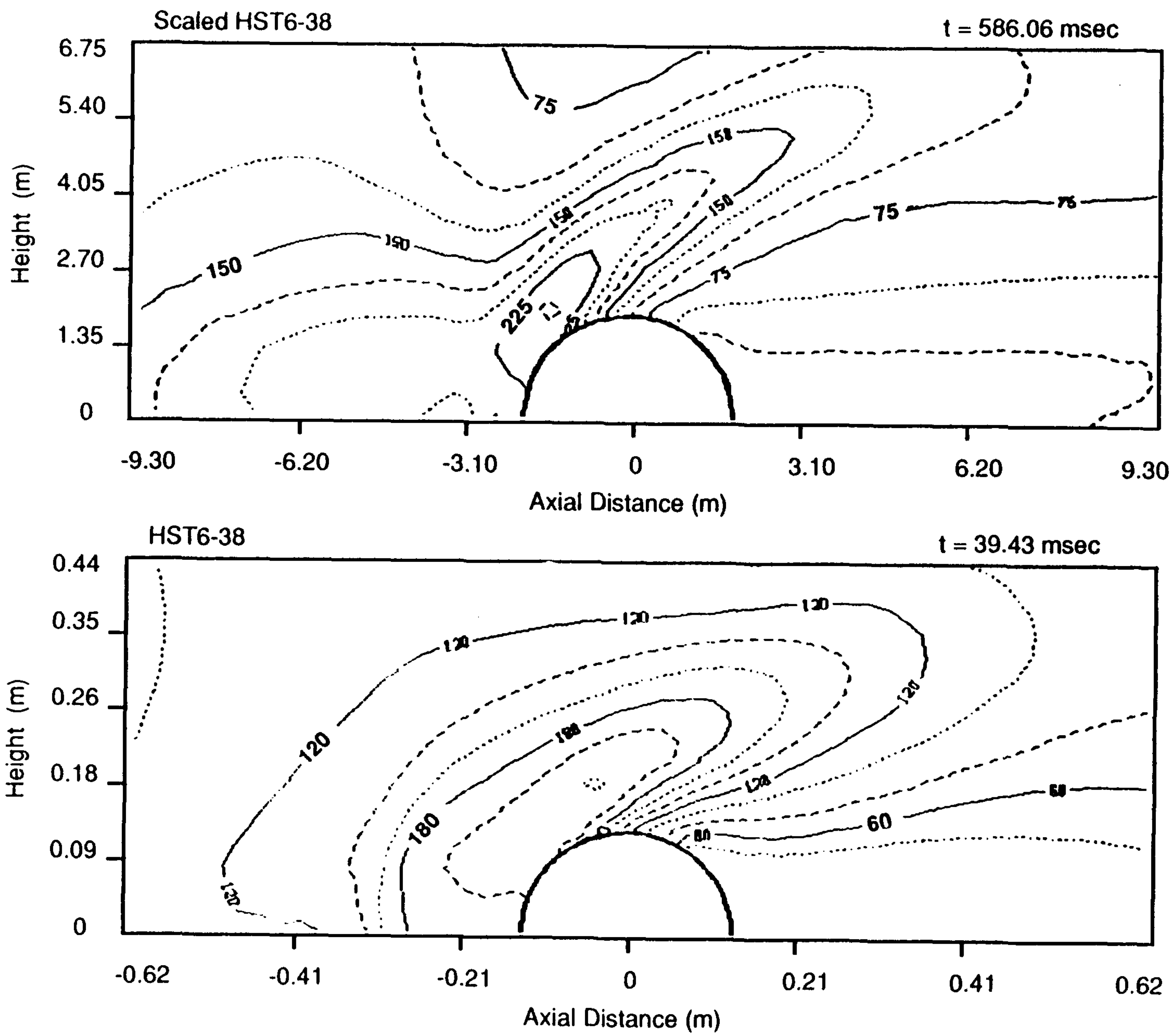

Figure 47. Stagnation pressure at time of peak dynamic pressure.

Figures 42 through 47 present comparisons of the velocity vector distributions and stagnation pressure contours between the original and scaled HST6-38 calculations at three selected times during the evolution of the pressure waveform. As depicted in the sketch below, the time snapshots are taken when the maximum precursor intensity is experienced (t_1), during the "pressure well" (t_2), and near the instant of peak dynamic pressure for the main shockwave (t_3).

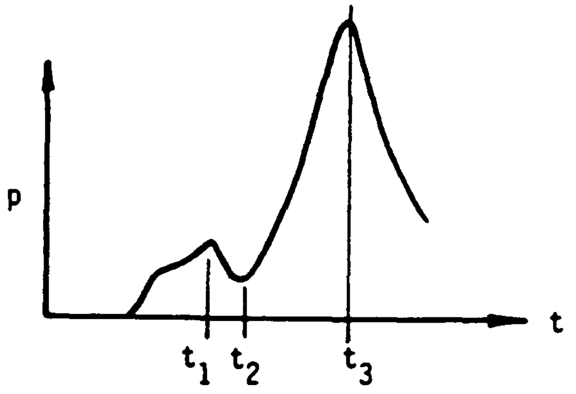

The comparisons illustrate a high degree of consistency between the solution performed for the 6 foot shocktube and the "full scale" calculation. Both **MAGIC** solutions indicate that the flow is initially attached on the forward face of the HML and then separates for a brief time between the precursor passage and the arrival of the main shockwave, at which time the flow is again sufficiently energetic to become reattached upstream. The occurrence of the transient upstream separation predicted by **MAGIC** coincides with the "pressure well" measured in the experiment.

Figures 43 and 45 illustrate a remarkable degree of consistency between the solutions for the stagnation pressure contours at the two earlier times. The modest differences between the contour distributions shown in Figure 47 are probably due to the fact that the scaled times do not agree exactly, combined with the observation that the temporal gradients are large at this point in time. However, these differences are not substantial, and Figure 47 serves to bolster confidence in the full scale calculation.

Figures 48 through 55 present calculated surface pressure histories at several locations on the forward face of the body. Two "full scale" HST6-38 computations were actually performed, each with a different treatment of the initial turbulent conditions. In one case, the initial turbulent parameters (the mean turbulent kinetic energy, the dissipation rate and the eddy viscosity) were scaled by appropriate powers of 15 for the purpose of driving the larger Region II solution. This may be called the rigorous approach. In the other case, the driver flow turbulent values, only on the initial data plane, were set to zero. Turbulent energy was then allowed to develop naturally within the Region II solution as a result of the existing local shear gradients. The second case may be thought of as a situation in which all upstream history effects on the turbulent state are lost. The purpose of this exercise was simply to investigate the significance of the turbulent variables' memory of upstream events on the Region II solution. In other words, it is a test of the necessity to rigorously include the time-dependent driver histories for the turbulent parameters for multi-region calculations.

Figures 48 through 55 indicate that the pressure histories are similar, but not identical, for each type of calculation. The major difference is that the pressure well lasts for a longer period of time in the calculation with the nulled initial turbulence values. The altered turbulent state at the driver plane produces a longer period of upstream separation, and the strength of the precursor and main shock wave are somewhat attenuated. This indicates the need for a rigorous treatment of the time-dependent turbulent variables across the interface planes of all sequential multi-grid calculations.

Figures 56 and 57 present the corresponding calculated surface pressure histories on the five inch model in the six foot shocktube test (HST6-38). Comparing these results with the large scale calculation (Figures 48 through 55) shows that: 1) the waveforms (particularly peak pressure) are quite similar at small polar angles (< 20-30°), and 2) for larger polar angles, the

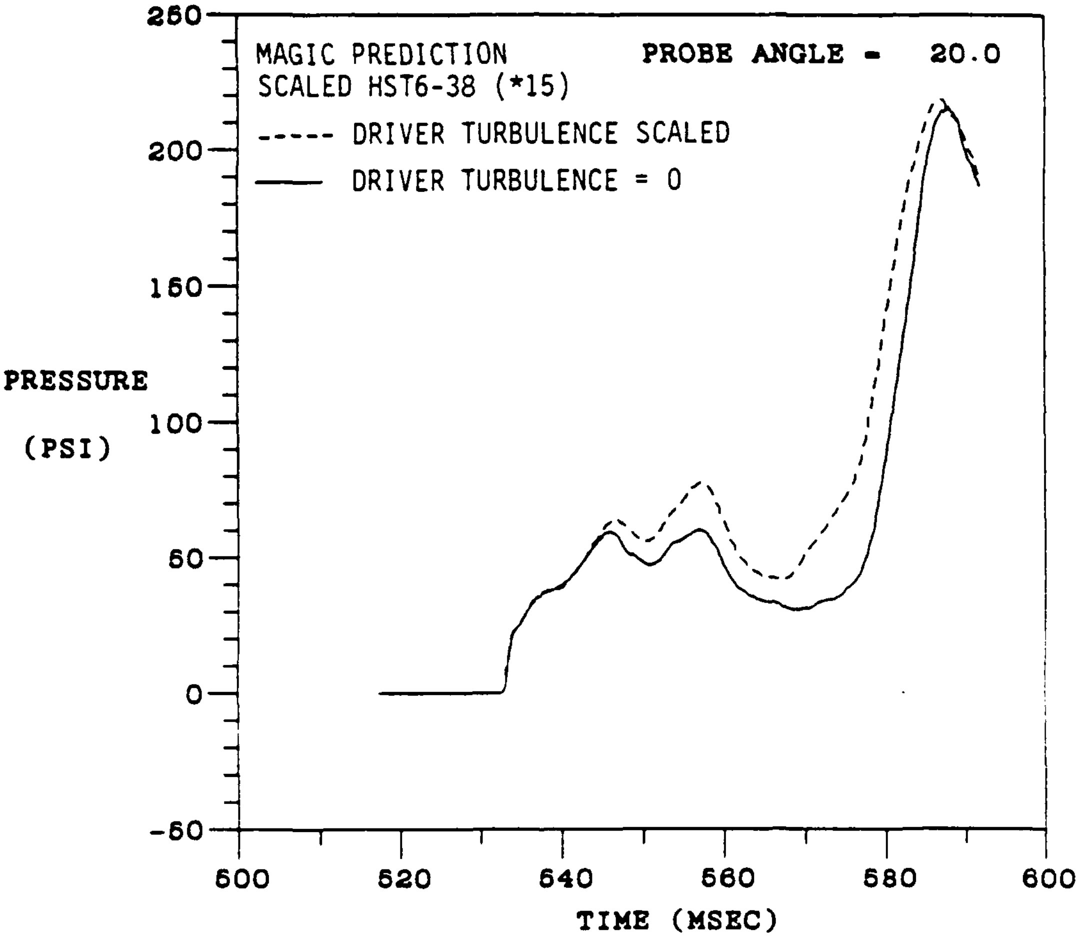

Figure 48. Surface pressure history on cylindrical HML in full scale NIAB flow, $\phi = 20^{0}$.

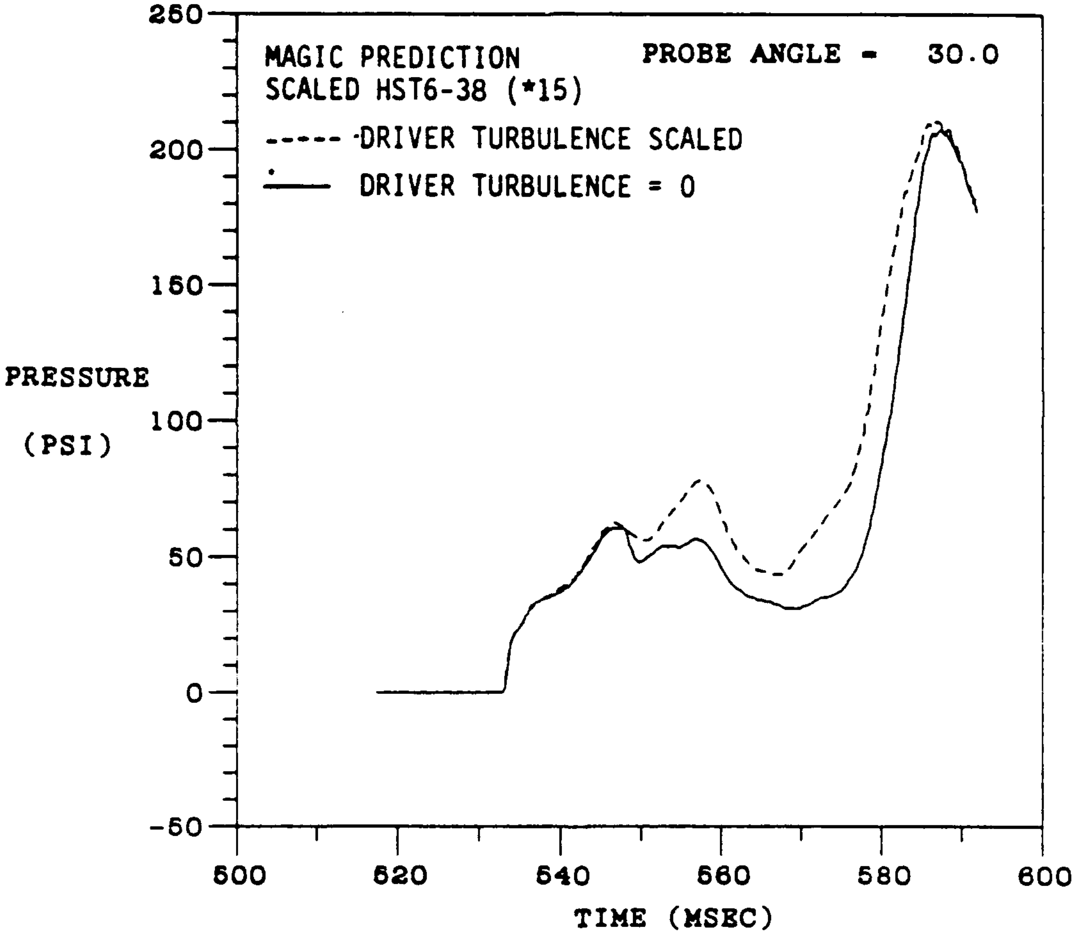

Figure 49. Surface pressure history on cylindrical HML in full scale NIAB flow, $\phi = 30^{0}$.

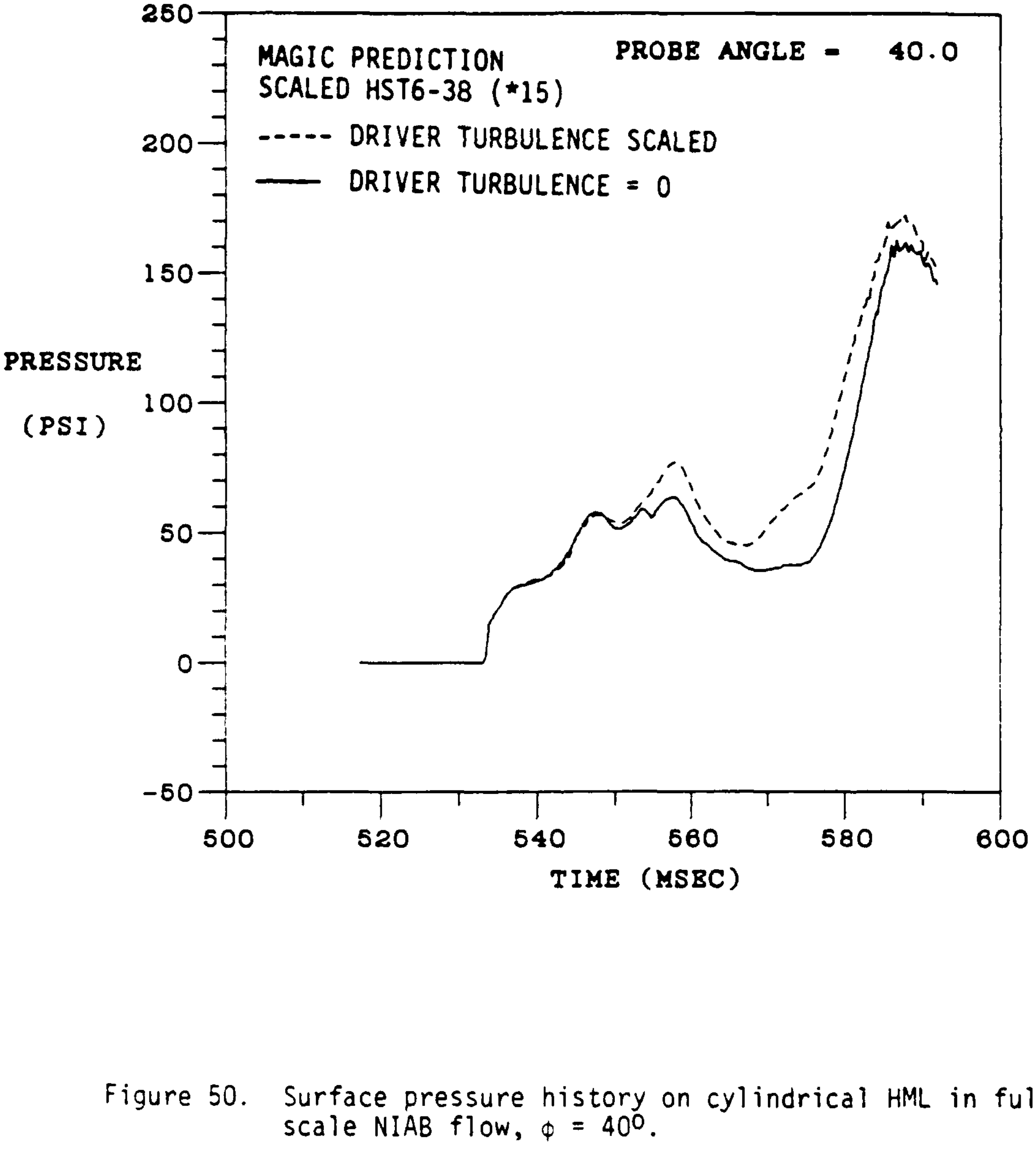

Figure 50. Surface pressure history on cylindrical HML in full scale NIAB flow, $\phi = 40^{\circ}$.

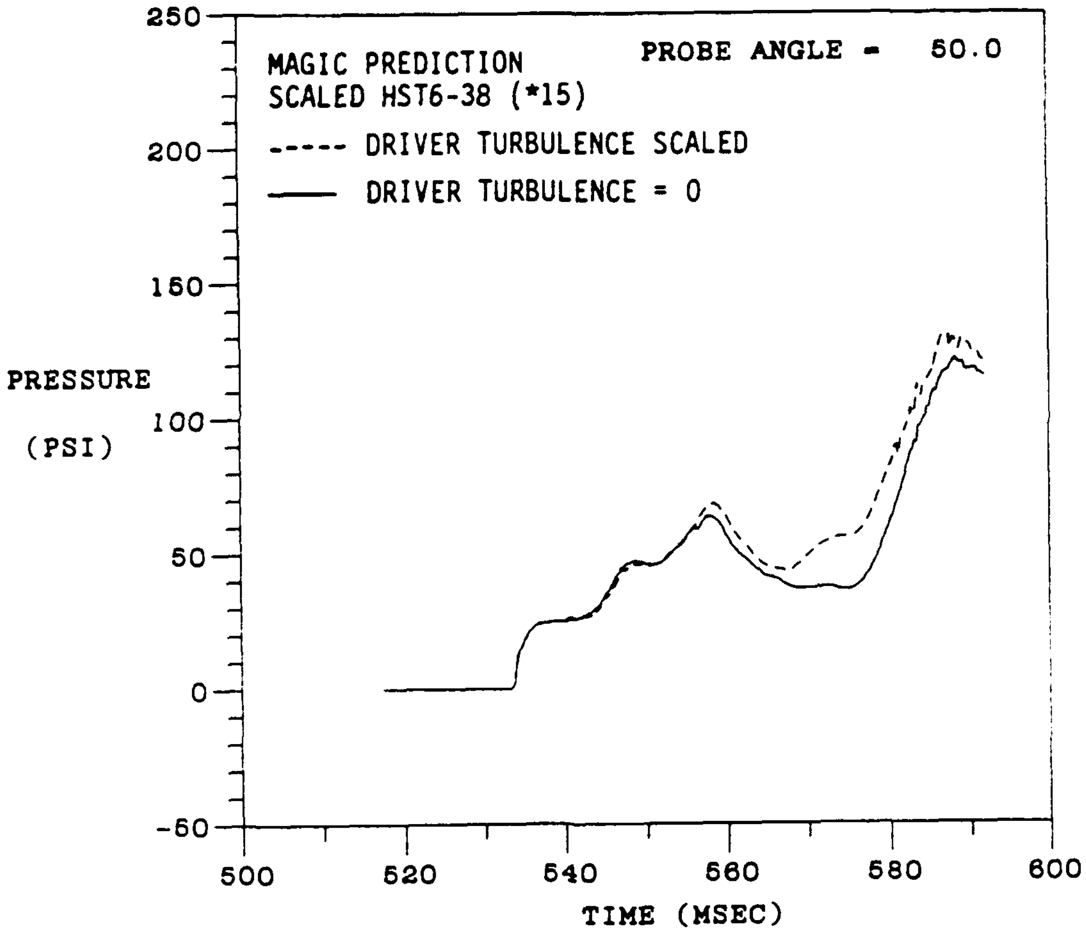

Figure 51. Surface pressure history on cylindrical HML in full scale NIAB flow, $\phi = 50^0$.

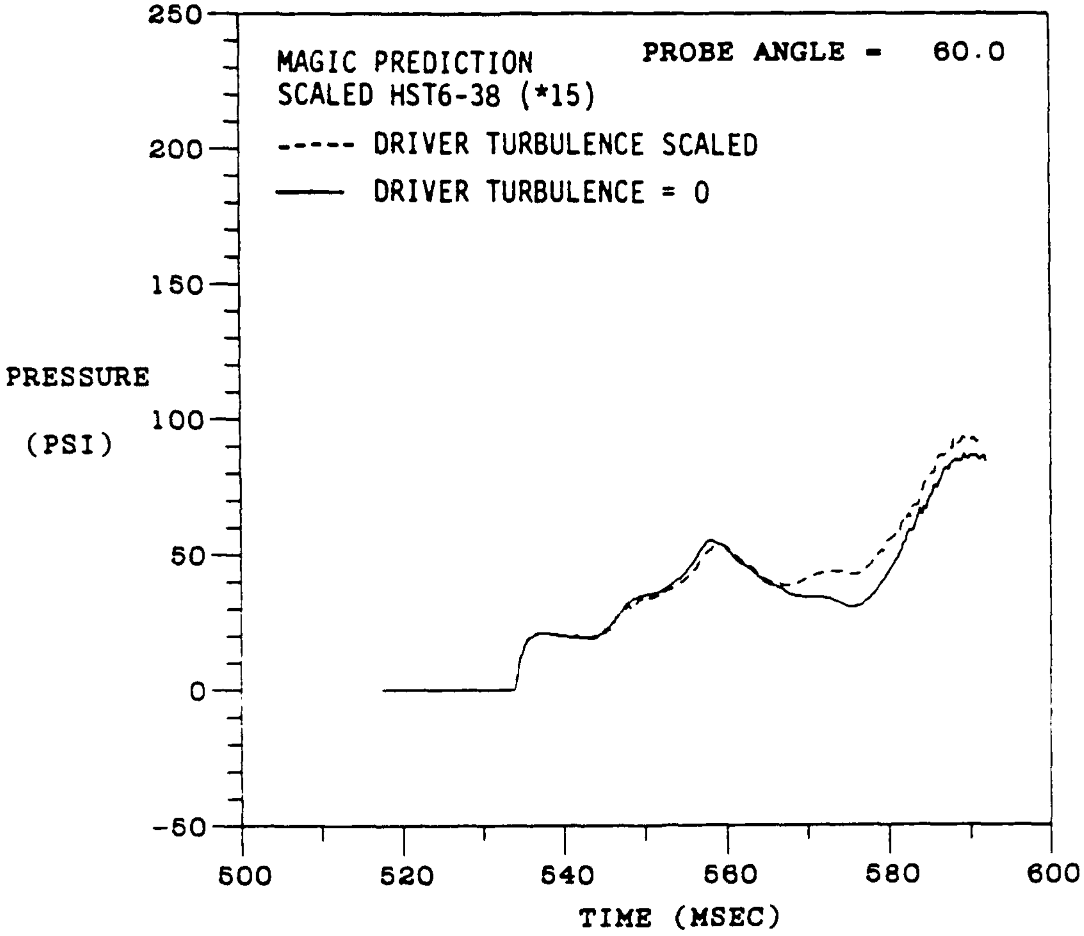

Figure 52. Surface pressure history on cylindrical HML in full scale NIAB flow, $\phi = 60^{\circ}$.

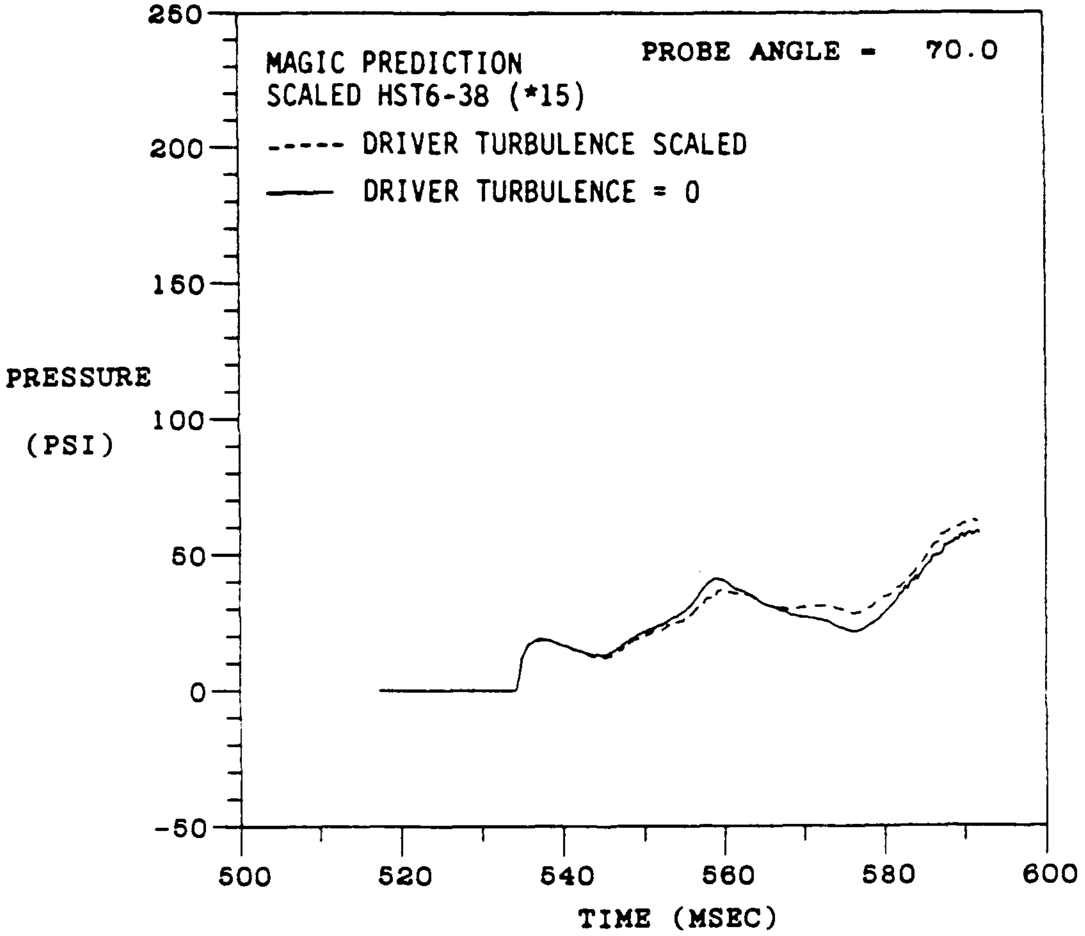

Figure 53. Surface pressure history on cylindrical HML in full scale NIAB flow, $\phi = 70^0$.

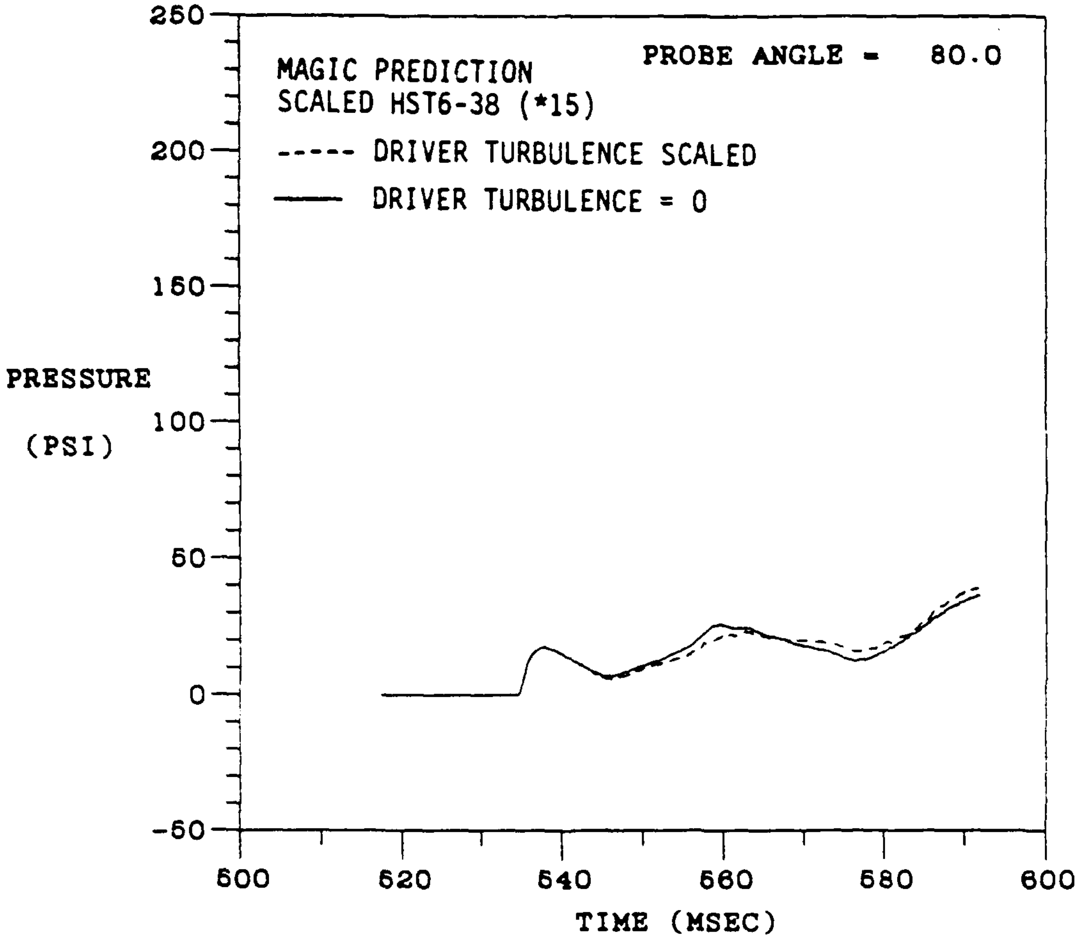

Figure 54. Surface pressure history on cylindrical HML in full scale NIAB flow, $\phi = 80^o$.

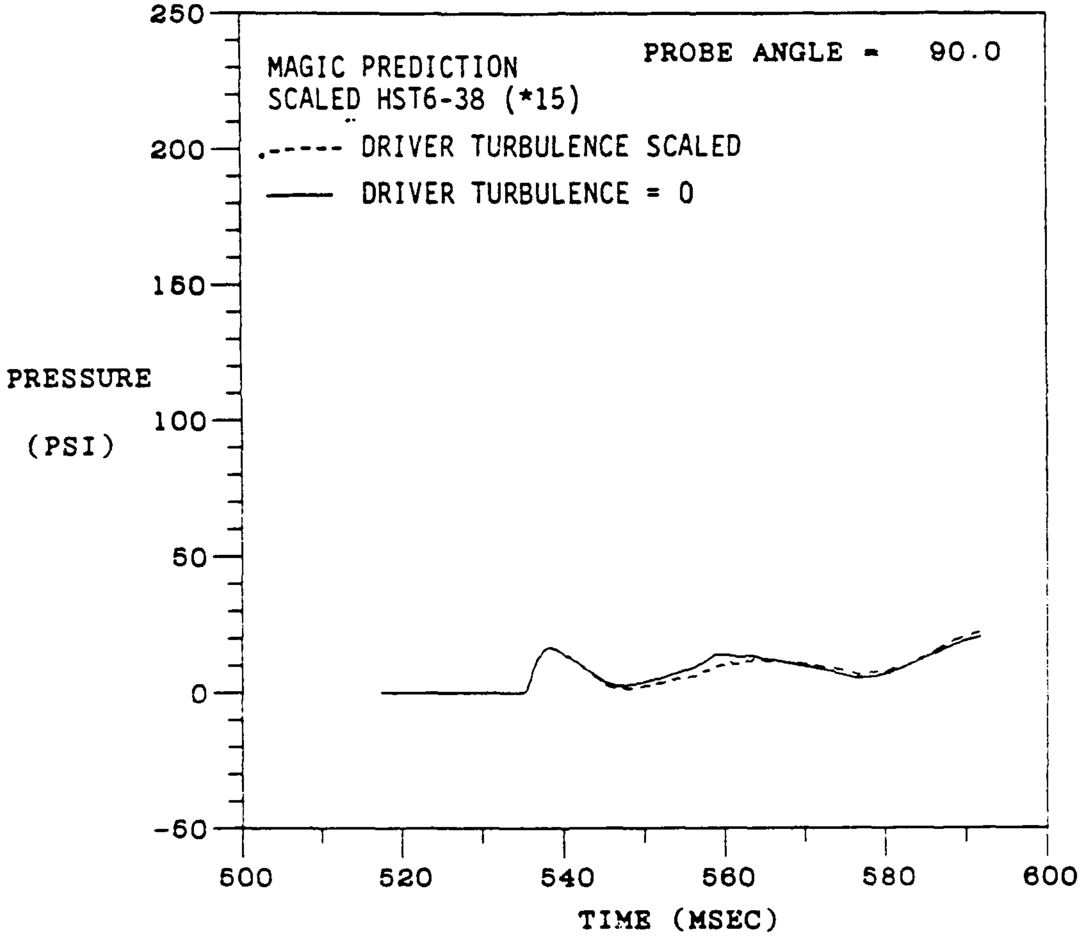

Figure 55. Surface pressure history on cylindrical HML in full scale NIAB flow, $\phi = 90^o$.

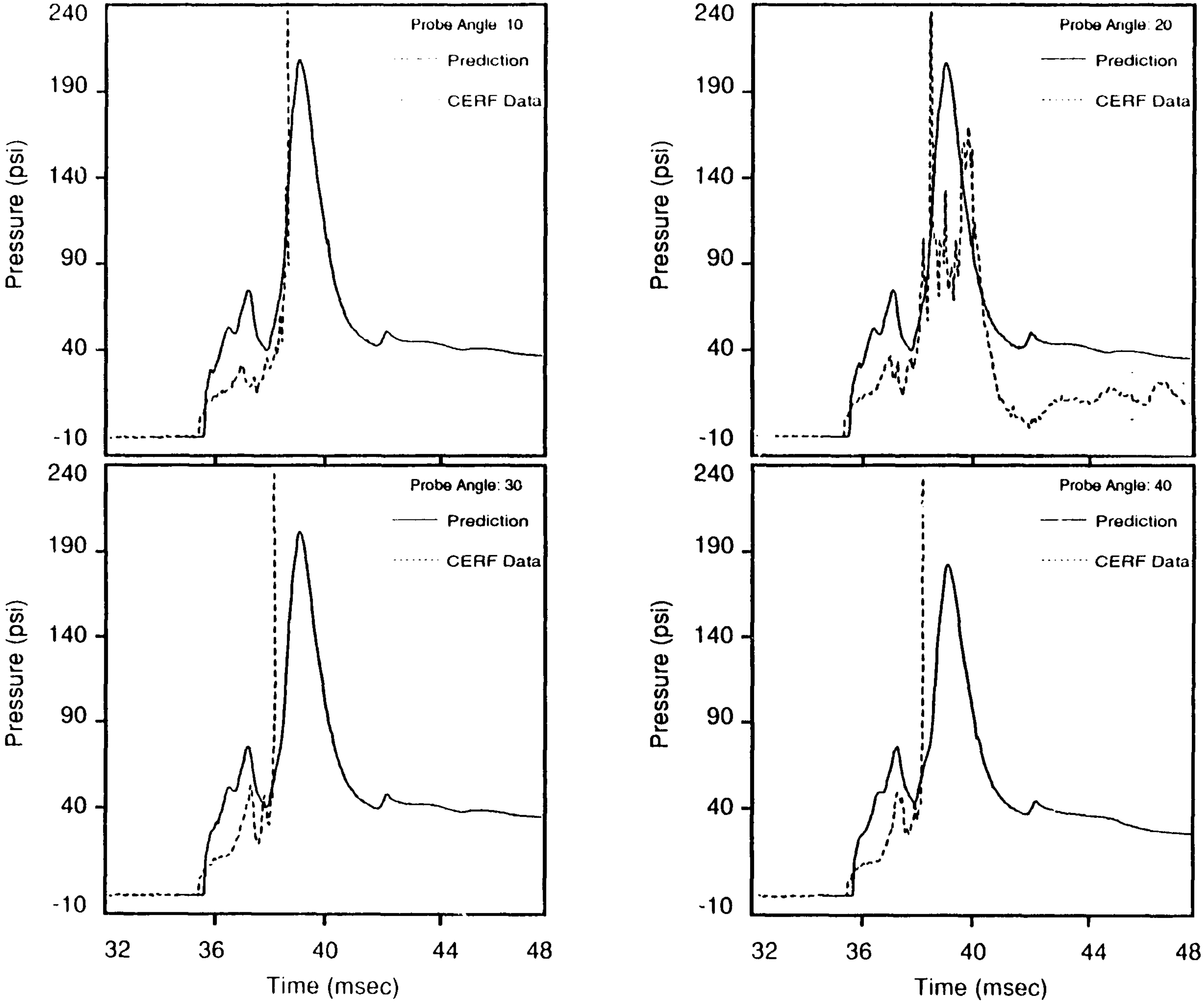

Figure 56. Pressure histories for HST6-38.

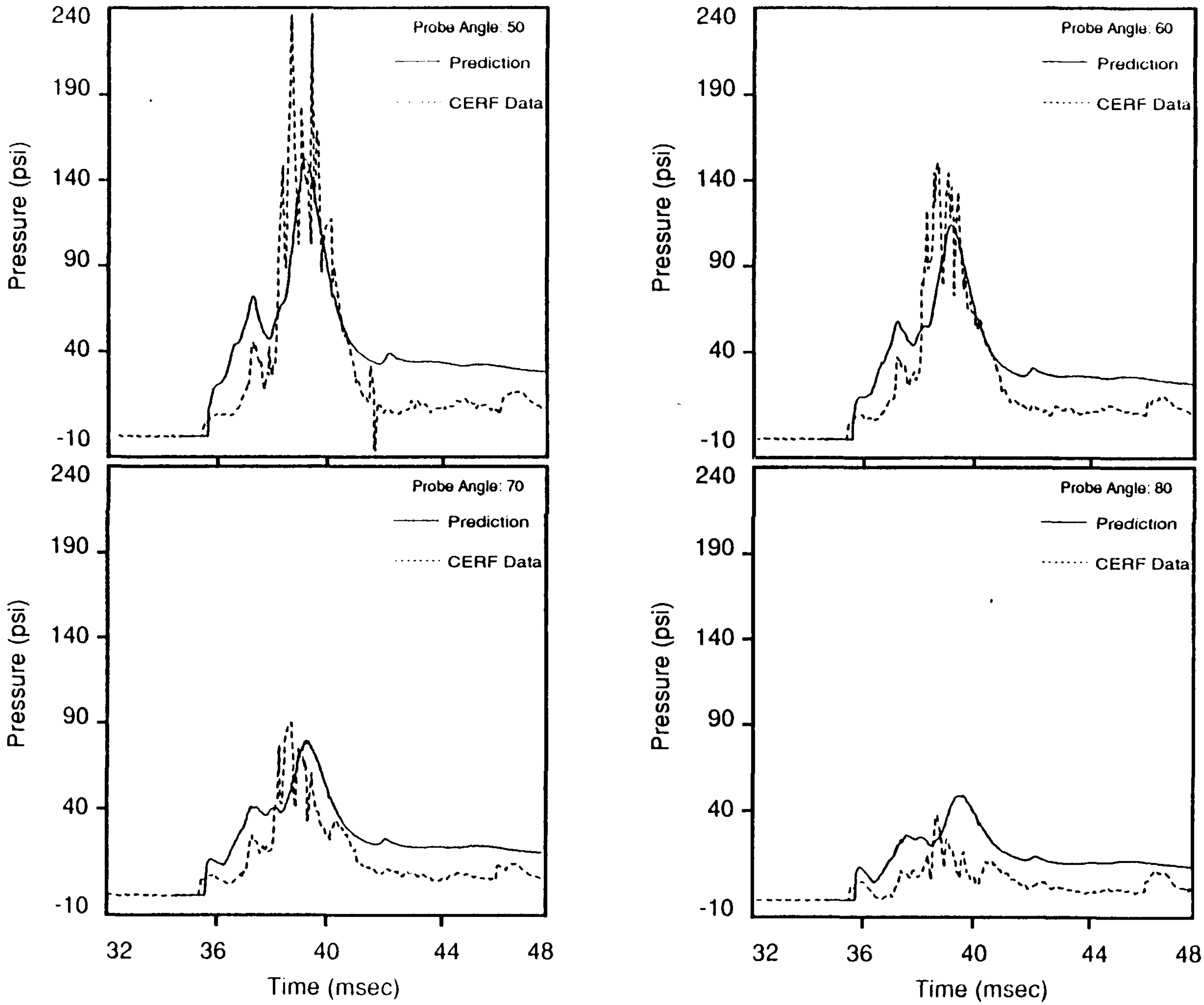

Figure 57. Pressure histories for HST6-38.

main shockwave pressures are about 20-30% smaller in the large scale solution than they are in the original HST6-38 computation. These differences in the circumferential pressure distributions can be attributed to an order of magnitude change in the Reynolds number, which can be expected to affect the mixing and dissipation rate of the wall jet flow. Consistent with the pressure results, the drag coefficient histories are very similar for both solutions, and the maximum lift coefficient is approximately 10% smaller for the large scale HML.

These comparisons again demonstrate a high degree of consistency between the engineering scale calculation (HST6-38) and its scaled counterpart. These initial indications are very encouraging. They show that the **MAGIC** code can model and accommodate the effects of scale between engineering tests and the full scale environment, even within the restrictions of available computer resources.

SECTION 5

LIST OF REFERENCES

1. Ausherman, D.R. (1973), "Initial Dust Lofting: Shock Tube Experiments", Defense Nuclear Agency Report No. DNA-3162F.

2. Bangold, R.ê. (1941), The Physics of Blown Sands and Desert Dunes, Methuen and Co., London.

3. Book, D.L., J.P. Boris, and K. Hain (1975), "Flux Corrected Transport II: Generalizations of the Method", Journal of Computational Physics, Vol. 18, pp. 248-283.

4. Boris, J.P., and D.L. Book (1973), "Flux Corrected Transport I: SHASTA, A Fluid Algorithm That Works", Journal of Computational Physics, Vol. 1 pp.38-69.

5. Boris, J.P., and D.L. Book (1976), "Flux Corrected Transport III: Minimal-Error FCT Algorithms", Journal of Computational Physics, Vol. 20, pp. 397-431.

6. Brown, G.L., and A. Roshko (1974), "On Density Effects and Large Structure in Turbulent Mixing Layers", J. Fluid Mech., Vol. 64, Part 4, p. 775.

7. Chepil, W.S. (1945), "Dynamics of Wind Erosion, Soil Sci., Vols. 60 and 61.

8. Dawes, J.O. (1952), "Dispersion of Dust Deposits by Blasts of Air", Safety in Mines Research Establishment, Research Report No. 36, Part 1: May, Part II: Nov.

9. Densison, M.R. and E. Baum (1984), "Engineering Research Support to the DNA ICBM Basing Program: Vol III Dusty Boundary Layer Modeling", Contract No. DNA-001-84-C-0107.

10. Dudziak, W.F. (1985), "Dust Boundary Layer Measurements", presented at HML Simulation Working Group Meeting, R&D Associates, Marina Del Ray, 6 May 21.

11. Hartenbaum, B. (1971), "Lofting of Particulate by a High Speed Wind", Applied Theory Inc., Report No. ATR-71-25, July.

12. Hirt, C.W., A.E. Amsden, and J.L. Cook (1974), "An Arbitrary-Lagrangian Eulerian Computing Method for all Flow Speeds", Journal of Computational Physics, Vol. 14, pp. 227-253.

13. Kirsch, J.W. (1977), "Near Surface Nuclear Dust Cloud Studies", Defense Nuclear Agency Report No-4332F, Jan.

14. Kulkarny, et al (1985), "Dust Lofting Experiments", presented at Defense Nuclear Agency Meetings; Dust Cloud Environmental Data Base Review, SRI International, Menlo Park, April 30.

15. Mirels, H. (1955), "Laminar Boundary Layer Behind a Shock Advancing Into Stationary Fluid", NACA TN3401, Mar.

16. Mirels, H., and J. Hammar (1962), "Laminar Boundary Layer Behind a Strong Shock Moving with Non Uniform Velocity", Physics of Fluids, Vol. 5, p . 91, Jan.

17. Mirels, H. (1984), "Turbulent Boundary Layer Behind Constant Velocity Shock Including Wall Blowing Effects", AIAA Journal, Vol. 22, No. 8, p. 1042.

18. Mirels, H. (1984), "Blowing Model for Turbulent Boundary Layer Dust Injection", AIAA Journal, Vol. 22, No. 11, p. 1582.

19. Owen, P.R. (1964), "Saltation of Uniform Grains in Air", J. Fluid Mech., Vol. 20, pp. 225-242.

20. Quan, V.C., and D.R. Crawford (1972), "Blast Wave Turbulent Boundary Layers", TRW Systems Report No. 18843-6001-R0-00, Defense Nuclear Agency Report No. DNA-2768F, Feb.

21. Quan, V.C. and R.M. Traci (1971), "An AnÃlysis of Blastwave Laminar Boundary Layers and PArticle Entrainment", Defense Atomic Support Agency Report DASA2627, April (Confidential).

22. Roberts, L. (1963), "The Action of Hypersonic Jet on a Dust Layer", IAS Paper No. 63-50.

23. Rosenblatt, M. et al (1984) "1 Mt, SHOB 200 ft/kt $^{1/3}$, 'Real' Surface Airblast Calculation", California Research and Technology, Report No. CRT584-06PM, May.

24. Singer, J.M. et al (1972), "Dispersal of Coal and Rock Dust Deposits", Bureau of Mines Report of Investigations, Ri-7642.

25. Singer, J.M. et al (1976), "Dust Dispersal Explosion Induced Airflow", Bureau of Mines Report of Investigations, RI-8130.

26. Singer, J.M. et al (1969), "Some Aspects of the Aerodynamics of Formation of Float Coal Dusts", Bureau of Mines Investigations, RI-7252.

27. Su, F.Y., R.M. Traci, G.T. Phillips and A.A. Boni (1983), "Dynamic Behavior of Fuel Droplet Spray in an Internal Combustion Engine Environment", Ninth International Colloquium on Dynamics of Explosions and Reactive Systems, Poitier, France, July.

28. Traci, R.M., and F.Y. Su (1986), "a User's Guide for the MAGIC Multi-Component Fluids Simulation Model", Science Applications International Corp., Report No. SAIC-86/65553.

29. Traci, R.M. et al. (1981), "MAGIC Code", sections in Comparison Between Measurement and Analysis of Fluid Motion in Internal Combustion Engines, edited by P.O. Witze, Sandia National Laboratories, Livermore, CA, Report No. SAND-81-8242.

30. Traci, R.M. et al. (1987), "Computational Analysis of Nonideal Airblast Phenomenology and Hardened Mobile Launcher Loads, DNA-TR-xxxx.

31. Vidal, R.J. (1962), Aerodynamic Processes in the Downwash-Impingement Problem", J. Aerospace Sci., Vol. 29, pp. 1067-1076.

32. Wilcox, D.C., and R.M. Traci (1976), "A Complete Model of Turbulence", AIAA 9th Fluid and Plasma Dynamic Conference, San Diego, CA, AIAA Paper No. 76-351.

33. Woodward, P., and P. Collela (1983), "The Numerical Simulation of Two-Dimensional Fluid Flow with Strong Shocks", UCRL-86952 Rev. I.

34. Zalesak, S.T. (1979), "Fully Multidimensional Flux-Corrected Transport Algorithms for Fluids", Journal of Computational Physics, Vol. 31, pp. 335-362.

DISTRIBUTION LIST

DNA-TR-87-171-V6

DEPARTMENT OF DEFENSE

AFSOUTH
ATTN: U S DOCUMENTS OFFICER

ASSISTANT TO THE SECRETARY OF DEFENSE
ATTN: EXECUTIVE ASSISTANT

DEFENSE INTELLIGENCE AGENCY
ATTN: DB-6E
ATTN: RTS
ATTN: RTS-2B

DEFENSE NUCLEAR AGENCY
ATTN: OPNS
ATTN: SPWE
4 CYS ATTN: TITL

DEFENSE NUCLEAR AGENCY
ATTN: TDNM
2 CYS ATTN: TDTT W SUMMA

DEFENSE TECHNICAL INFORMATION CENTER
2 CYS ATTN: DTIC/FDAB

FIELD COMMAND DEFENSE NUCLEAR AGENCY
ATTN: FCPR
ATTN: FCT COL J BOYCE

THE JOINT STAFF
ATTN: JKC (ATTN: DNA REP)
ATTN: JKCS

THE JOINT STAFF
ATTN: J-5 NUCLEAR & CHEMICAL DIV

UNDER SECRETARY OF DEFENSE
ATTN: J THOMPSON
ATTN: STRAT & THEATER NUC FORCES

DEPARTMENT OF THE ARMY

DEP CH OF STAFF FOR OPS & PLANS
ATTN: DAMO-NCZ

HARRY DIAMOND LABORATORIES
ATTN: SLCHD-NW-TS

U S ARMY MATERIAL TECHNOLOGY LABORATORY
ATTN: DRXMR-HH

U S ARMY MATERIEL COMMAND
ATTN: AMCCN

U S ARMY STRATEGIC DEFENSE CMD
ATTN: CSSD-H-SA

U S ARMY STRATEGIC DEFENSE COMMAND
ATTN: ATC-D WATTS
ATTN: CSSD-H-SA

DEPARTMENT OF THE NAVY

NAVAL RESEARCH LABORATORY
ATTN: CODE 2627 TECH LIB
ATTN: CODE 4040 D BOOK

OFFICE OF CHIEF OF NAVAL OPERATIONS
ATTN: OP 654

DEPARTMENT OF THE AIR FORCE

AIR UNIVERSITY LIBRARY
ATTN: AUL-LSE

BALLISTICS SYSTEMS DIVISION/MY
ATTN: CC
ATTN: CV
ATTN: ENSR
ATTN: MGET

STRATEGIC AIR COMMAND/XRFS
ATTN: XRFS

WEAPONS LABORATORY
ATTN: NTED J RENICK
ATTN: NTED R HENNY
ATTN: NTEDE CAPT K DEVAULT
ATTN: NTES
ATTN: WL/SUL

WRIGHT RESEARCH & DEVELOPMENT CENTER
ATTN: AFWAL/MLP
ATTN: WRDC/MTPM CAPT CAMERON

DEPARTMENT OF ENERGY

LAWRENCE LIVERMORE NATIONAL LAB
ATTN: L-10 J CAROTHERS
ATTN: L-122 G GOUDREAU
ATTN: L-285 DR S J SACKETT
ATTN: L-84 H KRUGER
ATTN: L-85 P CHRZANOWSKI

SANDIA NATIONAL LABORATORIES
ATTN: A CHABAI DIV 9311
ATTN: D J RIGALI 9140
ATTN: R G CLEM 1600

OTHER GOVERNMENT

CENTRAL INTELLIGENCE AGENCY
ATTN: OSWR/NED

DEPARTMENT OF THE INTERIOR
ATTN: D RODDY

DEPARTMENT OF DEFENSE CONTRACTORS

ACUREX CORP
ATTN: C WOLF

AEROSPACE CORP
ATTN: H MIRELS

APPLIED RESEARCH ASSOCIATES, INC
ATTN: C J HIGGINS

APPLIED RESEARCH ASSOCIATES, INC
ATTN: S BLOUIN

BDM INTERNATIONAL, INC
ATTN: J MERRITT

CALIFORNIA RESEARCH & TECHNOLOGY, INC
ATTN: M ROSENBLATT

CALIFORNIA RESEARCH & TECHNOLOGY, INC
ATTN: J THOMSEN

INFORMATION SCIENCE, INC
ATTN: W DUDZIAK

KAMAN SCIENCES CORP
ATTN: L MENTE
ATTN: R RUETENIK

KAMAN SCIENCES CORP
ATTN: D MOFFETT
ATTN: DASIAC

KAMAN SCIENCES CORPORATION
ATTN: DASIAC

MAXWELL LABORATORIES, INC
ATTN: J MURPHY

PACIFIC-SIERRA RESEARCH CORP
ATTN: H BRODE

R & D ASSOCIATES
ATTN: C K B LEE
ATTN: P RAUSCH
ATTN: T A MAZZOLA

R & D ASSOCIATES
ATTN: P MOSTELLER

R & D ASSOCIATES
ATTN: G GANONG
ATTN: J WALTON

S-CUBED
ATTN: C WILSON

SCIENCE APPLICATIONS INTL CORP
ATTN: H WILSON

SCIENCE APPLICATIONS INTL CORP
ATTN: DIV 411 R WESTERFELDT

SCIENCE APPLICATIONS INTL CORP
2 CYS ATTN: C C HSIAO
2 CYS ATTN: F Y SU
ATTN: J COCKAYNE
2 CYS ATTN: R M TRACI
2 CYS ATTN: T B HARRIS
2 CYS ATTN: T PHILLIPS
ATTN: W LAYSON

SCIENCE APPLICATIONS INTL CORP
ATTN: G BINNINGER

TRW SPACE & DEFENSE SECTOR SPACE
ATTN: D M LAYTON
ATTN: W WAMPLER

VITRO CORP
ATTN: ADA-12-RPT H BRIGHT

WEIDLINGER ASSOCIATES, INC
ATTN: P WEIDLINGER

DIRECTORY OF OTHER

MARYLAND UNIVERSITY OF
ATTN: H GLAZ